Shape modeling, attitude estimation, and classification of artificial Resident Space Objects (RSO) using photometric light curves

by

KATIYAYNI BALACHANDRAN

Presented to the Faculty of the Graduate School of
The University of Texas at Arlington in Partial Fulfillment
of the Requirements
for the Degree of

DOCTOR OF PHILOSOPHY

THE UNIVERSITY OF TEXAS AT ARLINGTON

August 2021

Shape modeling, attitude estimation, and classification of artificial Resident Space Objects (RSO) using photometric light curves

The members of the Committee approve the doctoral dissertation of Katiyayni Balachandran

Kamesh Subbarao
Supervising Professor

Donald R. Wilson _____

Animesh Chakravarthy _____

Ratan Kumar _____

Yue Deng _____

Dean of the Graduate School _____

Copyright © by Katiyayni Balachandran 2021

All Rights Reserved

To A and B, for always saying the sky's the limit.

Acknowledgements

First and foremost, I wish to thank the Almighty, for showering their abundant grace and benevolent blessings on me throughout this work to accomplish this.

It is with utmost pleasure that I express my deepest gratitude to Dr. Kamesh Subbarao: professor, mentor, and dissertation advisor. His dedication and involvement played a pivotal role in my completion of this work. I would like to thank him profusely for his scholarly advice, meticulous scrutiny, his guidance, and encouragement towards all external academic pursuits. I would certainly be remiss to not mention and sincerely thank the other members of my dissertation committee: Dr. Donald R. Wilson, Dr. Animesh Chakravarthy, Dr. Ratan Kumar, and Dr. Yue Deng. Their insight, feedback, and advice was influential and essential through the writing process.

To Dr.Tim Flohrer, Mr.Stijn Lemmens and all my colleagues in the Space Debris Office, I immensely cherished my time at the European Space Operations Centre (ESOC) and our intriguing discussions.

I would also like to thank my fellow labmates at the Aerospace Systems Laboratory (ASL), who have become great friends along the way. Their assistance and camaraderie welcomed me to the group. I appreciate the patience of all my teachers, professors, and educators from early on, who have helped shape me into the person I am today.

I gratefully acknowledge the funding received from the Natural Sciences and Engineering Research Council of Canada (NSERC), [CGSD3-532704-2019], Zonta International Amelia Earhart Fellowship, and University of Texas at Arlington's

Mechanical and Aerospace Engineering Department. I sincerely thank the authors and copyright holders of all the datasets and software used to accomplish this research. [1–3]

Lastly, to my two pillars of strength, my beautiful mother and amazing father, who have weathered through this arduous journey with me. I can't thank you enough for your unwavering support, encouragement, and unconditional love.

June 9, 2021

Abstract

Shape modeling, attitude estimation, and classification of artificial Resident Space Objects (RSO) using photometric light curves

Katiyayni Balachandran, Ph.D.

The University of Texas at Arlington, 2021

Supervising Professor: Kamesh Subbarao

Project Summary

Light curve inversion (LCI) has proven valuable in using photometric measurements to optimize various physical parameters of a resident space object (RSO) such as rotational period about its own spin axis, pole orientation and others. Other characteristics such as shape and size are dependent on the surface brightness. To accurately determine size, shape, spin rate, or attitude information of an unresolved resident space object, photometry is required to capture the relatively rapid changes in brightness that these objects can exhibit. LCI has been developed significantly for asteroids, although not fool-proof for artificial RSOs. Satellites and space debris, unlike asteroids, are dynamic in lighting and viewing geometry because they are closer to Earth. Additionally, while asteroids are roughly round, smooth, and have stable rotations, the opposite is true of man-made space objects, which often have sharp edges and flat surfaces that produce distinct specular glints. The minimal studies performed for satellites utilize *a priori* information on attitude and a simplified geometric model such as a cuboid. The objective is to determine the sidereal rotation period and shape of the RSO and subsequently, classify the object using these parameters.

Optical measurements for space object tracking are sensitive to shape, attitude, angular velocity, and surface parameters. Current state-of-the-art in RSO characterization relies heavily on nonlinear estimation theory which is computationally expensive. A data-driven approach for improved accuracy with a large volume of objects employs the use of deep neural networks. Given an unresolved object's light curve, in low earth orbit (LEO), we can characterize it by shape and spin rate using a Hidden Markov model (HMM) and Long Short-term Memory Recurrent neural network (LSTM RNN).

The tumbling rates are computed using the Lomb-scargle periodogram, which performs more accurately as opposed to other signal processing methods, and the synthetic light curves are generated using the Lebedev quadrature. This integrated model has been developed to identify tumbling and stabilized objects by testing for aliasing, periodicity, and feature extraction.

The application of photometric light curves has been extended to model Triton's atmosphere. To quantify the distortion required to reproduce the measured light curve (stellar occultation), a global model of the atmosphere of varying ellipticity can be constructed and fit using least-squares method. We can use the operations concept of a space probe releasing hundreds of small satellites into orbit around Triton in delayed succession to improve data collection capability and provide redundancy due to power constraints. The simulated data (with additional astrometric data of Triton) can be 3D mapped to generate the atmospheric model and validate predictions of Triton's expanding atmosphere due to thermal properties of the surface and increase in pressure.

Table of Contents

List of Illustrations

List of Tables

Chapter 1

Introduction

In recent years, there has been an increase in the number of active and defunct objects in space, leading to a large amount of space debris. Space situational awareness (SSA) requires active awareness of all objects in the Earth's orbit. The characterization of these Resident Space Objects (RSOs) is very important to national security, as drifting objects could cause collisions, or adversaries could maneuver objects so as to capture potentially confidential or classified data [6]. Due to the limited number of sensors available to track them, it is difficult to maintain persistent surveillance, and, therefore, there is inherent uncertainty and latency in the knowledge of the RSO population [7]. The space object catalog maintained by Joint Space Operations Center (JSpoC) currently includes more than 22,000 RSOs, with 1,100 of these objects being actively controlled and operated [8]. These aforementioned objects are of size 10 cm or larger, however objects less than and down to 2 cm have not been categorized and possibly may be in the range of a quarter-million. Researchers are interested in a detailed understanding, although the current space object catalog comprises of simplified characteristics such as solar radiation pressure and drag coefficients. For a comprehensive and reliable understanding, we need information on other characteristics that can provide insight into their dynamics such as shape and attitude play a vital role. Attitude (state of control) can in turn be used to accurately predict trajectory and behavior.

The use of optical sensors to track RSOs in near Earth orbits are supportive to provide both astrometric and photometric measurements. Photometric measurements,

more specifically light curves, are extremely significant in understanding the behavior of an RSO using ground-based measurements. Light curves measure the flux of photons across a wavelength (from the Sun) reflected by the object as collected by the observer on Earth. Typically, the light curve inversion procedure [9, 10] has been employed for asteroids, which is in its own domain for object modeling and characterization. Asteroids approximate to an ellipsoid shape (either convex or concave) with exceptions to uniquely-shaped ones. The surveys of celestial and stellar bodies [11, 12] are dissimilar to artificial space objects. The material properties of man-made objects are not always uniform throughout the surface. Additionally, the presence (or absence) of sharp glints in the light curve can indicate whether the object has flat reflective surfaces, and can constrain the rotation rate [13]. Hence, it is essential to determine a method to correctly analyze light curves of artificial RSOs.

Researchers have differed in their techniques utilized to estimate and model objects in the space catalog. After exploring several period estimation methods ranging across Fourier and phase-folding techniques, the method (or methods in conjunction) that performs most consistently for all applications, with an emphasis on artificial LEO object is selected. These methods were tested using ground-based observations of light curve data for various resident space objects that fall under a rigid body context (i.e. asteroids, satellites, probes, rocket bodies) and celestial objects like stars and extrasolar planets. The effect of varying sample size, the inadequacies in unevenly sampled data processing, autonomy of the method and complexity of parameters have been investigated. To account for heterogeneity in method parameters, each technique is tested with a range of values to optimize the rotational period.

Investigation of artificial space objects such as rocket bodies and satellites require a more complex polyhedron to estimate its shape. Various methods compute the light curves of irregularly shaped bodies at arbitrary viewing angles and illumination

geometries by integrating brightness. The more conventional approach is to compute surface integrals by polyhedral approximation with triangular facets (i.e. Delaunay triangulation) of different sizes based on the mesh and summing it over the facet areas. One of the more efficient methods, based on Lebedev quadrature, is function integration employed in light curve simulation. It has shown faster computational times than polyhedral sums and an increased accuracy regardless of noise in the data. It requires no collocation of the surface into a polyhedral approximation. Using synthetic light curves at varying angular rotational speeds and interpolated surface reflectance properties across the facets, the feasibility of using function integration with composite brightness functions is discovered.

Past techniques to classify RSOs have relied on estimation theory and include the development of multiple model adaptive estimation (MMAE), nonlinear state estimation, and full Bayesian inversion [8]. Although some of the above-mentioned methods also apply to artificial RSOs, they tend to be computationally expensive. State-of-the-art methods rely on well established physical models that are embedded in an inversion scheme capable of processing the data and estimate the model parameters. The inversion process requires the estimation of a large number of parameters. Methods that can provide a higher degree of accuracy, computational efficiency and reliability is where machine learning (data-driven classification) [14] comes into play. Deep learning and neural networks are also popular for space object classification. Multiple kernel learning (using Convolutional Neural Networks (CNN)) has been applied to geosynchronous satellites [15], a variation of CNN with Model-based Transfer learning [8] for space objects, as well as CNN-based classification using Hough space of LiDAR point clouds [16] have all been applied as data-driven approaches. A comparison of data-driven (Principal Component Analysis, CNN) with model-driven approaches (MMAE) [17] has also been performed for space objects. Instead of using

raw time series or texture features only, fused features of time series [18] has succeeded in classification of space objects, although it is applied to asteroid light curves. The literature review has shown methods for classifying RSOs, with some applying it to natural objects while others include artificial objects. CNN seems to be the only notable deep learning technique, however there are other types of networks such as Recurrent neural networks which are advantageous to this application. The use of Markov brains was proposed for on-board asteroid shape model determination [19]. The combination of RNN with the beneficial Hidden Markov model (HMM) is the technique utilized here to classify these objects by state of motion (tumbling vs. stabilized) and shape. A large bank of artificial space objects have been developed and modeled to create a training set. This two-stage classification scheme improves the accuracy by identifying and correcting misclassified samples.

The research objective is to classify an arbitrary object in LEO, given its photometric light curve, using the rotational period and shape efficiently. Some questions that have been addressed in the process are the following:

1. Is there an alternative to estimating the shape of an object using its light curve without prior knowledge on its correlated parameters?
2. What technique most accurately computes the spin rate of an artificial object that is in a tumbling state solely using its light curve?
3. Can we improve the computational efficiency of classifying RSOs using photometric light curves?

With the above-mentioned responses, we can then robustly estimate the shape of the object with supplemental information on its spin rate and categorize it appropriately.

Finally, the application of light curves to a planetary science problem that hasn't been explored much yet is the atmospheric modeling of Triton. The lack of information since Voyager 2, has made this a necessary topic of investigation. A better

understanding of Triton, Neptune's largest moon, can uncover the secrets behind the evolution of icy objects in the Solar system, including large moons, small Kuiper Belt Objects (KBOs) and dwarf planets that might share a similar history. Since Voyager 2 in August 1989 showing data of a dynamic atmosphere, only ground telescopes were able to capture data on Triton. Past literature has attempted to model the atmospheric figure by probing Triton's atmosphere with a stellar occultation from a group of sites. To observe the changes in atmosphere with time, light curves can be gathered within the central region to understand the structure. To quantify the distortion required to reproduce the measured light curve, a global model of the atmosphere of varying ellipticity can be constructed and fit using least-squares method. Using an orbiter, releasing hundreds of small satellites into orbit around Triton in delayed succession allows for an in-situ, simultaneous measurements, impossible to achieve using one operating probe. The simulated data (with additional astrometric data of Triton) can be 3D mapped to generate the atmospheric model and validate predictions of Triton's expanding atmosphere due to thermal properties of the surface and increase in pressure.

The organization of this report is as follows. First, we determine the optimal method for estimating the sidereal rotation period of artificial RSOs with an extension to asteroids and stellar transit light curves. The most accurate method is utilized to determine periodicity in the classification process. Next, we analyze computing surface brightness for artificial objects using quadrature schemes as opposed to the commonly used tessellation method for asteroids or pre-existing models. Following this, we examine the classification process using neural networks and the Hidden Markov model. Finally, the modeling of Triton's atmosphere is an augmentation of photometric light curve applications and concludes this report. Each chapter that

contains results uses simulated (and some real) examples with discussions succeeding them.

Chapter 2

Estimating Sidereal rotation period of RSOs

2.1 Introduction

Orbital debris exists in large quantities, crowding desired orbit regions. Resident Space Objects (RSOs), as defined by Segal et al. in [20], are constituted of natural and artificial objects such as asteroids, active and defunct satellites, spent rocket bodies and debris fragments of varying size. RSOs continue to increase in number and pose potential dangers to other space vehicles from the likelihood of collision (Kessler syndrome) [21, 22]. Space object characterization data, such as size and rotational period, can be determined using the reflected sunlight emitted from the artificial object (usually in the thermal wavelengths of the electromagnetic spectrum as noted in [23]). Each object in orbit can produce its own light curve, which is a plot of brightness measurements of the astronomical object seen by the observer as a function of time. The intensity of each measurement in light curves is dependent on the geometry relating Sun-spacecraft-observer, where the shaded yellow region is the solar phase angle, as seen in Fig. 2.1.

The photometric light curves caused by rotation of a non-spherical RSO has been shown to contain several important pieces of information: Wild, in ref [24], asserts that one can estimate the sidereal rotation period, spin axis orientation in space, and shape. Typically, a distinguishable feature in a light curve is selected, i.e. maximum or minimum measured brightness or a saddle point, and the re-occurrence of this feature in the light curve can give information on the object's periodicity. The angular speed of the RSO is approximated using the light curve period, as in the

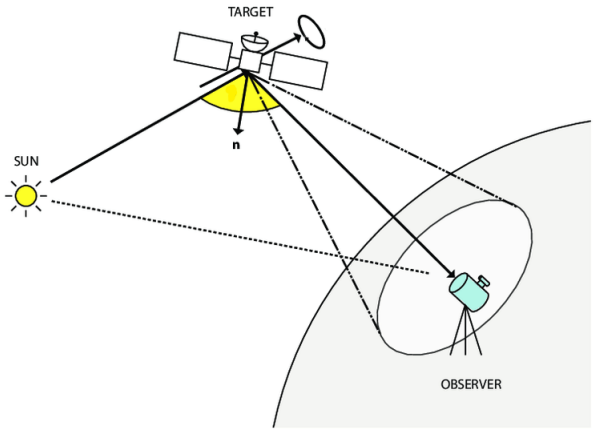

Figure 2.1: Simplified Sun-object-observer geometry involved in light curve acquisition. (Modified image) [4]

case of finding rotational state of uncontrolled disposed upper stages [25]. The time it takes for the RSO to rotate about its own spin axis relative to the fixed stars is otherwise known as sidereal rotation period. For simplicity, this will be referred to as rotation period henceforth in this paper similar to [26].

Evidenced by [27], uniformly spaced data obtained in intervals are typically analyzed by standard Fourier methods (based on Fast Fourier Transform) as well as the Method of Maximum Entropy. Most astronomical ground-based observations are difficult to achieve uniform spacing due to delegated windows for data collection, position of the object under observation and time-delay of information. Other reasons such as weather and diurnal, lunar or seasonal cycles as effecting factors where sampling is concerned is discussed in [28].

Irregularity in Astronomical time series data makes it difficult for application of standard Fourier-based analysis techniques. Since 1975, when the discrete Fourier transform was first introduced as a period finding algorithm [29], many others have emerged until the more recent correntropy technique. Choosing 'the optimum' (if any exists) technique is difficult due to influencing factors such as temporal coverage,

number of data points, sampling rates and prior knowledge of the object. This problem has been investigated in [30] by using numerical simulations to compare discrete Fourier transforms, minimum string length and phase dispersion minimization, although none was declared as more advantageous than others. In comparing model function and phase binning methods using hypothesis-testing theory, Schwarzenberg-Czerny found that methods such as Lomb-Scargle periodogram using smooth model functions are more sensitive than those using phase binning [31]. Another observation was that many phase binning methods produced the same result for identical number of bins. Additionally, phase dispersion minimization is regarded as an approximation to Lomb-Scargle with the latter as the best periodogram technique [32]. Distefano et al. found Lomb-Scargle as the most efficient method with a maximum recovery rate of 60% when comparing it with discrete Fourier transform and phase dispersion minimization to compute rotation periods of solar-like stars from unevenly sampled synthetic data of *Gaia* [33]. A single method can recover period values for up to 80% of the cases, but the accuracy is unknown [34]. Combining methods can increase the percentage although the identification of which method directs to fidelity is still unknown. A thorough comparison of period finding algorithms was also performed by Graham et al. in 2013 [35]. However, a commonality that all the previously mentioned literature have, are their application to cases of variable stars (eclipsing, binary, pulsating and stationary). In [35], they used large collections of time series data from searches for microlensing (i.e. MACHO), exoplanets (e.g. Convection, Rotation and planetary Transits (CoRoT)), and among others, synoptic sky surveys such as Catalina Real-time Transient Survey (CRTS), and All Sky Automated Survey (ASAS). It was the first survey using real data although it considers only a wide range of variable stellar classes.

Among related methods, a multi-band periodogram introduced in [36] significantly improves period finding for randomly sampled multi-band light curves (e.g. Panoramic Survey Telescope and Rapid Response System (Pan-StaRRs)). The slotted correntropy [37] and its counterpart, conditional entropy [38], have outperformed slotted correlation, string length, Lomb-Scargle periodogram on the MACHO survey. A nonparametric Bayesian model, based on Gaussian Processes (GP), was presented in [39] showing better results especially when the light curve does not exhibit a sinusoidal shape, once again using variable stars' datasets.

These surveys of celestial and stellar bodies [11, 12] are dissimilar to artificial space objects. The material properties of man-made objects are not always uniform throughout the surface. Additionally, the presence (or absence) of sharp glints in the light curve can indicate whether the object has flat reflective surfaces, and can constrain the rotation rate [13].

Light curves are affected by several noise sources such as light contamination from other celestial sources near the line of sight, the atmosphere, and detection sensitivity of the apparatus. Other sources such as equipment positioning, calibration, and maintenance impact the quality of the light curve according to [23]. Hence, multiple periods can co-exist in the time series for a day's or year's worth of data collection. In order to distinguish false periods and understand which technique works best, this paper will investigate the viability of three types of time-series analysis: 1) least-squares methods, 2) Fourier methods, and 3) phase-folding methods. The use of slotted correntropy to estimate periods of stellar light curves was introduced in 2011, and the Correntropy Kernel Periodogram (CKP) in 2012 by P. Huijse et. al as a new metric for finding periodicities. Both developments were based on the information theoretic concept of correntropy while the latter combined it with a periodic kernel. Centered autocorrentropy is explored as one of the signal processing techniques to

estimate periods of artificial tumbling space objects. In this thorough comparison, we will examine several variables such as duration of data collection, size of data set, uniformly and non-uniformly sampled data as well as user inputs (intermediate parameters that may need to be specified for further processing).

The detection of periodicity for astronomical objects is not limited to asteroids, satellites and rocket debris, but also include stellar objects and extrasolar planets. These are of high importance in astronomy and in order to classify variable stars and discovering extrasolar planets, the period is a pivotal characteristic. It can also aid in estimating other parameters such as mass, and distance to Earth [23]. Thus, these techniques will be employed to both kinds of light curve data; specifically, Asteroid 43 Ariadne, artificial low-earth orbit (LEO) objects employing geometric shapes (simple and composite), and a cluster object HAT-138-0001727.

Our main contribution is the presentation of a comparative study of several time-series analysis methods with applications to a wide range of time series data (real and synthetic light curves) e.g. unevenly spaced data from an asteroid, 1U Cubesat, NASA Regolith Advanced Surface Systems Operations Robot (RASSOR) Bucket Drum, Pioneer 9 disks and probe, Pioneer 10 probe, box-wing satellite, a rocket nose cone, and a stellar transit light curve. Through these applications, we seek to find the one method among those studied, that performs most consistently for all of this data. We feel that through the many kinds of light curves analyzed, we are able to communicate to the wider community "the method" to go for when they need to obtain a reasonable estimate of the sidereal rotation period of a space object, with an emphasis on artificial LEO object.

The following sections will provide a mathematical background for each of the methods prior to applying them to actual observed data from ground as well as a simulation generating synthetic uniformly-sampled light curves of which the process

has also been outlined in detail. The simulation results help us conclude which methods work best for estimating sidereal rotation periods of resident space objects, depending on the quality of light curves and sampling frequency.

2.2 Time Series Analysis for Sidereal Rotation Period Estimation

Commonly utilized in time-series analysis is the least-squares method; it attempts to fit a given set of points to a curve by minimizing the sum of the squares of the offsets of the points from the curve. The sum of the squares of the offsets is used instead of the offset absolute values because this allows the residuals to be treated as a continuous differentiable quantity. However, outliers can have an irregular effect on the fit, which may be detrimental to the objective. For nonlinear least squares fitting to a number of unknown parameters, linear least squares fitting may be applied iteratively to a linearized form of the function until convergence is achieved. Herein, we use the formulations from [40]. Let the function to be approximated be $h(x, y, z, \cdots)$ and the approximating function be $H(x, y, z, \cdots; \alpha, \beta, \gamma, \cdots)$ where $\alpha, \beta, \gamma, \cdots$ are the unknown parameters. The residuals at the points $(x_i,\ y_i,\ z_i,\ \cdots)$ for $i = 1,\ 2,\ \cdots,\ n$ are

$$f_i(\alpha, \beta, \gamma, \cdots) = H(x_i, y_i, z_i, \cdots; \alpha, \beta, \gamma, \cdots) - h(x_i, y_i, z_i, \cdots) \tag{2.1}$$

and the least squares criterion requires the minimization of $s(\alpha, \beta, \gamma, \cdots) = \sum_1^n f_i^2$.

The following is an example of the least-squares criteria. The Epoch method designed for amateur astronomers in [24], uses multiple light curves and its respective difference in period to compute the spin axis (pole) orientation and direction of rotation. The magnitude of periodic difference is a function of the object's spin axis orientation with respect to the observer-object-Sun geometry and direction of rotation as defined by [41] in their study. In the context of asteroids, not all rotate at the same

rate. Therefore, some may require a single light curve spanning several hours to find the period of rotation while others need multiple to observe all facets of the geometry. The advantages of data collection over several months or years for characteristics of shape and surface are brought to the reader's attention in [24]. While there are advantages to long-scale data collection (as shown in [24]), this is not always practical (especially for amateur astronomers, or for objects very near Earth).

Composite light curves (obtained through differential charge-coupled device (CCD) photometry) from three or more epochs are fit with a low order Fourier series to determine the fundamental frequency and its corresponding period [42]. We will examine the basis for Fourier and Phase-folding methods in the following sections.

2.2.1 Fourier Methods

A given signal travelling through a medium creates sources for scattering off the components in the sample. This ripple effect leads to secondary waves that interfere with one another. This phenomenon parallels the Fourier transform in wave-interference. The patterns of constructive and destructive interference give rise to dominant peaks in the frequency domain and low levels of noise for the latter.

While several of these methods are well known/studied and it would seem redundant to include the definitions; for the sake of completeness and to allow the reader to progress through the methods seamlessly and notice the subtleties, we choose to retain these definitions and well known details.

2.2.1.1 Fast Fourier Transform

The Fast Fourier Transform (FFT) algorithm computes the Discrete Fourier transform (DFT) of a sequence that samples a signal over a period of time and splits it into signals with respective amplitude and phase components at individual frequencies.

Consider a continuous function $g(t)$ sampled at regular intervals, Δt. The Fourier transform is defined as a function of frequency, f as shown below.

$$\hat{g}(f) \equiv \int_{-\infty}^{\infty} g(t) e^{-2\pi i f t} \mathrm{d}t \tag{2.2}$$

An infinite time and continuous signal $g(t)$ that is observed on a regular grid with spacing Δt has a Fourier transform that can be written as a Fourier sum rather than its integral form as shown in equation (2.2). The Fourier Transform of the observed signal is then,

$$\hat{g}_{obs}(f) = \sum_{n=0}^{N} g_n e^{-2\pi i f n \Delta t} \tag{2.3}$$

where g_n, a uniformly-spaced function, is $g_n = g(n\Delta t)$ and $n = 0, 1, 2, ..., N$. Accounting for Nyquist aliasing, the only relevant frequency range is $0 \leq f \leq 1/\Delta t$ as observed in [28]. We can then define N evenly-spaced frequencies with $\Delta f = 1/(N\Delta t)$ covering this range.

Denoting $\hat{g}_s \equiv \hat{g}_{obs}(s\Delta f)$, we can re-write equation (2.3) as

$$\hat{g}_s = \sum_{n=0}^{N} g_n e^{-2\pi i s n/N} \tag{2.4}$$

which is the standard form of the Discrete Fourier transform (DFT).

The frequency spacing (Δf) of DFT is uniform and favorable in terms of both the Nyquist sampling limit and the finite observing window [28]. It is also well known that, FFT is widely prevalent in signal processing, specifically for estimating power spectral density (PSD) from time-domain signals.

We denote the Fourier Transform operator as $F\{g\} = \hat{g}(f)$ and to eliminate the complex components and remove the phase, we square the amplitude of the resulting transform which is commonly known as the power spectral density (PSD) or power

spectrum, $PSD_g \equiv |F\{g\}|^2$. PSD is a positive real-valued function of the frequency f that distinguishes each individual frequency that is present in the total signal.

Note, FFT is advantageous due its to high processing speeds and reduces the complexity from $O(n^2)$ to $O(n \log n)$ where n is the data size. Linearity of the transform is inferred in [28] to the Fourier transform directly measuring periodic content in a continuous function since the signal is made up of a sinusoidal components. *However, it does require uniformly-spaced data which is not always the case with astronomical data pertaining to Space objects.* In [43], it is remarked that in order to get evenly sampled data for FFT, interpolation and resampling created inaccuracies in PSD estimation.

Many programming languages and signal processing blocksets have built-in functions for the Fast Fourier Transform which are capable of handling large volumes of data; however there are recursive and iterative algorithms available of which one is shown below for implementation.

Algorithm 1 Fast Fourier Transform algorithm

procedure FFT(x)
  $N \leftarrow length(x)$
  $n \leftarrow 2^{\log_2(N)}$
  $z \leftarrow [0]_{1xn}$
  $sum \leftarrow 0$
  for $k \leftarrow 1, n$ **do**
    for $j \leftarrow 1, N$ **do**
      $sum \leftarrow sum + x(j) * e^{\frac{-2\pi j(j-1)(k-1)}{n}}$
    end for
    $z(k) \leftarrow sum$
    $sum \leftarrow 0$
  end for
return z
end procedure

2.2.1.2 Fractional Fourier Transform

The fractional Fourier transform (FRFT) is a generalization of the Fourier transform and it implements the order parameter, α, which acts on the Fourier transform operator [44]. We obtain the Fourier transform when $\alpha = \pi/2$, whereas for $\alpha = 0$, we obtain the signal itself. Any intermediate value of α, $(0 < \alpha < \pi/2)$ produces a signal representation that can be considered as a rotated time-frequency representation of the signal [44]. Applications of the discrete counterpart of the FRFT as a signal processing tool include filtering, radar, pattern recognition, and wireless communications.

Since the FRFT is characterized by quadratic complex exponential kernels, it is often not possible to evaluate these by direct numerical integration because the fast oscillations of the phase of the complex exponential would imply excessively large sampling rates [45]. We can decompose these integral transformations into a succession of simpler operations, such as chirp multiplication, chirp convolution, scaling, and Fourier transformation. However, these methods might also require sampling rates that are significantly higher than the Nyquist rate, depending on α and particular decomposition employed [45]. This, in turn, results in greater time of computation, larger numerical inaccuracy, and the need for more memory. As such, this method does not seem to be a viable option for period estimation of artificial RSOs and we will not include this in the roster of signal processing techniques that will be tested further.

2.2.1.3 Classical Periodogram

Applying the definition of the Power spectrum to the Discrete Fourier Transform defined by [28] previously, and multiplying it by a factor of $1/N$ results in the classical periodogram.

$$P_C(f) = \frac{1}{N}\left|\sum_{n=1}^{N} g_n e^{-2\pi i f t_n}\right|^2 \tag{2.5}$$

Primarily, the classical periodogram is optimal for the uniform sampling case as it is able to capture all the frequency components. While the periodogram follows the definition of the power spectrum, conceptually; the former is an estimator of the latter. These terms are used interchangeably in the astronomy community. Extensions of the classical periodogram (such as the Lomb-Scargle periodogram which will be discussed later) have intrinsic variances in cases even where there are infinite number of observation points [28].

Equation (2.5) can be expanded and re-writen using Euler's theorem to eliminate the complex variables.

$$\begin{aligned} P_C(f) &= \frac{1}{N}\left|\sum_{n=1}^{N} g_n[\cos(-2\pi f t_n) + i\sin(-2\pi f t_n)]\right|^2 \\ &= \frac{1}{N}\left|\sum_{n=1}^{N} g_n[\cos(2\pi f t_n) - i\sin(2\pi f t_n)]\right|^2 \\ &= \frac{1}{N}\left[\left(\sum_{n=1}^{N} g_n\cos(2\pi f t_n)\right)^2 + \left(\sum_{n=1}^{N} g_n\sin(2\pi f t_n)\right)^2\right] \end{aligned} \tag{2.6}$$

In agreement with [28], the classical periodogram is useful for identifying periodic signals from non-periodic data. However, for a case of *non-uniform sampling*, the periodogram is harder to distribute using a Chi-squared term. As discussed in [46], two prevalent problems with the classical periodogram include statistical difficulties

Algorithm 2 Classical Periodogram algorithm

procedure CP(t, x, fs)
  t is the time vector
  x is the magnitude vector
  fs is the frequency search range (low, high) with interval df
  $N \leftarrow length(t)$
  $d \leftarrow x - mean(x)$
  $f_{index} \leftarrow fs_{low}$
  $n \leftarrow (fs_{high} - fs_{low})/df$
  $frequency \leftarrow [0]_{nx1}$
  $power \leftarrow [0]_{nx1}$
  $k \leftarrow 1$
  while $f_{index} < fs_{high}$ **do**
    $frequency(k) \leftarrow f_{index}$
    $power(k) \leftarrow \frac{|\mathbf{sum}(d * e^{(-2\pi i f_{index} t_k)}|^2}{N}$
    $f_{index} \leftarrow f_{index} + df$
    $k \leftarrow k + 1$
  end while
return $power, frequency$
end procedure

and spectral leakage. A more generalized form took its place and is known as the Lomb-Scargle periodogram to ensure that it holds this property.

Algorithm 2 can be appended to include normalization of the periodogram by associating noise with the variance of the signal x and dividing the power by the variance. Sorting the power spectrum in increasing order of frequency makes it facile for visual display.

2.2.1.4 Lomb-Scargle Periodogram

The Lomb-Scargle Periodogram, combined several properties such that it was able to simplify to the Classical form for equally-spaced data, and is not influenced by global time-shifts in the observations. The difference according to [28] lies in the

proportionality multiplied by each term, no longer $1/N$ which is expected for complete phase sampling at each frequency. The Periodogram function is expressed below:

$$P_{LS}(f) = \frac{1}{2}\left\{\frac{(\sum_n g_n \cos(2\pi f[t_n - \tau]))^2}{\sum_n \cos^2(2\pi f[t_n - \tau])} + \frac{(\sum_n g_n \sin(2\pi f[t_n - \tau]))^2}{\sum_n \sin^2(2\pi f[t_n - \tau])}\right\} \tag{2.7}$$

where τ is defined for each frequency f so that time-shift invariance is non-existent:

$$\tau = \frac{1}{4\pi f}\arctan\left(\frac{\sum_n \sin(4\pi f t_n)}{\sum_n \cos(4\pi f t_n)}\right) \tag{2.8}$$

The Lomb-Scargle Periodogram ensures accuracy for non-uniform sampling provided that the data has uncorrelated white noise [28].

Spectral leakage remains a challenge because frequencies not integral multiples of the DFT bin, spread over other bins as well. This creates false alarms when searching for the dominant frequencies. The periodogram power is normalized by the inverse of the variance of the original signal data values. This scaled power has an exponential distribution as shown in [47] for Gaussian noise data values and a large number of observations.

Numerical programming languages like MATLAB have built-in functions for the Lomb-Scargle Periodogram (i.e. plomb) where frequency search ranges do not need to be specified. The algorithm in itself is quite similar to Algorithm 2 (Classical Periodogram) with a modification in line 14. The power computed is defined using equation 2.7 instead.

2.2.2 Phase-Folding Methods

These methods depend on folding observations as a function of phase, computing a cost function across the phased data (often within bins constructed across the phase

space) and optimizing this cost function across candidate frequencies. In epoch folding as noted by [23], a trial period P_t is used to obtain a phase diagram of the light curve by applying the modulus transformation of the time axis:

$$\phi_i(P_t) = \frac{t_i \mathbf{mod} P_t}{P_t} \tag{2.9}$$

where t_i are the time instants of the light curve. The trial period P_t is found by a brute-force search across the range of possible values. Conforming to [23], if the true period is used to fold the light curve (ie. overlapping segments), the periodic shape will be clearly seen in the phase diagram. If an incorrect period is used, the phase diagram will look like noise. An additional step is to separate the segmented light curve into bins and the ratio of the intra-bin variance to inter-bin variance is also computed.

2.2.2.1 Minimum String Length

The light curve is folded using a trial period as mentioned earlier and the sum of distances between consecutive points in the folded curve is computed [23]. The true period is estimated by minimizing the string length on a range of trial periods. The true period is expected to result in the most controlled folded curve, essentially providing the 'minimum total distance' between points.

[48] used a method which is a true 'string-length' technique. In this method, the quantity to be minimized is simply the sum of the lengths of line segments joining successive points (m_i, ϕ_i) in a phase diagram. The period chosen is that for which the quantity $\sum_{i=1}^{n-1}[(m_i - m_{i-1})^2 + (\phi_i - \phi_{i-1})^2]^{1/2} + [(m_1 - m_n)^2 + (\phi_1 - \phi_n + 1)^2]^{1/2}$ is a

Algorithm 3 Minimum String Length algorithm

procedure MSL(t, x, fs)
  t is the time vector
  x is the magnitude vector
  fs is the frequency search range (low, high) with interval df
  $j \leftarrow 1$
  for all $k \in fs$ **do**
    $f \leftarrow folding(x, 1/k)$ This folds x into a period $1/k$
    $frequency(j) \leftarrow k$
    $stringlength(j) \leftarrow$ SLEN(f)
    $k \leftarrow k + df$
    $j \leftarrow j + 1$
  end for
  $index \leftarrow min(stringlength)$
  $MinFrequency \leftarrow frequency(index)$
return $frequency, stringlength, MinFrequency$
end procedure

procedure SLEN(c)
  $dx \leftarrow diff(c(:, 1))$
  $dy \leftarrow diff(c(:, 2))$
  $c \leftarrow \sqrt{(dx^2 + dy^2)}$
  $length \leftarrow sum(c)$
return $length$
end procedure

minimum, with n the number of observations. The algorithm to find the true period is shown in Algorithm 3.

2.2.2.2 Phase Dispersion Minimization

Period determination using Phase dispersion minimization distinguishes between trial periods, in which the period producing the least observational scatter (dispersion indicator) about the mean light curve is chosen in line with [49]. It is beneficial for non-sinusoidal light curves where there are scarce observations over a range-bound duration. An optimum light-curve shape is found, which is subtracted from measured

data for other periods to be searched. Data are folded modulo many periods, grouped into phase bins and intra-bin variance is compared to inter-bin variance using χ^2.

Stellingwerf's method [49] takes observational errors into account and gives useful results as the database increases in size; [50] adds it is particularly helpful when searching for secondary frequencies of low amplitude in variable stars. The following was proposed in [49].

Given a discrete set of observations $\{(x_1, t_1), (x_2, t_2), \ldots, (x_N, t_N)\}$ representing the magnitudes and observation times respectively and N is the total number of points. The variance of $\vec{x}$ is simply given by $\sigma^2 = \frac{1}{N-1}\sum(x_i - \bar{x})^2$ where $\bar{x} = \frac{1}{N}\sum x_i$ is the mean. For any subset of x_i we define the sample variance s^2 exactly as σ^2. Choosing M distinct samples having variances s_j^2 respectively for $j = 1, \cdots, M$ and containing n_j data points, the overall variance for all the samples is then given by

$$s^2 = \frac{\sum[(n_j - 1)s_j^2]}{\sum(n_j) - M} \tag{2.10}$$

The goal is to minimize the variance of the data with respect to the mean light curve. Let P_t be the trial period and the phase vector subsequently would be $\vec{\phi}$. For each observation,

$$\phi_i = \frac{t_i}{P_t} - \text{int}\left(\frac{t_i}{P_t}\right) \tag{2.11}$$

where int$(\cdot)$ represents the integer part of the value. Equivalently, $\vec{\phi} = \vec{t}\ \mathbf{mod}(P_t)$. Choosing M samples from $\vec{x}$ such that all members of sample j have identical ϕ_i, these samples are then split into a number of bins, where some may overlap or not be chosen at all. The variance of these samples gives a measure of the scatter around

the mean light curve defined by the means of the x_i in each sample, considered as a function of ϕ. The phase dispersion indicator is then given by

$$\theta = \frac{s^2}{\sigma^2} \tag{2.12}$$

If the trial period P_t is not the true period, then $\theta \approx 1$ since $s^2 \approx \sigma^2$. However, if it is correct, then θ will reach a local minimum as near to zero as possible. We seek periods at which the amplitude of the mean curve is a maximum, which in most cases will correspond to minimum phase dispersion. The bin structure is up to the user to define as suggested in [49], but following a standard structure, we can split the unit interval into N_b bins, each with length $1/N_b$. This resembles the least-squares method mathematically, but it fits relative to the mean curve as defined by the averages of each bin instead of a Fourier series. Obtaining the best fit curve and period occur simultaneously, so it is computationally efficient. Phase dispersion minimization minimizes the dispersion of data at constant phase and is a Fourier method of infinite order since all harmonics are included in the fitted function [49]. This technique to find the phase dispersion indicator θ has been adapted in Algorithm 4.

2.2.2.3 Autocorrelation Function

The autocorrelation function (ACF) is a measure of how identical a measured quantity at a given time is related to itself at another time. The ACF can also be viewed as a measure of the predictability of a process or signal, based on past data [51]. Prediction of a process at a future time '$t + \Delta t$' is valid such that the correlation function value at lag 'Δt' is large. As soon as the correlation function diminishes,

Algorithm 4 Phase Dispersion Minimization algorithm

procedure PDM($t, x, fs, Nbin$)
  t is the time vector
  x is the magnitude vector
  fs is the frequency search range (low, high) with interval *df*
  $Nbin$ is the number of bins in the folded period
  $I \leftarrow 0$
  for all $k \in fs$ **do**
    $I \leftarrow I + 1$
    $f \leftarrow [t * k - floor(t * k), x]$
    $Data \leftarrow$ Binning folded data, f with bin size, $1/Nbin$
    $N \leftarrow length(Data)$
    $S2 \leftarrow \mathbf{sum}((N-1) * Variance(Data))/(\mathbf{sum}(N) - Nbin)$
    $\theta(I) \leftarrow S2/Variance(x)$
    $frequency(I) \leftarrow k$
  end for
return $frequency, \theta$
end procedure

the similarity of the signal to its prior knowledge disappears, and the signal becomes unpredictable.

For observations $(x_1, \cdots, x_n)$ of a time series, the sample autocorrelation function is $\hat{\rho}(h) = \frac{\hat{\gamma}(h)}{\hat{\gamma}(0)}$ where, $\hat{\gamma}(h)$ the sample autocovariance function is

$$\hat{\gamma}(h) = \frac{1}{n} \sum_{t=1}^{n-|h|} (x_{t+|h|} - \bar{x})(x_t - \bar{x}) \tag{2.13}$$

for $-n < h < n$ and the sample mean is defined as $\bar{x} = \frac{1}{n} \sum_{t=1}^{n} x_t$

The autocovariance of a zero-mean random process x is defined by [51] as the expectation of the product of the values of x observed at times separated by the *lag*. The ACF is equivalent to the autocovariance normalized to 1 at $t = 0$. The Autocorrelation theorem equates the power spectrum of a stationary random process to the Fourier transform of its autocorrelation function [51]. Therefore, the ACF

can be estimated by computing the inverse Fourier transform of the square of the complex absolute value of the Fourier transform, since the latter is an estimate of the power spectrum. The autocorrelation sequence of a periodic signal has characteristics resembling the original signal. Thus, autocorrelation can validate repeated sequences and determine their durations. It is advantageous for large durations and can amplify the peaks. However, to determine the dominant period, significance threshold needs to be specified. Multiples of the same period are also peaks, thus requiring post-processing. Algorithm 5 describes the methodology to find the sample autocorrelation function and this can be repeated for multiple lags.

Algorithm 5 Autocorrelation Function algorithm

procedure ACF(x, p)
  p is the lag
  x is the magnitude vector
  $N \leftarrow length(x)$
  $xbar \leftarrow mean(x)$
  $num \leftarrow [0]_{(N-p)x1}$
  for $i \leftarrow (p+1), N$ **do**
    $num(i) \leftarrow (x(i) - xbar) * (x(i-p) - xbar)$
  end for
  $den \leftarrow (x - xbar)^T * (x - xbar)$
  $result \leftarrow$ **sum**$(num)/den$ **return** $result$
end procedure

2.2.2.4 Centered Correntropy

Correntropy measures similarities between two observed sets distinguished by a finite time delay in the input domain. The similarities are measured in terms of inner products in a high-dimensional kernel space. A kernel can be viewed as a similarity measure for the data. Kernels are viewed by [52] as covariance functions for correlated

observations at different points of the input domain. The Gaussian kernel which is translation-invariant, is defined by [23] as follows:

$$G_\sigma(x-z) = \frac{1}{\sqrt{2\pi}\sigma}\exp(-\frac{||x-z||^2}{2\sigma^2}) \tag{2.14}$$

where σ is the kernel size or bandwidth. The kernel size can be construed as the resolution for the similarity search to be performed in the high-dimensional kernel feature space. The kernel size gives the user the ability to control the emphasis given to the higher-order moments with respect to second-order moments, a finding of [23]. For large values of the kernel size, the second-order moments have more relevance and the correntropy function approximates the conventional correlation. If the kernel size is too small, the correntropy function will not be able to differentiate between signal and noise and instead approximates the Dirac delta function.

Through the formulation from [23], for a discrete strictly stationary random process X_n, the univariate centered correntropy function or centered autocorrentropy is

$$\hat{U}_\sigma[m] = \frac{1}{N-m+1}\sum_{n=m}^{N} G_\sigma(x_n - x_{n-m}) - \frac{1}{N^2}\sum_{n=1}^{N}\sum_{m=1}^{N} G_\sigma(x_n - x_m) \tag{2.15}$$

where N is the number of samples, σ is the kernel size used in the Gaussian kernel and $m \in [1, N]$ is the discrete time lag. It is ideal to choose a lag large enough so there are enough samples to estimate correntropy.

The Fourier transform of the centered autocorrentropy function is called correntropy spectral density (CSD) and can be written as

$$P_\sigma[f] = \sum_{m=-\infty}^{\infty} \hat{U}_\sigma[m]\exp(-2\pi i f\frac{m}{F_s}) \tag{2.16}$$

where f is the variable frequency, F_s is the sampling frequency and i is the imaginary unit number. The CSD can be considered as a generalized power spectral density (PSD) function although it does not measure power, rather an estimator based on kernel size [23]. For a large kernel size, CSD approximates PSD. Ref. [53] alluded to correntropy being used as a discriminatory metric for the detection of nonlinearities in time series. An ever-present challenge is choosing a precise maximum frequency to be searched for every set of data as well as the number of lags. This involves a trial-and-error process to ensure accuracy.

Algorithm 6 Centered Autocorrentropy algorithm

procedure CORRENTROPY(x)
  x is the magnitude vector
  σ is the gaussian kernel size
  $L \leftarrow round(0.5 * length(x))$ number of lags to consider
  V is the centered temporal correntropy of x using L and σ
  $E \leftarrow$ eigenvectors of V
  $fmax$ is the maximum frequency to be searched
  $i \leftarrow$ linearly-space vector from 0 to $fmax$ with interval $L/2$
  E_{end} is the last eigenvector
  $f \leftarrow \mathbf{FFT}(E_{end})$
  $Plot|f(1:L/2)|vs.i$ for the periodogram
  $frequency \leftarrow$ maximum peak in periodogram
return $frequency$
end procedure

2.3 Application to Case Studies

Computing the sidereal rotation period for a well defined uniformly spaced time series is trivial once the analysis is completed. From the periodogram, the frequency at which the highest peak occurs is defined as f_0 and subsequently, the rotational period about its own spin axis is $T = \frac{1}{f_0}$. For other methods that do not

use power spectral density, the frequency that satisfies its (the method's) *respective condition* is considered as f_0. In what follows test cases of RSOs of both uniformly and non-uniformly sampled light curves have been taken and their results (plotted in MATLAB) are shown below.

2.3.1 Unevenly sampled Sinusoidal Data

Let us assume the light curve for some RSO is obtained as a time-series with an underlying sinusoidal trend, $y_k = \sin k\Delta t + 5\sin 3k\Delta t + \nu_k$, where ν_k is Gaussian white noise and $k = 0 \ldots 100$ and $\Delta t = 0.1$s. The data points were unevenly sampled as shown in Figure 2.2. The different methods described in the previous section have been applied to determine the fundamental frequency producing the following results.

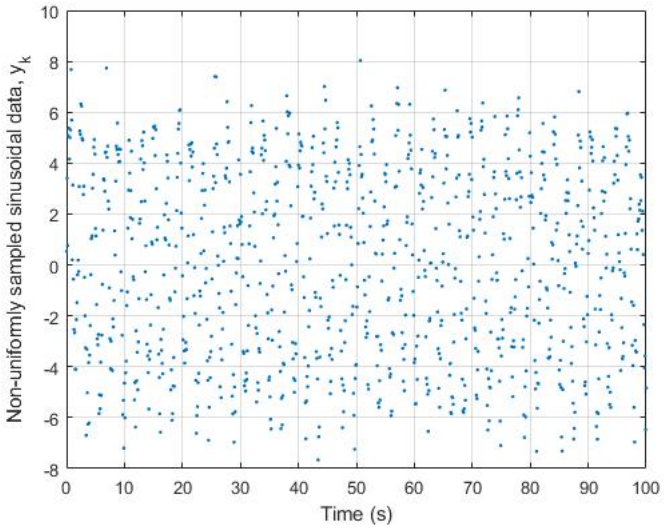

Figure 2.2: Light curve of non-uniformly sampled data

Table 2.1: Computed Rotational Period of non-uniformly sampled sinusoidal data and errors associated with different methods

Method	Computed Rotational Period (s)	Error (%)
Fast Fourier Transform	1.1636	44.3
Classical Periodogram	2.0833	0.3
Lomb-Scargle Periodogram	2.0921	0.1
Minimum Curve Length	2.0987	0.4
Phase Dispersion Minimization	2.0921	0.1
Autocorrelation Function	2.1750	4.1
Centered Correntropy	2.0870	0.1

From Table 2.1, it is observed that FFT has a computed rotational period of 1.1636 s (as expected) while the rest are relatively close to each other. This can be attributed to the lack of processing capability of Fast Fourier Transform with unevenly sampled data, as it requires a uniform sampling frequency for accurate results. The expected value for the rotational period is 2.0898 s and the errors in the experimental values are noted above in percentages.

Of all the methods, the Lomb-Scargle periodogram, Phase dispersion minimization and centered correntropy displayed the least error from the expected values at 0.1% each. This difference is small enough and almost negligible to consider these methods an accurate approximation for rotational period estimation.

Two of the methods (Autocorrelation function and Phase Dispersion Minimization) require user-defined parameters such as lags and number of bins respectively. Although it is difficult to choose a value large enough to estimate the correct period, *it is commonly misconstrued that there exists a linear relationship between the parameter and the estimated period.* The following tabulated data can shed some light that this is in fact not the case. The accuracy of the period is not dependent on the proximity to the optimal number of lags or bins.

Table 2.2: Table of rotational periods of non-uniformly sampled sinusoidal data using Autocorrelation function and varying lags (Top to Bottom: 10, 50, 75, 90, 100)

Number of Lags	Computed Rotational Period (s)
10	ERR
50	2.1000
75	1.8500
90	2.4000
100	2.1750

Table 2.3: Table of rotational periods of non-uniformly sampled sinusoidal data using phase dispersion minimization and varying number of bins (Top to Bottom: 10, 50, 75, 90, 100)

Number of Lags	Computed Rotational Period (s)
10	2.0921
50	2.0921
75	2.0921
90	2.0921
100	0.9452

The 'ERR' indicated in Table 2.2 for 10 lags is due to the distance between peaks on the autocorrelation exceeding the threshold, making it difficult to compute the period. The ACF plots differ only in the addition of data making it more detailed and filling in the gaps from the underlying trend as the number of lags increase.

It is important to note that for the results in Table 2.3, the frequency search range remained constant at $[0, 2]$ Hz with an interval of 0.002 Hz. It can be noted that in Table 2.3, the rotational period remains consistent for number of bins from 10 to 90, however drops drastically when the number of bins exceeds a limit at 100. More specifically, the frequency at which minimum dispersion occurs stays constant as the number of bins increase from 10 to 90, however the dispersion indicator magnitude varies. The dispersion in phase is existent at multiple frequencies when the number of

bins increase as illustrated in Table 2.3. The maximum lags must be large enough, however not so large that it permutes unnecessarily.

2.3.2 Light curve of Asteroid 43 Ariadne

43 Ariadne is a sizeable main-belt asteroid. The relative light curve points were obtained from the test file in Database of Asteroid Models from Inversion Techniques (DAMIT) Lightcurve Inversion software[1] and the best solution generated through a convex optimization is $T = 5.761985$ hrs and a spin pole orientation of $\lambda = -15°,\ \beta = 253°$.

The appropriate light curve (Fig. 2.3) and the plots corresponding to each analysis method (Figs. 2.4 and 2.5) is depicted below.

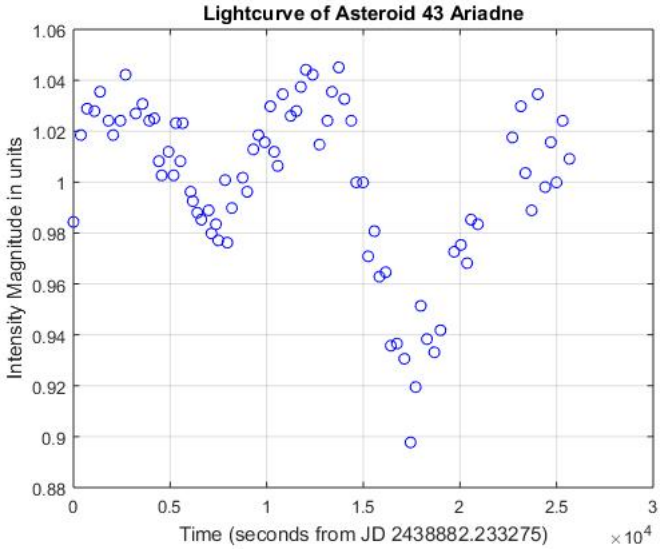

Figure 2.3: Light curve of Asteroid 43 Ariadne

[1] `https://astro.troja.mff.cuni.cz/projects/asteroids3D/web.php?page=download_software`

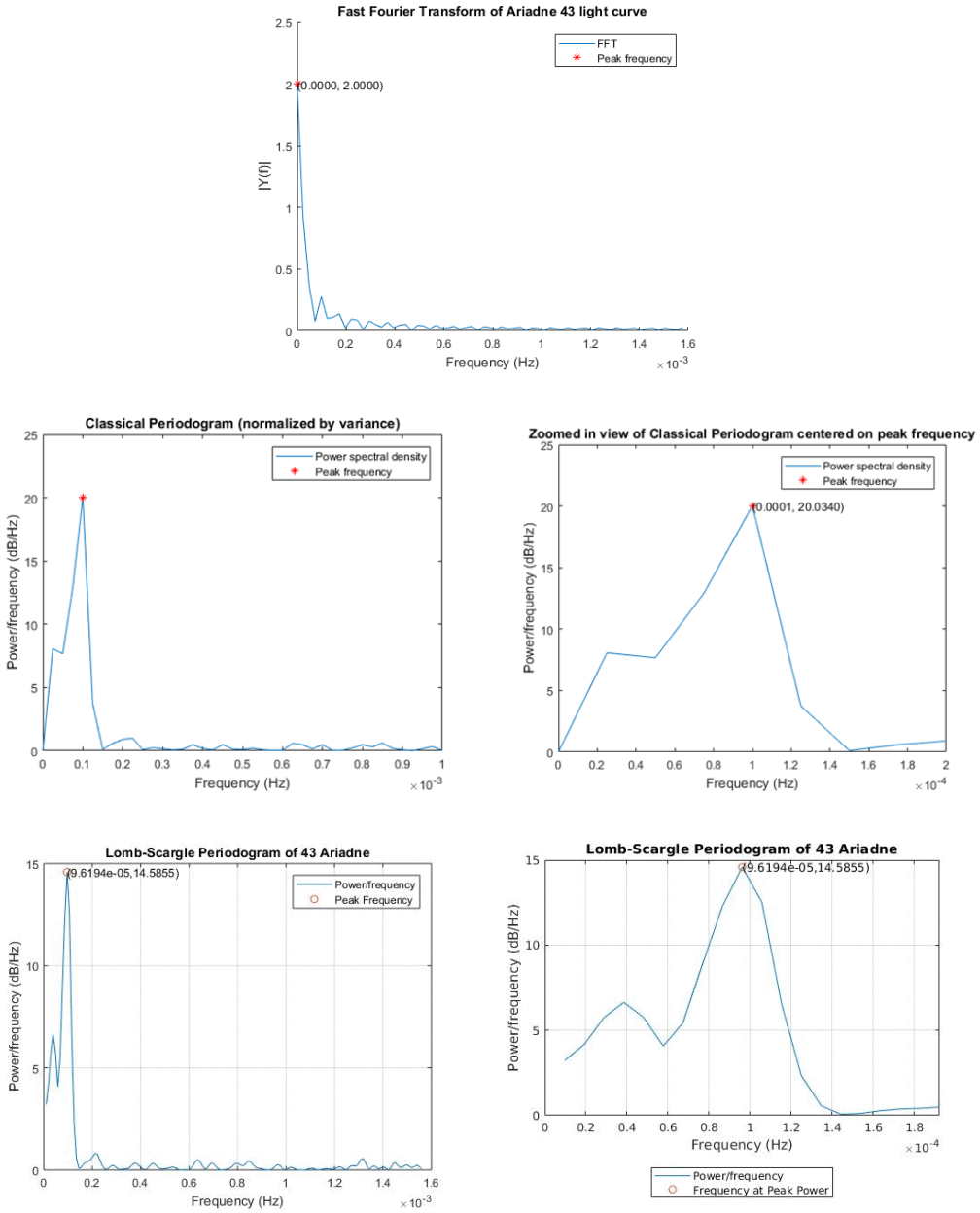

Figure 2.4: Fourier-based methods on asteroid 43 Ariadne's light curve (Top to bottom): fast fourier transform, classical periodogram and zoomed-in view centered at peak frequency, Lomb-Scargle periodogram and zoomed-in view centered at peak frequency

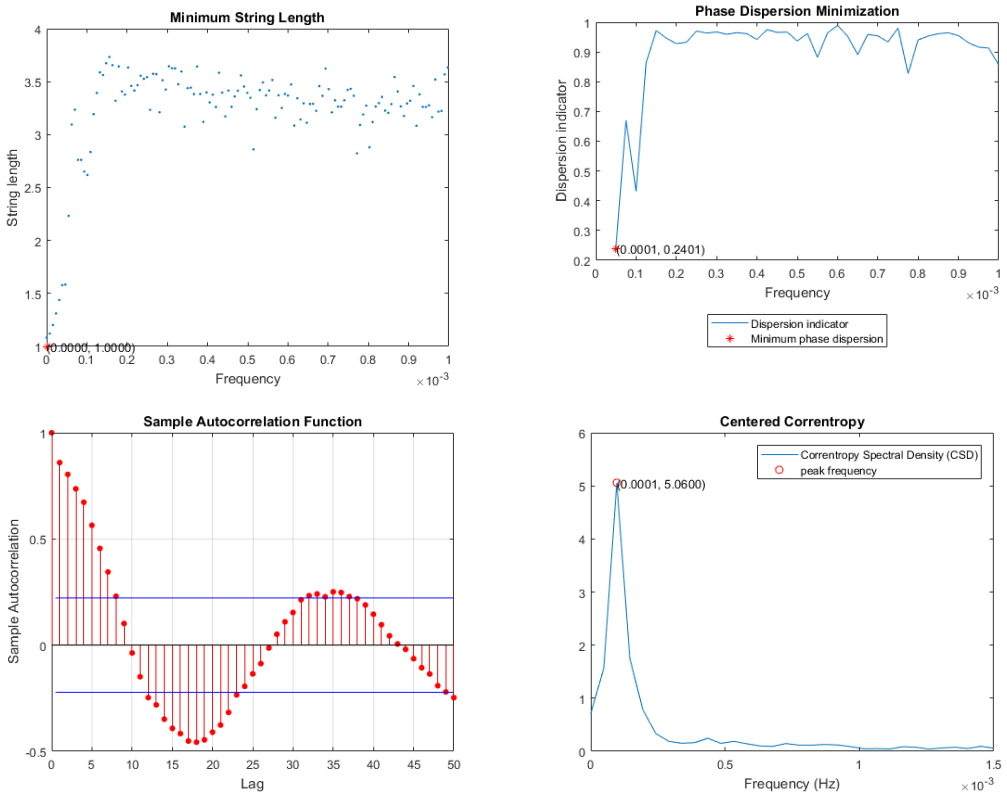

Figure 2.5: Phase-folding methods on asteroid 43 Ariadne's light curve (Top to bottom): minimum string length, phase dispersion minimization, autocorrelation function, centered correntropy

Table 2.4: Rotational Periods of Asteroid 43 Ariadne using light curve

Method	Computed Rotational Period (hrs)
Fast Fourier Transform	—
Classical Periodogram	2.7778
Lomb-Scargle Periodogram	2.8877
Minimum Curve Length	∞
Phase Dispersion Minimization	5.5556
Autocorrelation Function	—
Centered Correntropy	2.8704

Unsurprisingly, the FFT (Fig. 2.4 (top)) has the peak frequency annotated at 0 Hz which is expected for non-uniformly sampled data. This will result in a divide by zero scenario when computing the rotational period. The periodogram analysis performed significantly better with a non-zero peak frequency. The rotation period is calculated to be 2.8877 hrs via Lomb-Scargle periodogram (Table 2.4). This is approximately half of the expected value and is a phenomenon sometimes visible with elongated asteroids. Most asteroids are irregularly shaped so that the projected area of the surface facing the Sun varies as the asteroid rotates [42]. The light curve (almost symmetric) will generally have two minima and two maxima per period. An oblong object rotating about a spin axis (tilted to non-zero angles with respect to both its major and minor body axes) shows an increasing projected area to the observer until it reaches a maximum. Then the projected area decreases to a minimum, followed by another maximum as the object completes a full turn. The time between adjacent maxima is therefore half the rotational period [42]. The half-period is the most promiment period in the data when using any period analysis technique, hence the actual period of rotation is $2T$. Since the asteroid is a resolved space object, we have some *a priori* information on its shape, hence this characteristic is eligible for application. Recomputing the actual rotation periods (with the exception of Phase dispersion minimization) is tabulated in Table 2.5 along with the errors in the computed period values.

Of all the methods, the Lomb-Scargle periodogram presented the smallest percentage error followed by centered correntropy from the expected values at $< 1\%$ *each.* This difference is small enough and almost negligible to consider these methods an accurate approximation for rotational period estimation. The classical periodogram and phase dispersion minimization also had considerably small errors to be accepted as a reasonable estimator.

Table 2.5: Rotational Periods of Asteroid 43 Ariadne using light curve data and their associated errors

Method	Half-Rotational period (hrs)	Rotational Period (hrs)	Error (%)
Classical Periodogram	2.7778	5.5556	3.6
Lomb-Scargle Periodogram	2.8877	5.7754	0.23
Phase Dispersion Minimization	—	5.5556	3.6
Centered Correntropy	2.8704	5.7408	0.37

2.3.3 Procedure to generate synthetic light curves

A generic procedure to generate synthetic light curves of a RSO is depicted in the algorithm below.

Algorithm 7 Synthesize light curve from model of object

procedure LC
    Read STL file of object and extract faces, vertices, and normals
    Perform Delaunay Triangulation
    Set surface properties: color, transparency, and reflectance
    Create light as a point source
    Set observer's location coordinates, $\vec{O}$
    Initialize pole spin axis, $\vec{p}$
    Set background = black
    $n \leftarrow$ desired number of revolutions
    for $i \leftarrow 1, n$ **do**
        Capture object from observer's view and convert frame to indexed image data
        Calculate relative luminance array using RGB for each pixel
        Compute average brightness intensity of all pixels
        Rotate object by an angle increment
    end for
end procedure

2.3.4 Simulation of Asteroid 43 Ariadne

Using the 3D vertex coordinates of 43 Ariadne generated from the Database of Asteroid Models from Inversion Techniques (DAMIT) software suite written by Joseph Dŭrech, and applying Delaunay triangulation gives us the facets on the shape model (Fig. 2.6).

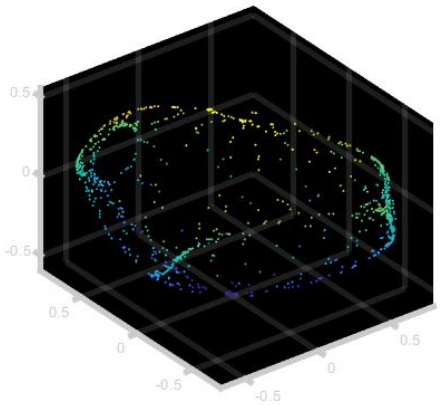

(a) Vertices Point cloud

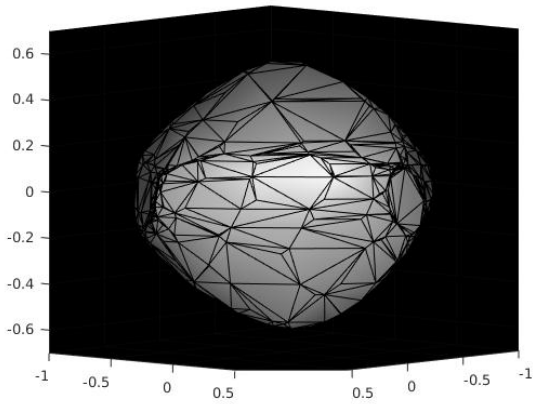

(b) Surface Triangulation

Figure 2.6: Asteroid 43 Ariadne as seen by the observer at 0°

The method, initially developed by the author in [26], is used to generate the synthetic uniformly-sampled light curves and the parameter details are rationalized succeeding this. The surface reflectance properties were set to include ambient, diffuse and specular reflection ($k_a = 0.5,\ k_d = 1,\ k_s = 0.3$ respectively).[1] The motion of the sun with respect to the asteroid is negligible. The lighting conditions are ideal to produce uniform white light at a point source that radiates in all direc-

[1] `http://paulbourke.net/miscellaneous/asteroid/`

tions. The astrocentric coordinates of the Sun at the first observed Julian date are (1.467574, 1.309298, 0.08242228) AU. The light is interpolated linearly across each triangular facet using the vertex normals. Similarly, the observer's location on earth has the astrocentric coordinates of (0.7140329, 0.6399864, 0.0723648) AU and is facing the target. Since this RSO is resolved, we are aware of its ecliptic pole coordinates as $\lambda = -15°,\ \beta = 253°$. Permuting one full rotation of 360° about this spin axis orientation such that the angular speed is defined by the user has the results in Table 2.6. *Since Lomb-Scargle periodogram has consistently proven the most accurate of all the methods*, it is reliable to test this simulation at different angular speeds of rotation.

It can be inferred from Table 2.6 that the percentage errors are all less than 5%, with two outliers at angular speeds of 19 and $20°/s$. This is a fairly reasonable accuracy for the simulation. Notably, most computed half-period values differ from the expected by 0.5 seconds and this is reflected in the error. Although, the relative error begins to increase from angular speed of 1 to $6°/s$, the pattern wobbles consequently. There is no direct correlation between the error and the angular speed of rotation. This may be a ramification of the function's search conditionality. One peculiar phenomenon was observed related to the the initial capture of the object. At time 0, one would expect a brightness intensity close to darkness prior to the shutter collecting images. This does not occur in all instances of running the simulation and could be the result of the timing of how the frames are captured in MATLAB. Using the synthetic light curve created from one full rotation of 360 degrees at a speed of $1°/s$, the various methods are employed to estimate the rotational period. The appropriate light curve (Fig. 2.7) and the plots corresponding to each analysis method (Figs. 2.8 and 2.9) appear below. It should be noted that the light curve (Fig. 2.7) has its initial brightness value of 255 units which equates to a black screen. This is a feature of the simulation that captures a black frame prior to the the 3D model appearing.

Table 2.6: Computed, Expected Half-Rotational Periods and associated errors of Ariadne using the simulation by varying Angular speed of rotation ω

Angular speed of Rotation ($^\circ/s$)	Computed Half-period (s)	Expected Half-Period (s)	Error (%)
1	180.5	180	0.28
2	90.5	90	0.56
3	60.5	60	0.83
4	45.5	45	1.11
5	36.5	36	1.39
6	30.5	30	1.67
7	26	25.71	1.11
8	23	22.5	2.22
9	20.5	20	2.5
10	18.5	18	2.78
11	16.5	16.36	0.83
12	15.5	15	3.33
13	14	13.85	1.11
14	13	12.86	1.11
15	12.5	12	4.17
16	11.5	11.25	2.22
17	11	10.59	3.89
18	10.5	10	5
19	10.86	9.47	14.6
20	9.5	9	5.56

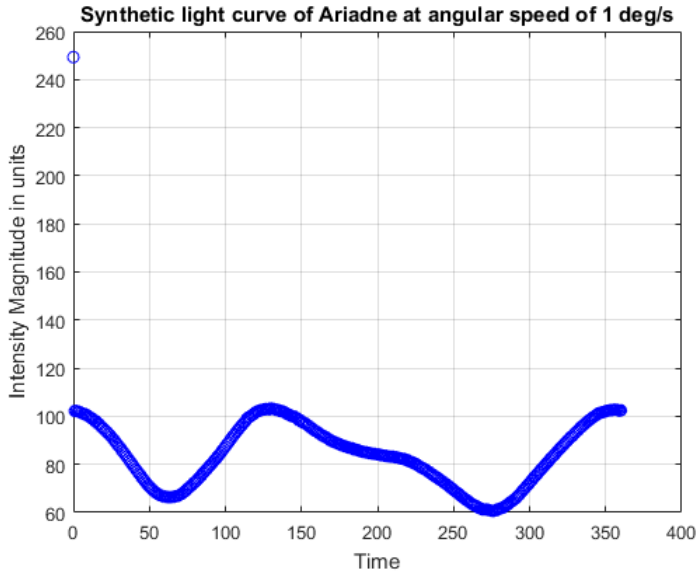

Figure 2.7: Synthetic light curve of Asteroid 43 Ariadne generated using simulation

The expected rotational period is 360 s and Table 2.7 shows the determined values for the various methods and the percentage errors corresponding to each technique. Some of the Fourier methods require the rotational periods to be found by doubling the half-rotational period as seen in the previous case study.

Table 2.7: Rotational Periods of Asteroid 43 Ariadne using simulated light curve and their errors

Method	Half-Rotational period (s)	Actual Rotational period (s)	Error (%)
Fast Fourier Transform	—	—	—
Classical Periodogram	188.7	377.4	4.8
Lomb-Scargle Periodogram	180.5	361	0.28
Minimum String Length	—	360	0
Phase Dispersion Minimization	—	333.33	7.4
Autocorrelation Function	—	—	—
Centered Correntropy	—	353.2	1.9

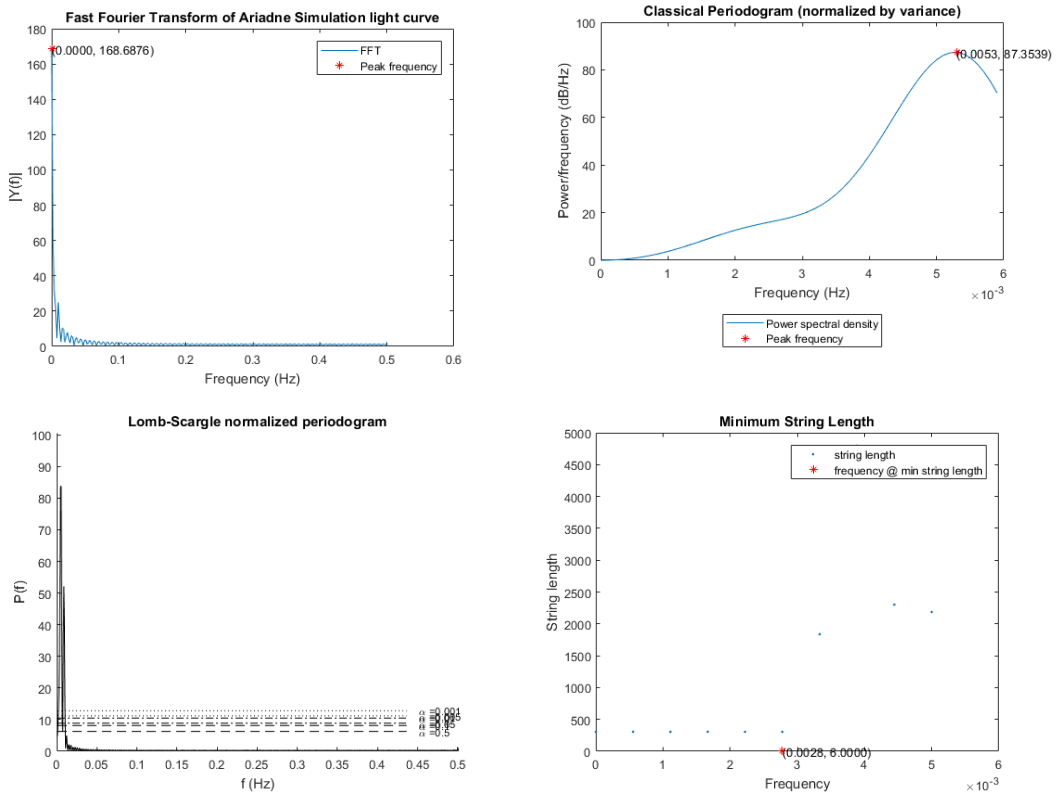

Figure 2.8: Period-finding methods on asteroid 43 Ariadne's synthetic light curve (Top to bottom): fast fourier transform, classical periodogram, Lomb-Scargle periodogram, minimum string length

Compared to the results obtained with the actual light curve in the previous section, some of the methods have shown strange behavior. The minimum string length period managed to calculate the expected period with no error. The Lomb-Scargle, classical periodograms, centered correntropy and phase dispersion minimization accrued numerical values with percentage errors less than 10% with the first being the most accurate. That said, the choice of σ, the kernel size plays an important role in the centered correntropy method and an appropriate kernel size cannot be ascertained if the data shows such large outliers and/or without sufficient a priori knowledge. The

maximum frequency search value must be chosen optimally and to ensure minimum error, the period value of Lomb-Scargle periodogram is a good benchmark for accuracy.

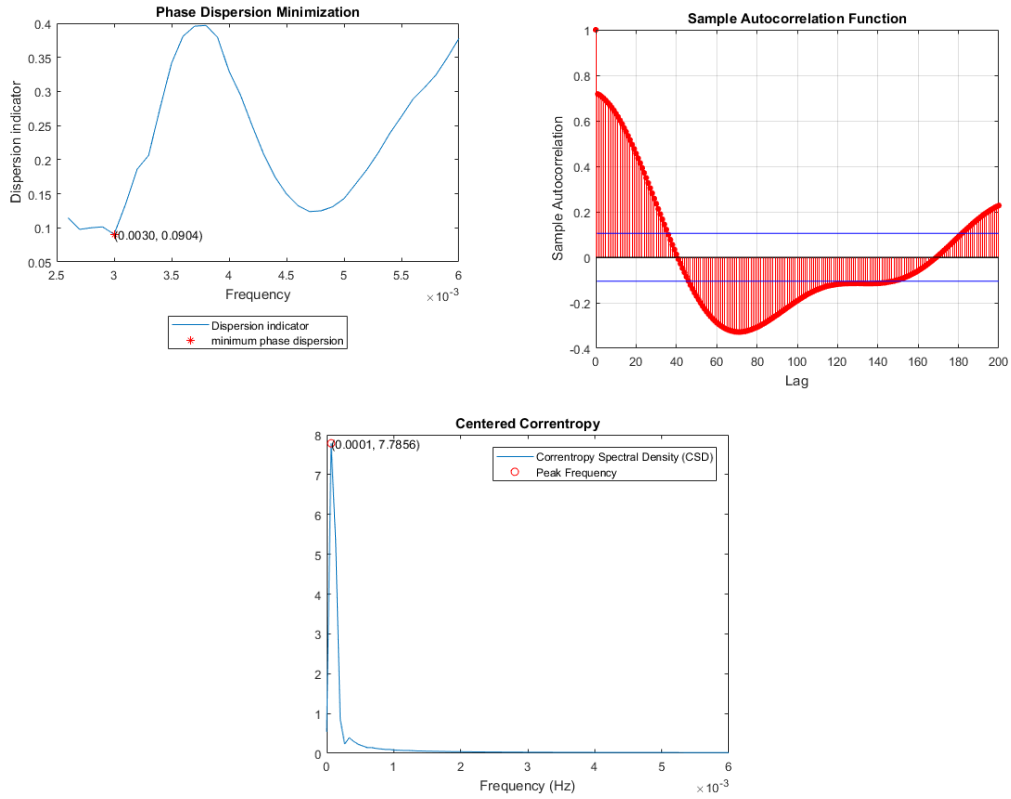

Figure 2.9: Period-finding methods on asteroid 43 Ariadne's synthetic light curve (Top to bottom): phase dispersion minimization, autocorrelation function, centered correntropy

2.3.5 Simulation of LEO artificial objects

Most rockets and payloads give off specular flashes. Their metallic surfaces act as a mirror for the sunlight. The observer can see this reflected sunlight only if the reflecting surface is perpendicular to the bisectrix of the solar phase angle. A portfolio of objects consisting of simple geometric shapes and complex composite objects have been presented in this section. Testing light curves from a wide range of objects

(simulated with the procedure illustrated in an earlier section) will allow us to gauge the performance of period-finding algorithms for artificial debris. The objects (in order) are 1U cubesat, NASA Regolith Advanced Surface Systems Operations Robot (RASSOR) Bucket Drum, Pioneer 9 disks and probe, Pioneer 10 probe, box-wing satellite and a rocket nose cone. The STL files for these objects were gathered from GrabCad[1]. For all tumbling objects, the observer has captured 1 frame per second for 2 full revolutions about its own spin axis, with frame axes limits enforced manually.

2.3.5.1 Cubesat (1U)

CubeSats, in their smallest form, measure about four inches on each side, weigh less than three pounds, and have an approximate volume of one quart. CubeSats are built using these standard dimensions or Units (U) and are typically classified as 1U, 2U, 3U, 6U, or 12U in total size. The total number of cubesats present in space have exponentially increased in the last two decades. Majority of launches were performed by academia, involving experiments for Earth observation and amateur radio. Currently, they fly as auxiliary payloads aboard rockets. For this case study, a 1U cubesat (Fig. 2.10(a)) has been simulated in LEO using model spectral reflectance measurements of CanX-1 (a Canadian CubeSat Nanosatellite program) [54]. In the light curve (Fig. 2.10(b)), we can see repetitive behavior with identical intensities, verifying the simulation process. If the reflecting surfaces are flat (e.g. box shaped satellites), there is no guarantee that the reflection is observed during one full-body rotation.

[1]https://grabcad.com/

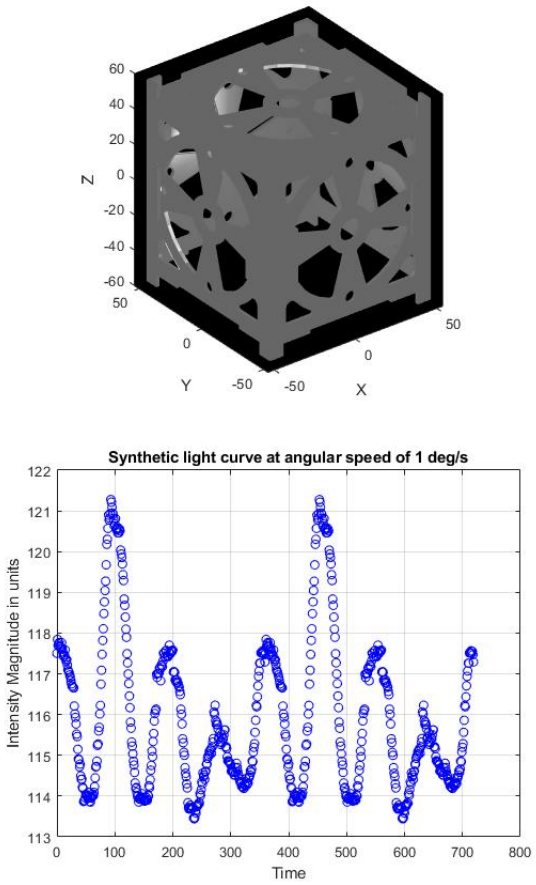

Figure 2.10: Cubesat (1U) (left) and its synthetic light curve (right)

Table 2.8: Rotational Periods of Cubesat using simulated light curve and their errors

Method	Period (sec)	% Error
Fast Fourier Transform	—	—
Lomb-scargle periodogram	359.5*	0.14
Autocorrelation function	—	—
Minimum string length	359.5	0.14
Classical periodogram	370.4	2.88
Phase Dispersion Minimization	357.1	0.79
Centered Correntropy	358	0.56

From Table 2.8, we see at first glance that Lomb-scargle periodogram and minimum string length have the least error [1]. As expected, the FFT and autocorrelation function were not able to execute the algorithm for this light curve.

2.3.5.2 NASA Regolith Advanced Surface Systems Operations Robot (RASSOR) Bucket Drum

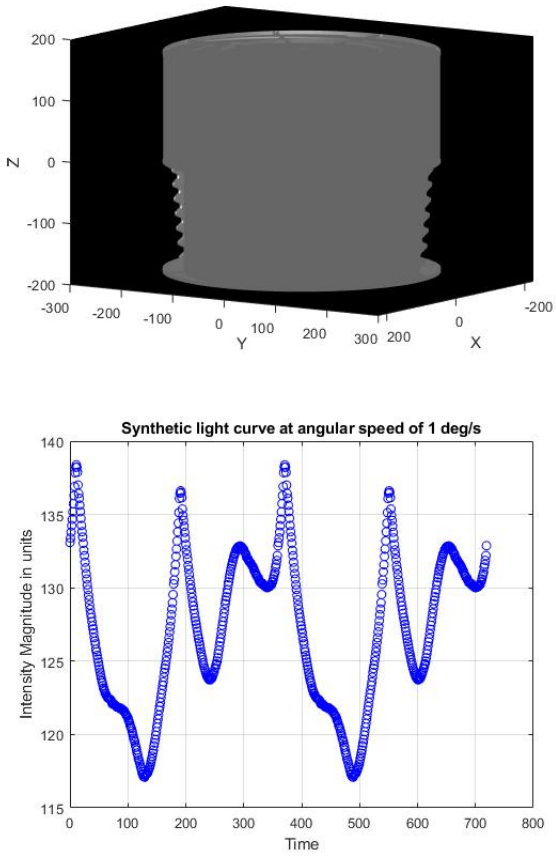

Figure 2.11: NASA RASSOR bucket drum (left) and its synthetic light curve (right)

NASA RASSOR Bucket Drum (Fig. 2.11(a)) is the portion of the robot that captures the regolith and keeps it from falling out. The regolith can then be transported

[1]Period computations with an asterisk (∗) originally resulted a period harmonic

to a designated location where reverse rotation of the drum allows it to fall back out. It is a cylindrical shape with closed top, bottom and sides. The ends of the cylinder are assumed to be reflective. Cylindrical objects have reflecting surfaces in many more directions at any time than objects with flat sides. The light curve of rotating cylindrical objects will give off between zero and two flashes per period, as seen in Fig. 2.11(b).

Table 2.9: Rotational Periods of RASSOR Bucket Drum using simulated light curve and their errors

Method	Period (s)	Error (%)
FFT	—	—
Lomb-scargle periodogram	359.5	0.14
Autocorrelation function	—	—
Minimum string length	359.5	0.14
Classical periodogram	357.1	0.79
Phase Dispersion Minimization	357.1	0.79
Centered Correntropy	358	0.56

From Table 2.9, all methods except FFT and ACF have performed well to within 1% error. Again, the Lomb-scargle periodogram and minimum string length have the highest accuracy.

2.3.5.3 Pioneer 9 Disks

Pioneer 9, launched in 1968, was the fourth in a series of five NASA probes designed to collect data on electromagnetic and plasma properties of interplanetary space from widely separated points in heliocentric orbit over at least six passages of solar activity centers.

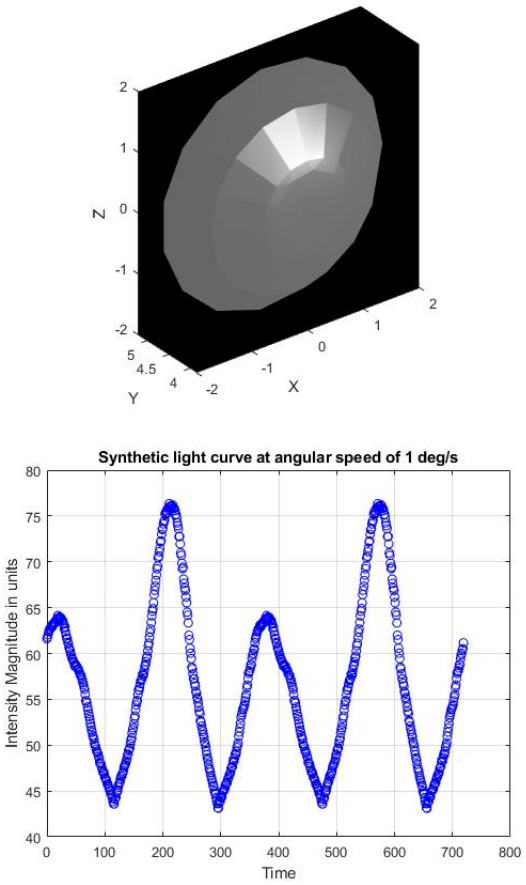

Figure 2.12: Pioneer 9 Disks (left) and its synthetic light curve (right)

Table 2.10: Rotational Periods of Pioneer 9 Disks using simulated light curve and their errors

Method	Period (s)	Error (%)
FFT	—	—
Lomb-scargle periodogram	359.5*	0.14
Autocorrelation function	—	—
Minimum curve length	359.5	0.14
Classical periodogram	363.6*	1.01
Phase Dispersion Minimization	357.1	0.79
Centered Correntropy	358	0.56

The curved disk (Fig. 2.12(a)) has produced a regular, symmetric sinusoidal shape (Fig. 2.12(b)). The computed periods for the periodograms are the half-periods from the initial iteration. After closer observation and knowing the shape of the disk, doubling the values has mirrored the performance of the bucket drum in errors (Table 2.10) with the exception of classical periodogram. The error has increased by a minuscule amount to 1.01%, but all techniques are within acceptable range. Lomb-Scargle and minimum string length resulted in the least error to expected period.

2.3.5.4 Pioneer 9 Probe

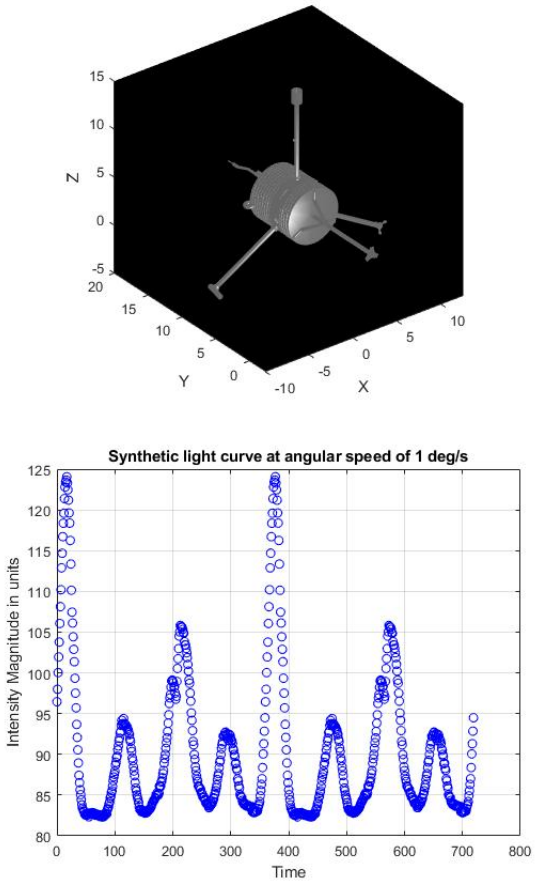

Figure 2.13: Pioneer 9 probe (left) and its synthetic light curve (right)

Table 2.11: Rotational Periods of Pioneer 9 Probe using simulated light curve and their errors

Method	Period (s)	Error (%)
FFT	—	—
Lomb-scargle periodogram	359.5*	0.14
Autocorrelation function	—	—
Minimum string length	359.5	0.14
Classical periodogram	377.4*	4.82
Phase Dispersion Minimization	357.1	0.79
Centered Correntropy	358	0.56

The raw results tabulated in Table 2.11 show evidence of identifying harmonics of a period for Lomb-Scargle periodogram and classical periodogram. In the former case, multiplying the value by 4 results in a period of 359.5 seconds, equating to a 0.14% error. On the other hand, classical periodogram employs the half-period characteristic producing a less than 5% error after doubling the period. With some post-processing, Lomb-scargle and minimum string length have shown highest accuracy in this test case as well.

2.3.5.5 Pioneer 10 Probe

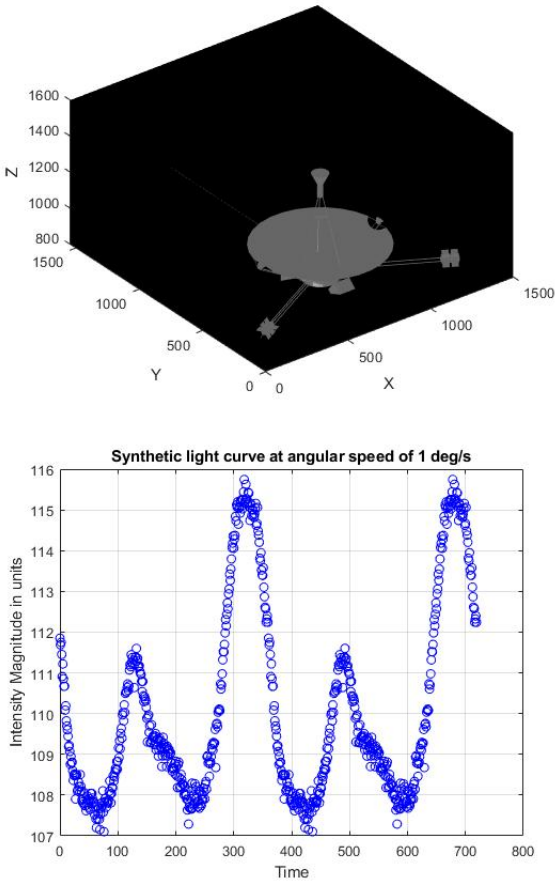

Figure 2.14: Pioneer 10 probe (left) and its synthetic light curve (right)

Table 2.12: Rotational Periods of Pioneer 10 Probe using simulated light curve and their errors

Method	Period (s)	Error (%)
FFT	—	—
Lomb-scargle periodogram	359.5*	0.14
Autocorrelation function	—	—
Minimum string length	359.5	0.14
Classical periodogram	363.6*	1.01
Phase Dispersion Minimization	357.1	0.79
Centered Correntropy	358	0.56

It is interesting to note that the computed period from Table 2.12 almost reflects identically to that of Pioneer 9 probe with the exception of the classical periodogram. This is considering the fact that the objects differ in shape with the central body of a dish antenna for Pioneer 10 probe instead of a cylinder. This is reflected in the number of peaks in the light curve (Fig. 2.14(b)) correspoding to features of the object.

2.3.5.6 Box-wing interplanetary satellite

Spinning satellites usually have booms, solar panels or other structures that cause asymmetries in the cylindrical body and hence regular flashes can occur, as seen in Fig. 2.15(b). After studying four inactive box-wing geosynchronous satellites' light curves, it was observed that their brightness varies in a periodic fashion [55]. This stemmed from the reasoning that reflected sunlight was modulated due to satellite spin. The spin period variation was negligible in hourly timescale, but significant and possible cyclically over monthly and yearly timescales, as expected. An external disturbance torque (solar radiation pressure) acting on the large-area solar panels produced sufficient angular accelerations [55]. In fact, solar radiation torques have a long-term effect on the evolution of spin of any spacecraft (i.e. Earth orbiting

spacecraft, deep space probes, solar sails) [56]. Our case study is over a shorter timescale, hence these variations are not observed, although with real data it is highly probable.

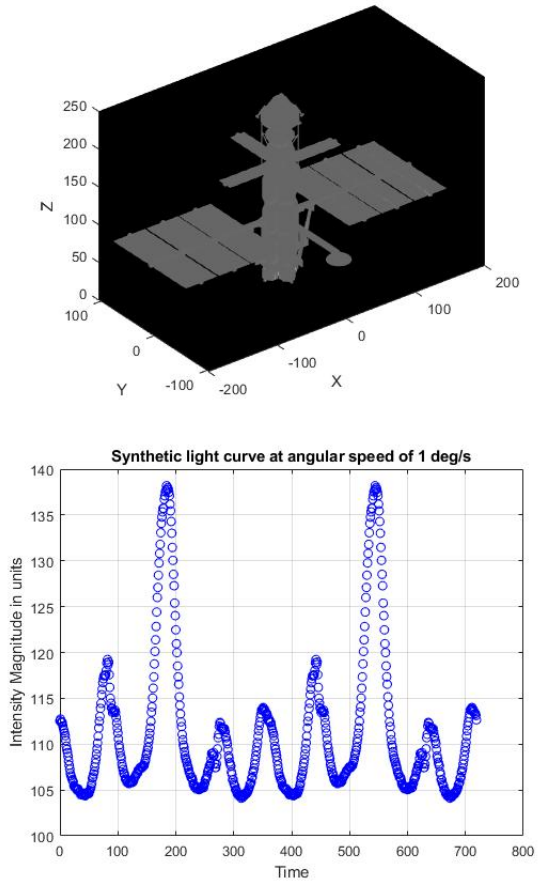

Figure 2.15: Box-wing satellite (left) and its synthetic light curve (right)

Table 2.13: Rotational Periods of Box-wing interplanetary satellite using simulated light curve and their errors

Method	Period (s)	Error (%)
FFT	—	—
Lomb-scargle periodogram	359.5*	0.14
Autocorrelation function	—	—
Minimum string length	359.5	0.14
Classical periodogram	333.33	7.41
Phase Dispersion Minimization	357.1	0.79
Centered Correntropy	358	0.56

Due to temporal aliasing, the Lomb-Sargle periodogram exhibits a period harmonic in Table 2.13.

2.3.5.7 Rocket Nose Cone

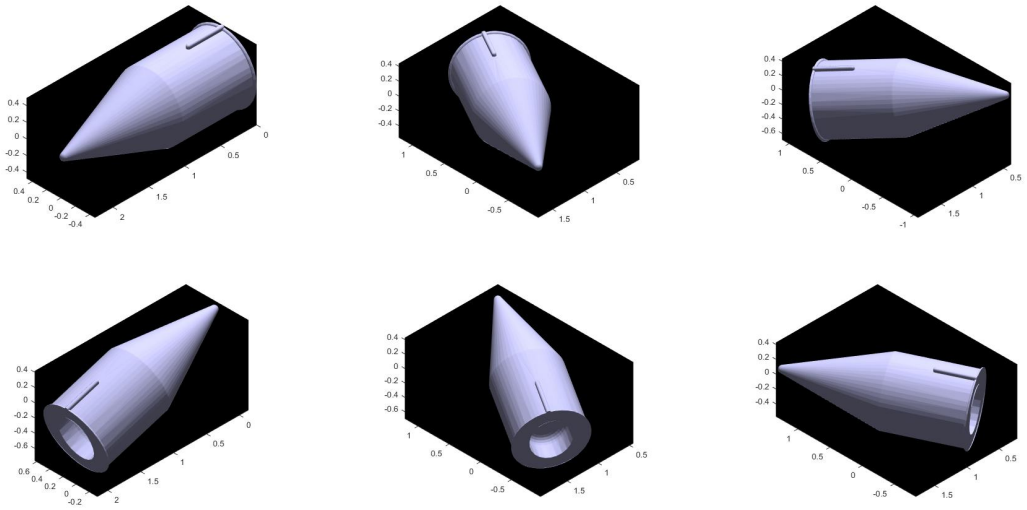

Figure 2.16: Different geometries of Rocket nose cone at specified angles of rotation as seen by the observer.
1st Row: (Left to Right) 60°, 120°, 180°, 2nd Row: (Left to Right) 240°, 300°, 360°

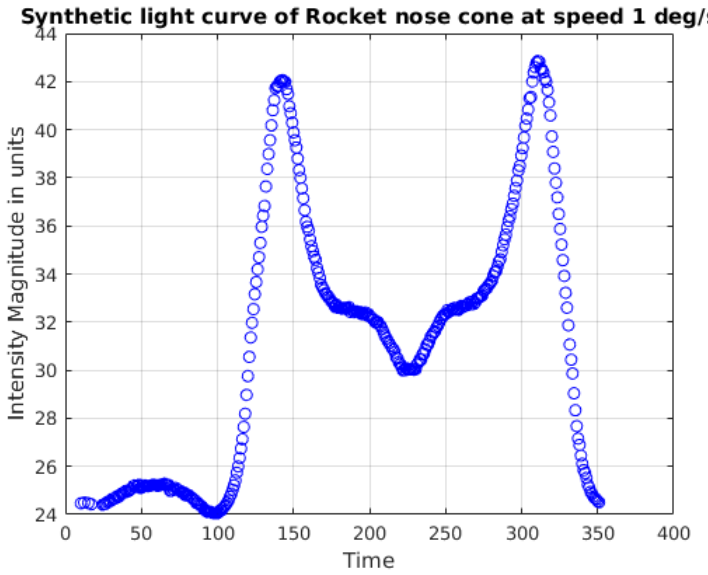

Figure 2.17: Synthetic light curve of Rocket nose cone generated using simulation

Using the CAD model of a rocket nose cone (Fig. 2.16)[1], the material surface properties were set to include ambient, diffuse and specular reflection ($k_a = 0.8,\ k_d = 0.1,\ k_s = 1$ respectively). Rocket nose cones are primarily made of plastic, fiberglass and hard wood [2], hence the choices of reflective properties. The lighting conditions are ideal to produce uniform white light at a point source that radiates as a headlight. The position of the object with respect to the observer's location on earth has the coordinates of $(7.140329,\ 6.399864,\ 1.33692) \times 10^{-}5$ AU, which is approximately 2000 km altitude. The spin axis orientation is user-defined as $\lambda = -20°,\ \beta = 90°$. Tumbling effects are ignored in this scenario. Performing a 360° rotation about its own spin axis has produced the light curve (Fig. 2.17).

[1]C. Kaufman, `https://grabcad.com/caleb.kaufman-3`
[2]T. Beach, `http://www.unm.edu/~tbeach/IT145/week05/parts.html`

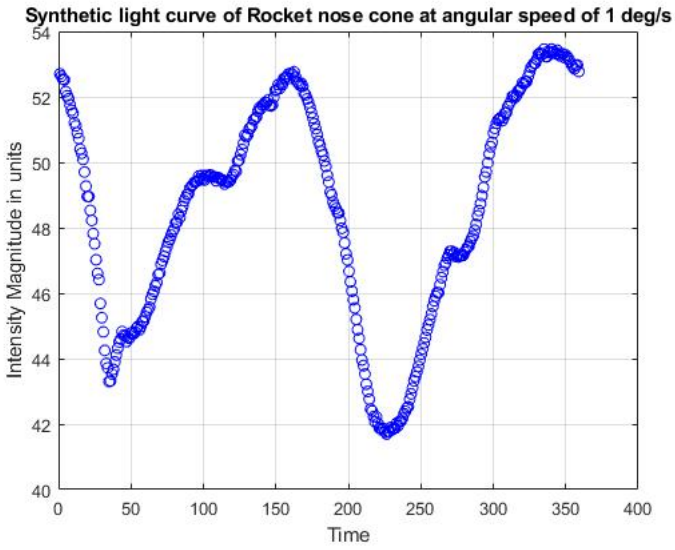

Figure 2.18: Synthetic light curve of Rocket nose cone generated using simulation with axes limits enforced manually

It is observed that the first generated light curve (Fig. 2.17) is not symmetric or periodic, unlike the asteroid. Another characteristic of the software that affects the brightness magnitude is the image's window framing as the object is rotating. This causes the light curve to vary, but can be kept consistent by manually verifying axes limits (Fig. 2.18). Applying the period estimation methods to this light curve results in the computed values (Table 2.14).

Table 2.14: Rotational Periods of Rocket nose cone using simulated light curve and their errors

Method	Rotational period (s)	Error (%)
Fast Fourier Transform	—	—
Classical Periodogram	370.4*	2.88
Lomb-Scargle Periodogram	358*	0.56
Minimum String Length	—	—
Phase Dispersion Minimization	363.6*	1.01
Autocorrelation Function	—	—
Centered Correntropy	356	1.11

In this test case, we can observe that the only reasonable estimates resulted from classical periodogram, Lomb-Scargle periodogram, phase dispersion minimization, and centered correntropy. The technique resulting in the least error is Lomb-Scargle periodogram.

Of all the simulation test cases discussed so far in the paper and henceforth, some techniques require user influence to perfect the algorithm as mentioned previously. They include minimum string length, classical periodogram, autocorrelation function, phase dispersion minimization and centered correntropy. The parameters to optimize are frequency search range, frequency search interval, number of lags, number of bins and maximum frequency respectively. Some methods' complexity increases as they employ multiple parameters. In order to ensure the best values, the Lomb-Scargle periodogram is a reasonable reference to center about, for the frequency search range. Using this as an initial guess and correcting it through iterations will reach the closest value possible to the expected period. One of the more peculiar variables is the maximum frequency (f_{max}) for the centered correntropy. In a way, it has an inverse proportionality to the dominant frequency (i.e. doubling f_{max} will halve the rotational frequency). Therefore, these methods used in conjunction with the Lomb-Scargle ameliorates the precision.

2.3.6 Varying the sampling frequency

Using the Box-Wing satellite for a 720-degree rotation where the object is tumbling at 1°/sec, varying the observer's sampling frequency in frames per second (fps) is tabulated (Table 2.15) illustrating the rotation periods (in seconds). For an expected period of 360 seconds, we see that FFT cannot handle the sampling. Lomb-Scargle periodogram determines a period harmonic as the dominant frequency. Classical periodogram and phase dispersion minimization are not affected by varying sampling frequency. We do see that minimum string length and centered correntropy

are dependent on the quality of the light curve and show a decline in accuracy with lower quality light curves as a consequence of fewer observations.

Table 2.15: Effect of varying the sampling frequency (1, 0.5, 0.33, 0.2 and 0.1 frames/second) on rotational period (seconds)

Method	1 fps	0.5 fps	0.33 fps	0.2 fps	0.1 fps
Fast Fourier Transform	—	—	—	—	—
Classical Periodogram	333.3	333.3	333.3	333.3	333.3
Lomb-Scargle Periodogram	89.88	92.64	92.52	92.26	91.61
Minimum String Length	359.5	359	358.5	357.5	355
Phase Dispersion Minimization	357.14	357.14	357.14	357.14	357.14
Centered Correntropy	358	356	354	350	340

2.3.7 Varying the time-series duration

Using the box-wing satellite where the object is tumbling at 1°/sec and sampling frequency is 1 fps, the length of time-series duration is varied by using fractions of a full-body rotation. The periods derived from this is tabulated (Table 2.16) in seconds. Unlike the previous experiment, the length of the time-series for data collection has no direct correlation to the effectiveness of the period-finding algorithm. However, periodograms and correntropy are able to generate an acceptable period regardless of the duration of the light curve, at the bare minimum.

2.3.8 Stellar Transit Light curve

The Kilodegree Extremely Little Telescope (KELT) project is a survey for planetary transits of bright stars. It consists of a small-aperture, wide-field automated telescope located at Winer Observatory near Sonoita, Arizona as indicated by [57]. Authors in [58] agree that the Beehive Cluster or Praesepe is an open star cluster

Table 2.16: Effect of varying the time-series duration on rotational period (seconds)

Method	720° rotation	540° rotation	360° rotation	180° rotation	90° rotation
Fast Fourier Transform	—	—	—	—	—
Classical Periodogram	333.33	116.28	100	100	100
Lomb-Scargle Periodogram	89.88	89.83	95.73	89.5	89
Minimum String Length	359.5	∞	359	∞	∞
Phase Dispersion Minimization	357.14	357.14	277.78	181.82	∞
Centered Correntropy	358	357.33	356	352	357

in the constellation Cancer. Praesepe is a bright, large cluster with an apparent magnitude of 3.7. It lies at a distance of 577 light years from Earth [1].

From the NASA Exoplanet Archive, the transit survey of object HAT-138-0001727 collected from KELT Praesepe over a duration of 100 heliocentric Julian days (HJD) was utilized to perform period estimation using some of the methods that proved favorable with Asteroid 43 Ariadne.

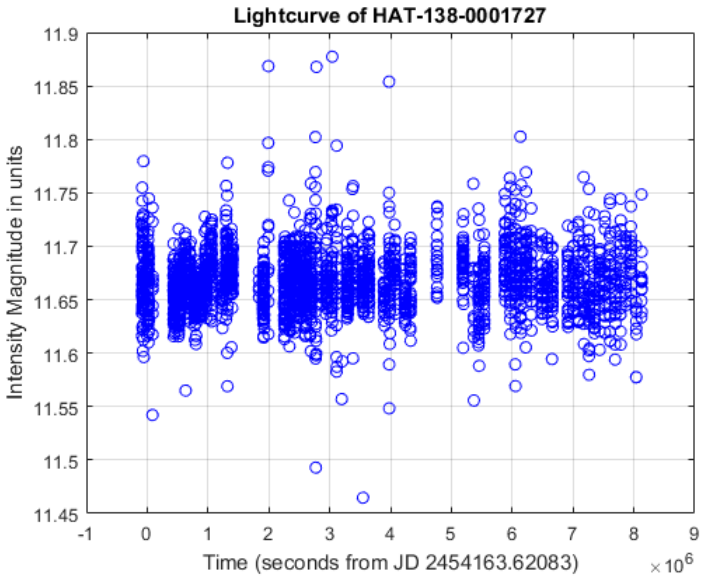

Figure 2.19: Transit Survey of HAT-138-0001727 from NASA Exoplanet Archive

This transit light curve (Fig. 2.19) has a really long duration compared to the earlier test cases and the number of observation points has multiplied manifold. The following results can give some explanation in terms of capabilities to handle large datasets.

[1] https://www.messier-objects.com/messier-44-beehive-cluster/

Table 2.17: Rotational Periods of stellar object HAT-138-0001727 using transit survey

Method	Computed Rotational Period (days)
Lomb-Scargle Periodogram	4.4232
Minimum Curve Length	∞
Phase Dispersion Minimization	4.0188
Centered Correntropy	1378.6

Comparing values from Table 2.17 to the referenced value of 4.41341887 days from the NASA Exoplanet archive, *we can conclude that the Lomb-Scargle periodogram is the most reliable when estimating rotational periods of varying dataset sizes, as well as in both uniformly and non-unifomly sampled scenarios. It is rigorous in exhausting all possible frequencies in the range search without requiring any user input, which is the deficiency of the phase dispersion minimization method. This method can handle large gaps in the time series too.*

2.4 Conclusion and Future Work

Of all the time series analysis methods, the periodogram methods and Phase Dispersion Minimization worked correctly for all test cases and the former resulting in the least percentage error when comparing with the expected values, except for the simulated rocket nose cone. The Lomb-Scargle periodogram is versatile in estimating period of objects that are sampled both uniformly and non-uniformly (which is more realistic when looking at ground-based observations of space objects). Certain methods like the FFT only handle evenly sampled data since it requires a sampling frequency. The phase-folding methods have a slight disadvantage in that there are additional parameters such as lags and number of bins that can vary the final output greatly. Performing the operation also requires the user to know before-hand, a viable search

range of frequencies as well as an interval with which to search with. These two values must be accurate for the method to work at all. The Lomb-scargle periodogram has a robustness to it to process large sets of observational data with less interference from the user. This was proven with the transit survey of the object HAT-138-0001727. It showed an accuracy of 0.23% error for Asteroid 43 Ariadne which is a very good estimator of period. The only downside was with the simulation and synthetic light curves at angular speeds of 19 and 20 degrees per second as it generated errors greater than 5% but was still quite reasonable (based on results from published literature that deemed this criterion acceptable). This was mimicked in the rocket nose cone rotating at an angular speed of 1 deg/sec. Although methods like minimum string length and centered correntropy performed well for simulation of LEO objects, they have both hits and misses with other RSOs and its inconsistency leads to little reliability. The phase dispersion minimization algorithm is consistent with any number of bins less than 100 and the number of lags are irrelevant of the autocorrelation function's predicted period as long as it doesn't exceed a threshold. Varying angular speeds of rotation or the number of 360-degree rotations does not alter the location of peaks in the periodograms significantly and this validates the consistency of results and re-assures that the window of data collection is irrelevant to determine the period of rotation. These values are dependent on the previously stated test case parameters and may differ for other spin axis orientations. Since there is little to no access to available "truth" values with which to compare these results, the paper invites observations and analyses from other researchers to validate this technique and verify the sidereal rotation periods determined through simulation means. We can conclude that the Lomb-Scargle periodogram is the most reliable for test cases at varying distances from the observer on Earth including LEO (cubesat, RASSOR bucket drum, disks, Pioneer probes, box-wing satellite and rocket nose cone), deep space (asteroid Ariadne) and

exo-Solar objects (Stellar transit survey). Ensemble methods (using Lomb-scargle to predict search parameters) show improvement over single algorithms, however it does not exceed the consistent performance of the Lomb-scargle periodogram on its own. Optimizing the periodogram to identify period harmonics would enhance this process.

Spent rocket bodies and defunct satellites are major sources of orbital debris in low-Earth orbits that pose higher threats directly to humans through collisions with Earth or each other causing major communication failure. Future work includes testing with real data of operational and inactive satellites. A generic method may be developed for unknown targets that exhibit periodic changes in brightness and give forth to estimating its shape and motion solely based on photometric observations and astrometric data using ground-based data collection methods.

It is also seen that for the cases when the methods yielded agreeable results, the errors are bounded to 10% which is a reasonable estimator for period and the proximity to expected value increases for methods where the observed data is solely sufficient to estimate the period.

Chapter 3

Computing surface brightness integrals of RSOs

3.1 Introduction

The number of RSOs includes both artificial and natural bodies such as satellites, rocket bodies, and asteroids. Defunct satellites are major causes of concern due to potential collisions [59]. Breakups of Earth-orbiting bodies result in an uncatalogued population thereby creating uncertainties in the resulting environment for spacecraft [60]. An accurate understanding of existing objects' orbit and propagation can help in planning collision avoidance maneuvers. Since the shape, and inertia of the object influences the orbit, especially in LEO, methods to calculate these from observed data (Light curve) are important. The shape is emphasized as it allows for the inference of size, mass and possibly operational status [61]. Using photometric light curves for shape estimation is well-known for asteroids [9, 10, 62]. An axisymmetric cellinoid model was developed as an extension of the ellipsoid shape which consists of eight octants from eight ellipsoids such that adjacent octants share semi-axes [3]. Studies that use LCI for satellites on the other hand have required *a priori* information such as known attitude states and used cube-shaped objects [61]. Investigation of artificial space objects such as rocket bodies and satellites, both active and defunct, in general require a more complex polyhedron to model and thus estimate its shape.

Various methods compute the light curves of irregularly shaped bodies at arbitrary viewing angles and illumination geometries by integrating brightness over the surface. A common method employed is to tessellate the surface, i.e., to represent it as a polyhedral approximation, usually with triangular facets of similar size (triangulation)

[63]. Ref. [64] applies this to estimate the brightness variation of COMS-1 satellite, using a rendering method of summing the total brightness at each simulated position. The brightness is calculated using Hedjuk's equations induced from Pogson's equation [65, 66]. Specifically, the phase function equation for calculating the brightness was developed for fragmentation debris [67], which is defined in terms of the solar phase angle. Algorithms have been proposed to incorporate radial basis functions (RBF) over spherical surfaces using arbitrarily scattered nodes and Gaussian basis functions to reduce the order of operations [68, 69].

Another approach to compute the brightness integrals is to use quadrature schemes such as Gauss, Chebyshev or Lebedev to improve computation [63], instead of triangulation. Quadratures have their merits of being stable, accurate, and minimally computationally expensive in the field of physical optics where the surface integrals are multi-dimensional and highly oscillatory [70]. The choice and distribution of nodes, uniformity of corresponding weights and the computational complexity is what sets each quadrature scheme apart from the other. Increased performance, in terms of accuracy and operation time, for computing surface brightness integrals of axisymmetric bodies is witnessed in the usage of Lebedev quadrature. Specifically, Lebedev quadrature computes the surface integral over a unit sphere making it a worthwhile extension to model naturally spherical/ellipsoidal objects (i.e. asteroids [63]).

Our main contribution includes utilizing Lebedev quadrature scheme for artificial axisymmetric space objects such as cone, cylinder, upper-stage rocket bodies, torus and a unique peanut-shaped asteroid. Typically, man-made objects are not simple to model for computing the brightness surface integrals, due to the presence of sharp edges, and flat reflective surfaces. In this paper, we have shown the use of this quadrature scheme and results are presented for the above-mentioned surfaces as well as composite bodies utilizing a superposition of geometric shapes. Further, the total

brightness integral of a space object is simplified such that the curvature function is reduced from a double to a single integral and the derivation is included later in the paper.

The following sections will provide a theoretical background to surface integrals and quadrature schemes. Application of the formulated surface approximation to axisymmetric test cases is shown in the results through means of simulation. Finally, a comparison of the techniques i.e. tessellation, and quadrature is provided.

3.2 Surface Brightness Integrals

Computing the total brightness of a convex surface as detailed in [63] adapted for irregularly shaped bodies, such as asteroids, is outlined briefly below. An object illuminated by a source (Sun) and the observer viewing on Earth is in a body-fixed coordinate system to the object. The direction unit vectors to the source and observer from the object are $\boldsymbol{\omega}$ and $\boldsymbol{\omega_0}$ respectively. All angles are elements in the unit sphere, S^2. The unit normal vector of a facet, as depicted in Figure 3.1 (Modified image from [4]), is defined as $\boldsymbol{\eta}$ (specifically $\boldsymbol{\eta}(\theta, \psi)$ where θ is measured from the pole - see Figure 3.1b).

$$\eta_1 = \sin\theta\cos\psi \tag{3.1}$$

$$\eta_2 = \sin\theta\sin\psi \tag{3.2}$$

$$\eta_3 = \cos\theta \tag{3.3}$$

The visible, illuminated section of the surface is given by $\boldsymbol{A}$. The integrated total brightness of the target object (made up of a finite number of facets) as seen by the observer at a given time is

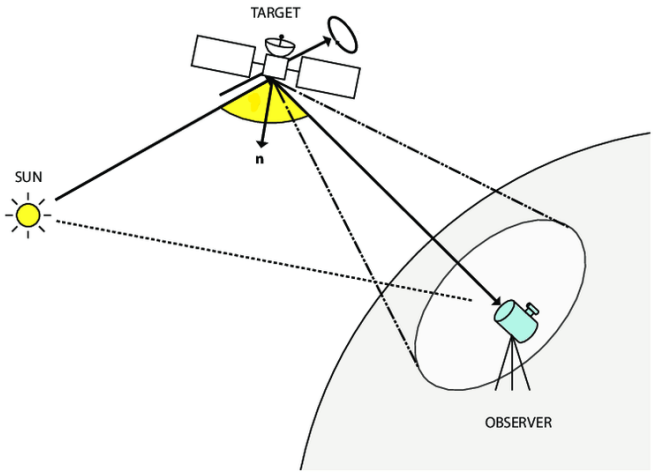

(a) Sun-Object-Observer geometry

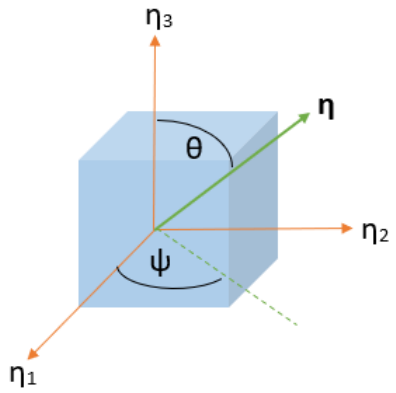

(b) Object's normal direction vector and astrometric angles

Figure 3.1: Simplified geometry involved in light curve acquisition

$$L(\boldsymbol{\omega_0}, \boldsymbol{\omega}) = \int_{\boldsymbol{A}} S(\mu, \mu_0, \alpha) G(\theta, \psi) \sin\theta d\theta d\psi \tag{3.4}$$

and the scattering function $S(\mu, \mu_0, \alpha)$ is dependent on the viewing geometry where

$$\begin{aligned} \mu &= \boldsymbol{\omega} \cdot \boldsymbol{\eta} \\ \mu_0 &= \boldsymbol{\omega_0} \cdot \boldsymbol{\eta} \\ \cos\alpha &= \boldsymbol{\omega_0} \cdot \boldsymbol{\omega} \end{aligned}$$

The scattering function or bidirectional reflectance distribution function (BRDF) uses the area of the facet and α is the solar phase angle [61]. The BRDF model describes light reflection off a surface which comprises the shape's reflectance properties. There are different models to describe the scattering function (i.e. Hapke model) and a simplified model [71] is depicted as

$$S(\mu, \mu_0, \alpha) = f(\alpha)\left(\frac{\mu\mu_0}{\mu + \mu_0} + C\mu\mu_0\right)$$

where $f(\alpha)$ is the phase function and C is a relative weighting factor. The illuminated surface, $\boldsymbol{A}$, encompasses points on the surface where $\mu, \mu_0 \geq 0$. The surface curvature function $G(\theta, \psi) \geq 0$ is denoted by $G(\theta, \psi) = \dfrac{J(\theta, \psi)}{\sin\theta}$ where $J = |\mathbf{J}|$ is the norm of the Jacobian vector $\mathbf{J}(\theta, \psi) = \dfrac{\partial \mathbf{x}}{\partial \theta} \times \dfrac{\partial \mathbf{x}}{\partial \psi}$ and $\mathbf{x}(\theta, \psi)$ gives the surface as a function of the surface normal direction.

To numerically compute the integrated total brightness (equation 3.4), generally, there is a tessellation of S^2 into N almost equal-sized facets approximating the surface as a polyhedron [63]. The area of each facet on the surface is solved for in the inverse problem, which in the LCI procedure [72] leads to shape reconstruction using the Minkowski procedure.

A more analytical approach is to use quadratures instead of geometric tessellation. The objective of quadrature methods is to effectively choose the evaluation points of the integrand function and their corresponding weights [63]. This is usually done on a basis where the form of the function is assumed. There are multiple types of quadrature schemes on a sphere among whom, the Gauss, Chebyshev, and Lebedev schemes will be discussed further.

3.3 Quadrature Schemes

In various applications, the need arises for the calculation of integrals over spherical surfaces in R^3. An integral over the unit sphere S^2 is

$$I[f] = \int_{S^2} f(x) d\Omega = \int_0^{2\pi} \int_0^{\pi} f(\phi, \theta) \sin\phi d\phi d\theta \tag{3.5}$$

where $f : S^2 \to R$. Many times, the actual form of f is complex or unknown, so it is essential to determine an approximation to the integral. A commonly used technique to arrive at such approximations is by use of a quadrature Q, where the integral is approximated by a weighted sum over a finite collection of points. A wide variety of quadratures can be derived under the assumption of fixed weights, such as Chebyshev quadratures. On the other hand Gauss quadratures requires one to determine both weights and nodes [73].

3.3.1 Gauss quadrature

The formulation of (3.5) is an integral over the unit sphere as a product of two one-dimensional integrals over θ and ϕ. As a result, we can use quadrature rules for one-dimensional integrals repeatedly to arrive at

$$Q[f] = \sum_{i=0}^{N-1} \sum_{j=0}^{M-1} w_{ij} f(\theta_i, \phi_j) \tag{3.6}$$

The weights w_{ij} are still to be determined by the choice of two one-dimensional quadrature rules. The generation of the nodes and weights, up to very high order, can be done quickly. The distribution of the nodes in the Gaussian product is clustered around the poles [73]. This, in turn, causes the grid distance between points close to the poles to shrink significantly. Another aspect is the computational time and complications in inverse problems [63]. There is a potential reduction in the number of points, as compared to tessellation, and it's not enough for the computation.

3.3.2 Chebyshev quadrature

Another approach to deriving quadratures on the sphere starts from the assumption that the weights of all the N integration nodes are equal. Quadratures of this type will minimise a probability error if the function values are subject to normally distributed errors, which could be the case if the integrand can only be empirically sampled [74]. As one wants to correctly integrate the constant function $f \approx 1$, this implies that the weights must satisfy

$$w_i = \frac{4\pi}{N}, \quad i = 0, \ldots, N-1 \tag{3.7}$$

The remaining question now is how the nodes should be scattered along the sphere for an optimal quadrature schemes. As the weights are equal for all nodes (as seen in Fig. 3.2), this suggests the seemingly trivial answer that the nodes should be uniformly spread out over the sphere. The location of the zeros are approximately the same for both Gauss and Chebyshev in Fig. 3.2, although subsequently the $5th$ order polynomials have differing peaks and troughs due to their weights. A crucial caveat

soon emerges, to determine the context of uniform distribution and the method of calculating these points.

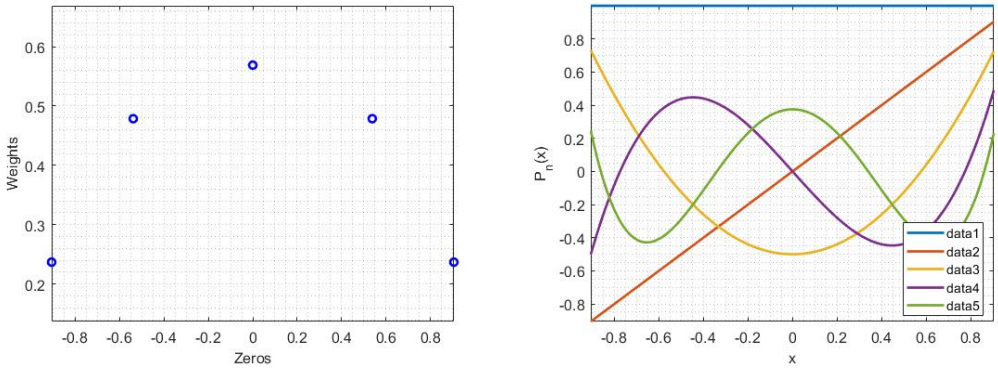

(a) Weights vs. zeros for 5th order polynomial (b) Polynomial P(x) using zeros for orders 1 to 5

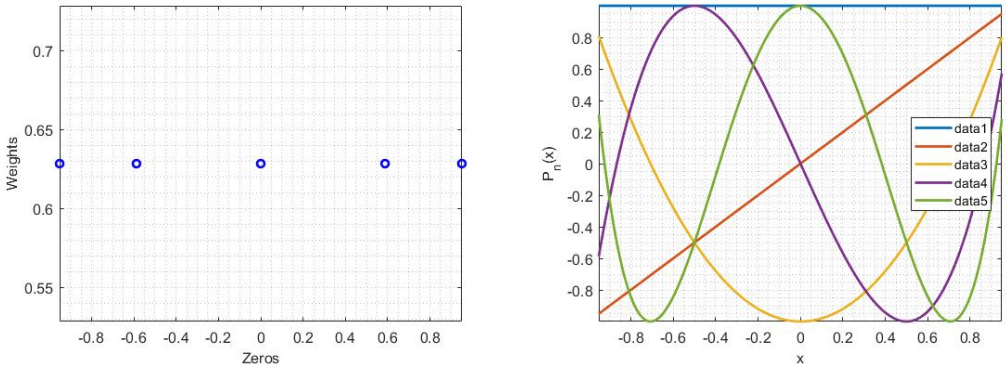

(c) Weights vs. zeros for 5th order polynomial (d) Polynomial P(x) using zeros for orders 1 to 5

Figure 3.2: Roots of a 5th order polynomial using Gauss (Top) and Chebyshev (Bottom) Quadrature

3.3.2.1 Uniform distribution of points on a sphere

If we impose the standard requirement that a quadrature is exact for all spherical harmonics up until order p in the case of equal weights we arrive at the spherical designs. A set of N points $\mathbf{x_i}$ is called a spherical t-design if

$$\int_{\mathrm{S}^2} f(\mathbf{x})\mathrm{d}\Omega = \frac{4\pi}{N}\sum_{i=0}^{N-1} f\left(\mathbf{x}_i\right), \quad \forall f \in \Pi^t \tag{3.8}$$

One normally desires to find spherical designs with a minimal amount of nodes. The efficiency of the spherical designs puts these quadratures on par with the Gaussian quadrature.

3.3.2.2 Random distribution of points on a sphere

Another approach to Chebyshev quadratures is to use a Monte Carlo scheme where instead of a regular grid we use a randomly generated grid yielding a non-deterministic quadrature scheme. This quadrature can be applied to a more general class of integrals over a multidimensional volume V i.e. $J[f] = \int_V f(\mathbf{x})\mathrm{d}\Omega$

It is argued that Monte Carlo integration becomes increasingly competitive for higher-dimensional integrals as it does not suffer from the curse of dimensionality [75]. Under the assumption of a roughly constant sample variance we see that a Monte Carlo quadrature has exactly the same form as spherical designs if the integration is taken over S^2 [73].

3.3.3 Lebedev quadrature

Lebedev quadrature approximates the surface integral over a unit sphere. The mesh grid has octahedral rotation and inversion symmetry. The number and position of the grid points along with corresponding integration weights are computed by evaluating the exact integration of function (or spherical harmonics) up to a reasonable order. The surface integral is approximated as

$$Q[f] = 4\pi\sum_{i=0}^{N-1} w_i f(\theta_i, \phi_i) \tag{3.9}$$

where the grid points and weights are to be determined. The use of a single sum, rather than two one dimensional schemes in Gauss product from discretizing the θ and ϕ integrals individually, leads to fewer total grid points for a similar accuracy. Similar to Gauss quadrature, the computation speed is resultant of using two one-dimension integrals. However, Lebedev quadrature simplifies the use of any symmetry of the integrand to remove unnecessary points. Lebedev quadrature can achieve the same kind of accuracy as the Gaussian product scheme using less quadrature points (order of roughly $\frac{2}{3}$) [73]. As a result, the Lebedev quadratures need less function evaluations and will result in a faster integration scheme if the nodes and weights are precomputed. As depicted in Table 3.1, Lebedev quadrature determines the root and corresponding weights with the fastest computational time.

Table 3.1: Computational time to compute roots and weights of a 5th order polynomial using various quadrature schemes

Quadrature Scheme	Computational Time (sec)
Gauss	0.789227
Chebyshev	2.429716
Lebedev	0.317689

Lebedev quadrature is essentially an advanced method for arranging evaluation points such that their distribution is approximately even, and consequently their weights are not uniform [63].

3.4 Surface function approximation for axisymmetric bodies

As formulated in [76], if a surface is given by

$$\boldsymbol{x}(r,\phi) = r\cos\phi\hat{x} + r\sin\phi\hat{y} + F(r)\hat{z} \tag{3.10}$$

And $z = F(r)$ is a continuous, smooth function where $0 \leq r \leq R$ in (r, z). Each point (r, ϕ) has tangents:

$$\begin{aligned} \boldsymbol{T}_r &= \frac{\partial}{\partial r}\boldsymbol{x}(r,\phi) = \cos\phi\hat{x} + \sin\phi\hat{y} + F'(r)\hat{z} \\ \boldsymbol{T}_\phi &= \frac{\partial}{\partial \phi}\boldsymbol{x}(r,\phi) = -r\sin\phi\hat{x} + r\cos\phi\hat{y} \end{aligned} \tag{3.11}$$

The surface integral is

$$\int_S g(x)dS = \iint_S g(r)\left|\boldsymbol{T}_r \times \boldsymbol{T}_\phi\right| dr d\phi \tag{3.12}$$

where

$$\boldsymbol{T}_r \times \boldsymbol{T}_\phi = -rF'(r)\cos\phi\hat{x} - rF'(r)\sin\phi\hat{y} + r\hat{z} \quad \text{and} \quad \left|\boldsymbol{T}_r \times \boldsymbol{T}_\phi\right| = r\sqrt{(F'(r)^2+1)}$$

So, the double integral in equation 3.12 becomes

$$\begin{aligned} \iint_S g(r)\left|\boldsymbol{T}_r \times \boldsymbol{T}_\phi\right| dr d\phi &= \int_0^{2\pi} d\phi \int_0^R g(r) r\sqrt{(F'(r)^2+1)} dr \\ \iint_S g(r)\left|\boldsymbol{T}_r \times \boldsymbol{T}_\phi\right| dr d\phi &= 2\pi \int_0^R g(r) r\sqrt{(F'(r)^2+1)} dr \end{aligned} \tag{3.13}$$

The single integral (equation 3.13) can be evaluated as an approximation once the nodes and their corresponding weights are computed. The number of nodes (vertices) chosen is important. Varying the number of vertices, N, influences the

number of facets and in turn the volume. The results tabulated in Table 3.2 show that a larger number of vertices chosen for Lebedev quadrature, a smaller error there is to the unit sphere volume.

The Lebedev points for $N = 2354$ are seen in Fig. 3.3 and show a distribution with a volume derived by Lebedev closest to the sphere volume. For the following Lebedev quadrature tests, $N = 2500$ will be chosen to maximize the distribution of points. The next section presents a list of test cases including quadric level surfaces.

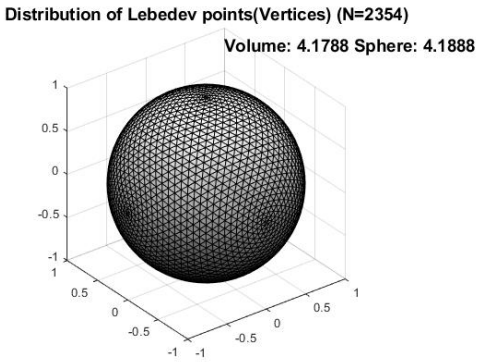

Figure 3.3: Lebedev points and Convex hull distribution for N=2354

Table 3.2: Lebedev volume of Unit sphere for a varying number of vertices

Number of vertices, N	Number of facets	Lebedev volume	Unit sphere volume, $\left(\frac{4}{3}\pi r^3\right)$
266	528	4.0957	4.1888
350	696	4.1191	4.1888
590	1176	4.1488	4.1888
974	1944	4.1646	4.1888
2354	4704	4.1788	4.1888

3.5 Results and Discussion

Test cases from axisymmetric bodies were used to study the efficacy of this approach over tessellation in simulation.

3.5.1 Non-symmetric asteroid

43 Ariadne is a sizeable main-belt asteroid. Using the 3D vertex coordinates of 43 Ariadne generated from the Database of Asteroid Models from Inversion Techniques (DAMIT) software suite written by Joseph Durech and applying Delaunay triangulation (a form of tessellation) gives us the facets on the shape model (See Fig. 3.4).

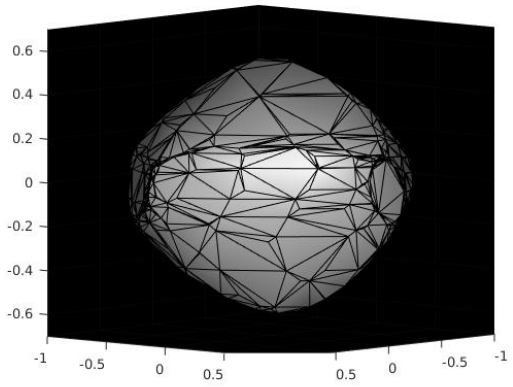

Figure 3.4: Asteroid 43 Ariadne as seen by the observer at 0°

The method used to generate the synthetic light curve from [26] is rationalized succeeding this. The surface reflectance properties were set to include ambient, diffuse and specular reflection ($k_a = 0.5, k_m = 1, k_s = 0.3$ respectively). The motion of the sun with respect to the asteroid is negligible and assumed constant. The lighting conditions are ideal to produce uniform white light at a point source that radiates in all directions. The astrocentric coordinates of the Sun at the first observed Julian date and the observer's location are both facing the target. The light is interpolated

linearly across each triangular facet using the vertex normals. Since this RSO is resolved, we are aware of its ecliptic pole coordinates as $\lambda = -15°$ and $\beta = 253°$. We can then permute 1 full rotation of 360° about this spin axis orientation, resulting in a light curve (See Fig. 3.6).

It is difficult to explicitly define the shape as the form of the function is too complex. However, we can approximate it at best using a stellated octahedron with the following equation

$$f(x, y, z) = a\left(x^2y^2 + y^2z^2 + x^2z^2\right) + b\left(x^2 + y^2 + z^2\right)^2 + c\left(x^2 + y^2 + z^2\right) + d = 0 \tag{3.14}$$

where $a = 1, b = 0, c = -1, d < 0$ for it to be a real quartic surface [77]. The reconstructed shape using the above-mentioned surface approximation function is depicted in Figure 3.5.

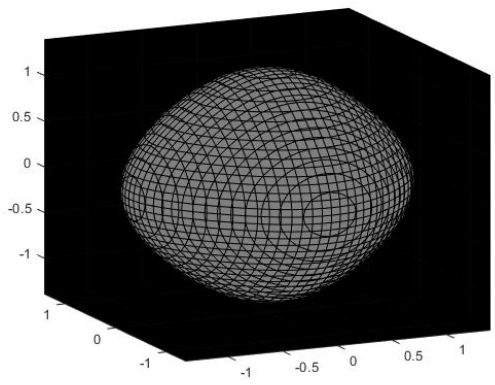

Figure 3.5: Ariadne 43 shape reconstruction using an octahedron

The synthetic light curve generated using the octahedron is viewed in Fig. 3.6. The shape of the light curves permuted from both methods (after normalization of

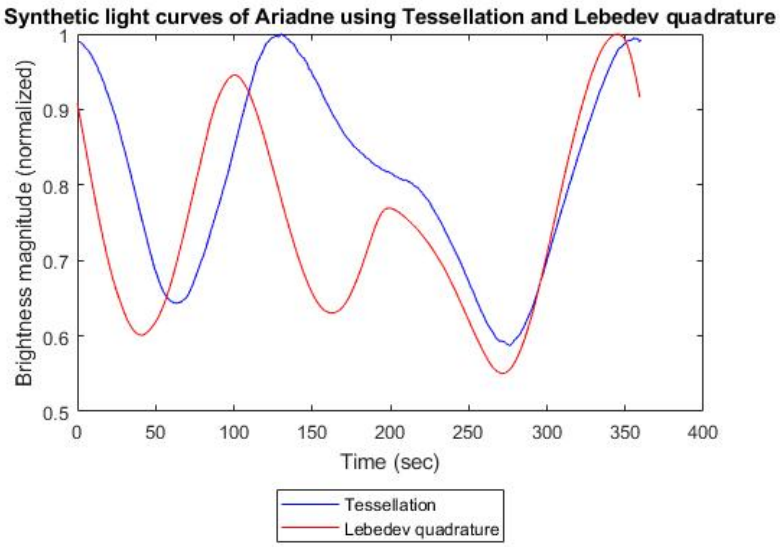

Figure 3.6: Simulated light curve of Ariadne using a tessellated surface and Lebedev quadrature (octahedron)

magnitude and bias removal) are quite similar with the exception of slight horizontal displacement in the location of the first trough. They can overlap with relative accuracy with some discrepancies found in the middle of the curve. This can be attributed to the uneven shape of Ariadne and its sparse, flat facets as opposed to smooth, round edges.

3.5.2 Axisymmetric bodies

3.5.2.1 Cylinder

The general equation of a cylinder with an ellipse cross-section centered about the z-axis is given by $\frac{x^2}{a^2} + \frac{y^2}{b^2} = 1$

If $a = b$, then the cylinder will have a circular base, which simplifies the equation. The light curve generated using Lebedev quadrature is shown in Fig. 3.7. Comparing the errors in area generated by tessellation and Lebedev quadrature (See Fig. 3.8),

the error due to Lebedev is a lot smaller by several orders. The number of triangular facets needed is also significantly lower for Lebedev quadrature. Lebedev quadrature is able to provide full coverage of the object with much lower number of facets, in turn decreasing the number of iterations required to compute the surface integral.

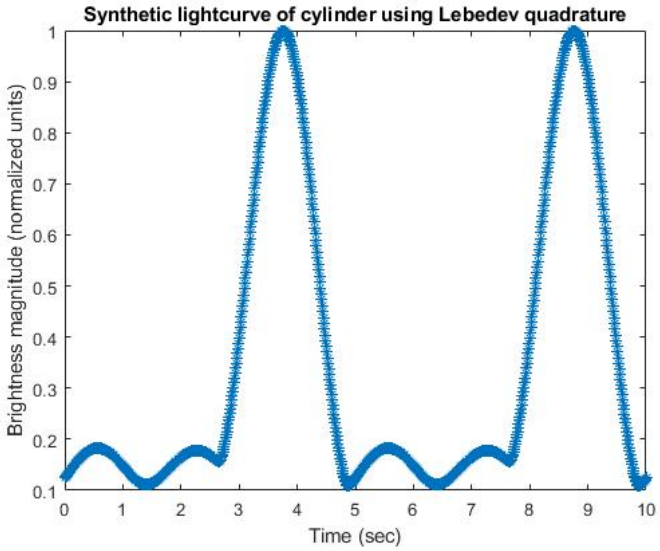

Figure 3.7: Synthetic light curve generated by Lebedev quadrature for Cylinder

3.5.2.2 Cone

The general equation of an upside-down right circular cone (base facing the positive z-axis) is $\frac{x^2}{a^2} + \frac{y^2}{b^2} = \frac{z^2}{c^2}$ where z can be rearranged to a positive and negative root (i.e. the orientation of the cone is upright or upside down). For this case, we will only assume one root i.e $z = \sqrt{\frac{c^2}{a^2}x^2 + \frac{c^2}{b^2}y^2}$.

The light curve generated through Lebedev quadrature where $a = 10, b = 8$ and $c = 6$ is shown below in Fig. 3.9.

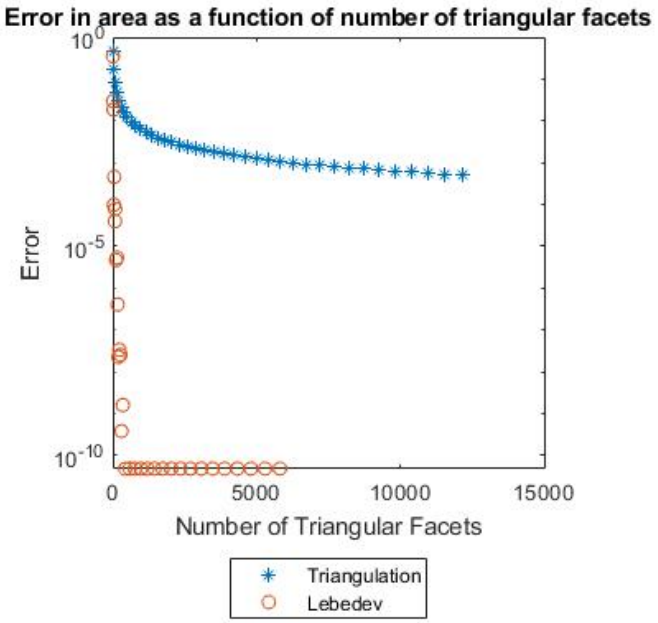

Figure 3.8: Error in surface area through tessellation and Lebedev quadrature as a function of triangular facets

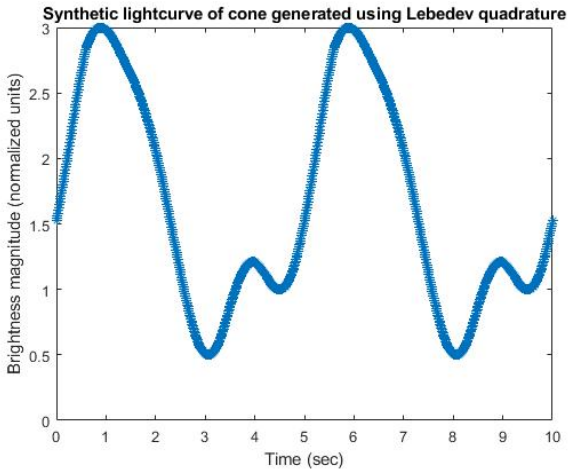

Figure 3.9: Synthetic light curve generated by Lebedev quadrature for Cone

3.5.2.3 Rocket body with nose cone

This is a combined geometry of the cylinder and cone, also known as cylindro-conical shape. Since a cone is an apex of the cylinder, we can also think of this as

two cylinders with $\frac{2}{3}$ of the volume extruded from one of the cylinders. This is of particular interest in the scientific community to determine the attitude motion of disposed upper-stages. However, the optical observations are made with a simplifying assumption of cylindrical diffusely reflecting cylinders [78].

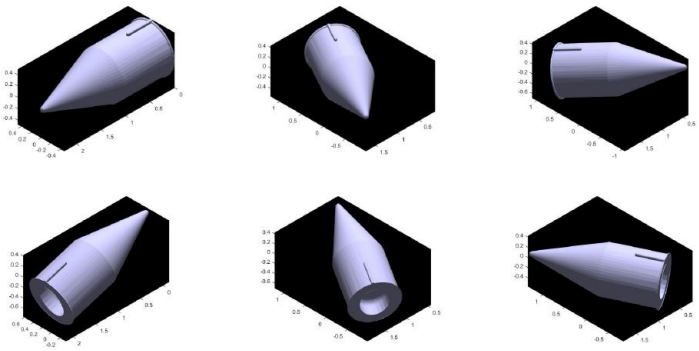

Figure 3.10: Different geometries of Rocket nose cone at specified angles of rotation as seen by the observer. 1st Row: (Left to Right) 60°, 120°, 180°, 2nd Row: (Left to Right) 240°, 300°, 360°

On the contrary, the material surface properties were set to include ambient, diffuse and specular reflection ($k_a = 0.8, k_d = 0.1, k_s = 1$ respectively). Rocket nose cones are primarily made of plastic, fiberglass and hardwood, hence the choices of reflective properties. The spin axis orientation is user-defined as $\lambda = -20°$ and $\beta = 90°$. Tumbling effects are ignored in this scenario. Performing a 360° rotation about its own spin axis has produced the light curve generated by tessellation (See Fig. 3.11). Comparing this to the light curve generated by Lebedev quadrature in Fig. 3.11, we observe that the trend and underlying behavior of the light curves are quite similar. There are a few outliers in the former light curve, which could be a result of the simulation's lighting conditions. However, most notable is that after normalization and removal of bias, the inverted peaks are aligned quite well.

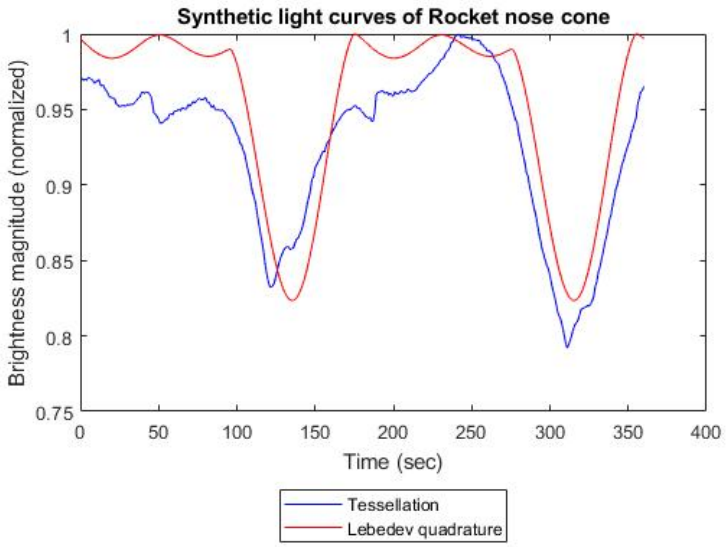

Figure 3.11: Simulated light curve of Rocket nose cone using a tessellated surface and Lebedev quadrature

3.5.2.4 Torus

The torus is the surface generated by the revolution of a circle around a line of its plane; it is therefore a tube with constant diameter and circular bore. It can be useful to estimate rings and disks found in satellites and antennas. As a rational quartic surface, the cartesian equation is $\left(x^2+y^2+z^2+a^2-b^2\right)^2 = 4a^2\left(x^2+y^2\right)$ where a and b are the major and minor radius, respectively. The shape model is seen in Fig. 3.12 and its corresponding light curve is shown in Fig. 3.13. The light curve has peculiar characteristics of resembling a sinusoid with truncated troughs.

3.5.2.5 Peanut-shaped asteroid

This is based on a Cassini oval (2D plane curve) where the product of distances to two fixed points P_1 and P_2 is constant (i.e. $|PP_1|, |PP_2|$). If the foci are located at

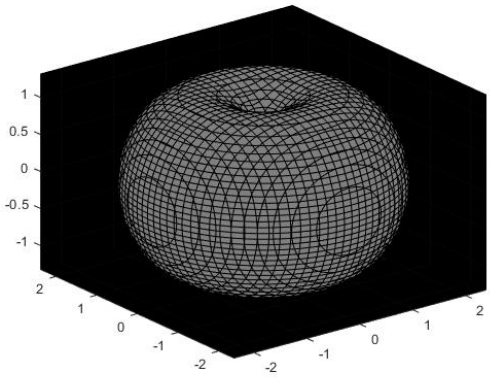

Figure 3.12: Torus model with $b = 1.1a$ and reflectance properties of artificial object

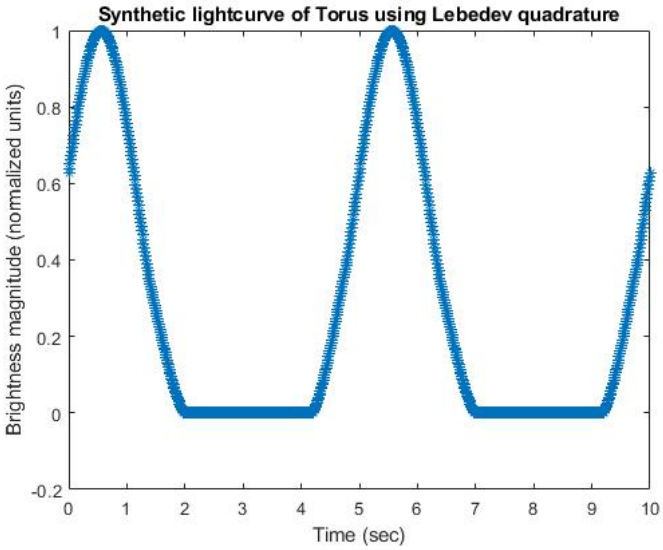

Figure 3.13: Synthetic light curve of Torus using Lebedev quadrature

$(a, 0)$ and $(-a, 0)$, the equation of the 2D curve is $\left(x^2 + y^2\right)^2 - 2a^2\left(x^2 - y^2\right) + a^4 = b^4$ where $a = 1$ and $b = 1.1a$. The level surface in 3D (Fig. 3.14) then becomes

$$f(x, y, z) = \left(x^2 + y^2 + z^2\right)^2 - 2a^2\left(x^2 - y^2 - z^2\right) + a^4 - b^4 = 0$$

The light curve generated through Lebedev is shown in Fig. 3.15.

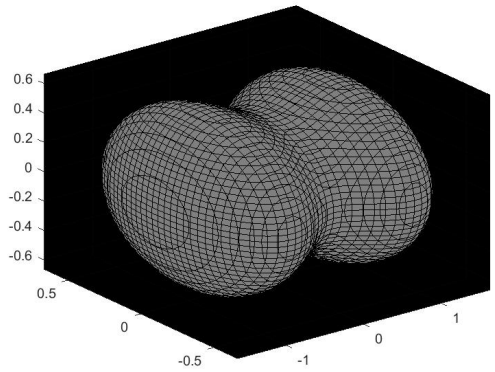

Figure 3.14: Peanut-shaped asteroid generated through tessellation with applied material surface properties

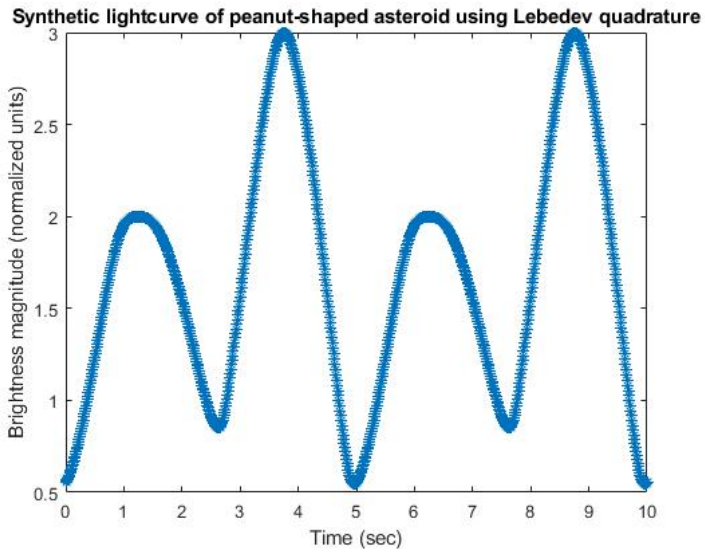

Figure 3.15: Synthetic light curve generated by Lebedev quadrature for peanut-shaped asteroid

The asteroid, Ariadne, is resolved and we have real light-curve data [72] to validate our method. However, for the remaining artificial bodies, reference values are computed using the simulated object's light curve, where a frame is captured each second by the camera and its mean intensity is calculated. The rocket nose cone can be assimilated to an upper-stage body. The error is determined by calculating the

difference between the "truth" value and the quadrature result, and is tabulated below in Table 3.3. As expected, the objects relying heavily on superposition of multiple geometric models (i.e. rocket nose cone) has a larger relative error in contrast with simpler shapes such as the cylinder. The octahedron also produces an increased error since it's a symmetric approximation and the asteroid is an uneven surface.

Surface function	Error (Magnitude order)
Octahedron	10^{0}
Cylinder	10^{-3}
Cone	10^{-2}
Rocket-body	10^{0}
Torus	10^{-2}
Peanut-Shaped	10^{-1}

Table 3.3: Relative error in the approximation of the surface integral

Some light curves generated through tessellation and Lebedev may overlap one another with some difference in the magnitude (at peaks and troughs), but it is not possible to declare one more accurate in this situation since it's derived through a simulation. With no reference to compare it to, a better means would be to compute the rotational period of the target objects about its spin axis and correlate the error in the period to an scaled error for light curve generation. Furthermore, there are advantages of the Lebedev quadrature over tessellation that are detailed below.

Remark: The choice of Lebedev quadrature to compute the brightness integral of a space object (especially in artificial bodies) is recommended as opposed to tessellation, especially if the object has not been resolved. Representing the surface by a set of triangular facets for tessellation has been previously tested on natural, convex bodies which have already been resolved. On the other hand, Lebedev quadrature eliminates the dependence on a priori knowledge of the object's faces and vertices to form triangular

facets. As opposed to other quadrature schemes, Lebedev approximates the integral with a non-uniform weight distribution and providing an additional computational advantage.

3.6 Conclusion and Future Work

Compared to tessellation, Lebedev quadrature has a better scheme for computing surface brightness integrals for axisymmetric bodies, and provides a lower relative error approximation. The computational times are also significantly faster than using Delaunay Triangulation. Unlike common geometric shapes, for composite bodies such as the rocket nose cone, the complexity is significantly higher, so error persists, and synthetic light curves do not resemble one another obtained through both means.

Future work entails varying the reflectance properties of the rocket body such that the cone is entirely dull (non-reflective) and a validation can be performed to see its equivalence to the cylinder test case. Similarly, changing certain portions of an object to have differing reflectance properties and evaluating its effect in comparison with the body in its entirety would be of interest (similar to the mixed-brightness integral in [79]). Quasi-uniform distributions of relatively low numbers of nodes [68] can be applied to simpler artificial objects to verify variability of quality [80].

Chapter 4

RSO light curve classification using neural networks

4.1 Introduction

As the number of artificial space objects increase, the availability of astrometric and photometric data obtained commercially along with high cadence of observations makes it difficult to sustain continuous and real time analysis [81]. The state of a satellite cannot be assumed constant and therefore requires machine classification if near real time assessment of a larger number of objects is desired. Machine learning techniques have been used to analyze variable stars [82], however there isn't a big data problem with artificial space objects unlike astronomical/stellar objects. As deep space becomes increasingly congested and anomalous events are common, it is essential to the space situational awareness (SSA) community to have the tools to close awareness gaps and reduce information latency [81]. The requirement of timeliness and the consideration of a non-stationary state are unique to man-made objects. As such, we are considering both active, stabilized objects as well as inactive, tumbling objects.

The light curve observations are readily available to exploit for classification purposes. Currently, time series data are seen in a varied range of applications and numerous clustering and classification methods were developed [83]. Time series classification is a supervised machine learning problem aimed for labeling multivariate series of variable length [84]. Time series data often have a very high dimensionality and thus, a broad number of features can be extracted making classification arduous [85,86]. Instead of applying classification methods on raw time series data, as it's not very

practical, we can employ a higher-level representation [83]. One such type of higher-level representation is window-based representation. Some examples include Piecewise Aggregate Approximation [87], Trend-based and Value-based Approximation [86], and Symbolic Aggregate Approximation [85]. In window-based representation, the whole time series is divided into a sequence of equal sized windows (segments). One or more features are extracted from each frame, and a vector of these features becomes the data-reduced representation. Subsequently, the created vectors are used to train a classifier. A few commonly used classifiers are listed as follows: Rule Induction, Support Vector Machine (SVM), Neural Network (NN). When using any of the above-mentioned classifiers, the temporal relations present in time series data are ignored, leading to inaccurate results. To solve this issue, multiple classifiers can be utilized to improve the accuracy of time series classifiers. The viability of using multiple classifiers are evidenced in [88, 89] and have been found better performing than those of single classifier systems. Adding a Hidden Markov Model (HMM) to a Recurrent neural network (RNN) is proposed for this study. This modification will incorporate temporality of the data, and execute a second stage classification to remove any redundancy and check for misclassification from the first level of screening.

Representation learning allows the model to extract important features to characterize objects according to physical property one by one [90]. Initially, this may limit model interpretability however, it provides an opportunity for hidden features of the light curve to surface and help in classifying an object. Feature engineering is the process of determining, calculating, and extracting features from raw data. These features are typically properties of the raw data that can be understood by humans and believed to provide insight on the prediction task. Feature analysis of time series (FATS) [91] has been able to extract features from stellar light curves and proven successful for regression. While feature engineering can be computationally extensive,

representation learning has the opportunity to remove human-based preconceived notions about factors affecting classification [90]. The Long-Short Term Memory (LSTM) RNN is chosen so that the model can learn both relations between flux values in a sequence and general patterns of all objects, allowing accurate predictions.

This chapter outlines the various types of neural networks and mathematical background for the Hidden Markov Model. Details of the classification model are included with the aggregation of Long-Short Term Memory (LSTM) RNN to the HMM. Identifiers (labels) by which classification of light curves are performed as well as the tests to ensure accuracy are then explained. Results from training a set of simulated objects will conclude this section.

4.2 Neural Networks

There are three important types of neural networks that form the basis for most prior-trained models in machine learning: Artificial Neural Networks (ANN), Convolution Neural Networks (CNN), and Recurrent Neural Networks (RNN). The three types of neural networks have been examined and evaluated for its feasibility for this application below.

4.2.1 Artificial Neural Network (ANN)

The fundamental element of an Artificial Neural Network is a single perceptron (or neuron). ANN is a group of multiple perceptrons at each layer, in which the outputs of one layer are provided as the inputs to the neurons of the subsequent layer (See Fig. 4.1) (from [92]). ANN is also known as a Feed-Forward neural network because inputs are processed only in the forward direction. ANN can be used to solve problems related to: tabular data, image data, and text data.

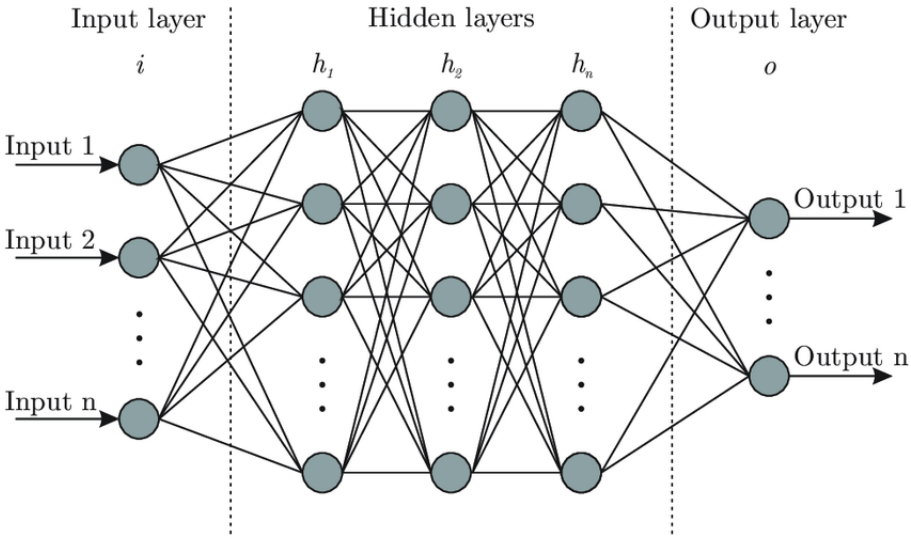

Figure 4.1: Architecture of an ANN

Artificial Neural Network is capable of learning any nonlinear function. Hence, these networks are popularly known as Universal Function Approximators. ANNs have the capacity to learn weights that map any input to the output. The inputs to a neuron are each individually multiplied by weights and the results summed [6]. This value is given as input to a non-linear activation function that produces the neuron's output activation. One of the main reasons behind universal approximation is the activation function. Activation functions introduce nonlinear properties to the network. This helps the network learn any complex relationship between input and output. Theoretically, ANNs that use non-linear activation functions could replicate the mapping of any training set, given that the network contained a sufficient number of neurons [93].

There are various ANN optimizers, such as Stochastic Gradient Descent (SGD), RMSProp, and Adam [94], to name a few, that are used in the training process. The typical approach to design an ANN is to limit the width of each hidden layer, but include many layers (making it deep) [93]. This leads to overfitting, since these

networks have a larger capacity than required [6]. To overcome this problem, several regularization techniques (i.e. batch normalization) exist to counteract the impact of updating layers sequentially. Another option would be to utilize a dropout layer, where it randomly removes a percentage of neurons (by setting those neurons' activations to 0) during each training batch. Although this may mitigate overfitting, a negative consequence is a slower training rate.

One common problem in all these neural networks is the Vanishing and Exploding Gradient. This problem is associated with the back-propagation algorithm. The weights of a neural network are updated through this back-propagation algorithm by finding the gradients. So, in the case of a very deep neural network, the gradient vanishes or explodes as it propagates backward which leads to vanishing and exploding gradient. ANN cannot capture sequential information in the input data which is required for dealing with sequence data.

4.2.2 Convolutional Neural Network (CNN)

Convolutional neural networks are especially prevalent in image and video classification. With the enormous number of pixels in an image, processing each pixel as an individual feature is unreasonable. CNNs are able to provide some degree of weight sharing through two unique layers: convolutional layers and pooling layers [6].

Convolution is a signal processing technique wherein a small kernel is applied to a source signal [93]. Since images don't have a time component, the kernel is instead moved spatially and the output is effectively a new image. Convolution layers apply a collection of kernels to the input, where a single kernel is applied across different parts of an input to produce a feature map. Each kernel can contain multiple trainable weights, hence weight sharing. The building blocks of CNNs are kernels (sometimes called filters), which are used to extract the relevant spatial features from the input,

such as arrangement of pixels and the relationship between them in an image. They help us in identifying the object accurately, the location of an object, as well as its relation with other objects in an image.

Pooling is a regularization technique to combat overfitting [93]. Pooling is typically accomplished via the maximum, minimum, or average function. A pooling layer will have some sample rate, and will combine pixels of its inputs using the aforementioned function at whatever rate is desired [6]. Pooling layers are usually intertwined throughout a CNN to act as a funnel, in order to ensure the image is sufficiently small (flattened) as it passes through to the fully-connected layer. Pooling layers group local features from spatially adjacent pixels to improve robustness [8].

The Convolutional layer is the most demanding layer in terms of computations from summing the products across all regions. Mathematically, the convolutional layer as described in [8] is as follows:

$$(X * Y)(i, j) = \sum_{n=0}^{N} \sum_{m=0}^{M} X_{m,n} * W_{i-m,j-n} \tag{4.1}$$

where, W is the convolution kernel corresponding to the randomly initialized weights, and X is the image with indices (m, n). CNN uses the ReLU function (i.e., Rectified Linear Unit) defined as $f(x) = max(0, x)$ as its nonlinear activation function.

Though convolutional neural networks were introduced to solve problems related to image data, they perform impressively on sequential inputs as well. CNNs are easier to train due to parameter (weight) sharing and are trained in batches via SGD. Similar to the ANN, the dropout technique improves generalization and avoids overfitting [8].

4.2.3 Recurrent Neural Network (RNN)

RNN has a recurrent connection on the hidden state, which allows for feedback (a major difference from ANN). The outputs of previous time steps will be considered as inputs in the current time step, and the results of the current time step will impact the calculation of the next time step. This looping constraint ensures that sequential information is captured in the input data. We can use recurrent neural networks to solve the problems related to: time series data, text data, and audio data.

Given $\boldsymbol{x_1}, \boldsymbol{x_2}, \ldots, \boldsymbol{x_n}$ are the input vectors, $\boldsymbol{h_1}, \boldsymbol{h_2}, \ldots, \boldsymbol{h_n}$ are the hidden cell vectors and $\boldsymbol{y_1}, \boldsymbol{y_2}, \ldots, \boldsymbol{y_n}$ are the output vectors, where n represents the total steps, the equations computing result vectors [95] are defined below:

$$\begin{aligned} \boldsymbol{h}_t &= \theta \phi_{(\boldsymbol{h}_{t-1})} + \theta_x \boldsymbol{x}_t \\ \boldsymbol{y}_t &= \theta_y \phi_{(\boldsymbol{h}_t)} \end{aligned} \tag{4.2}$$

where $\theta, \theta_x, \theta_y$ are weights, ϕ is the activation function (tanh in most RNNs). The self-connection weight θ is simply initialized as 1. The subsequent back-propagation will adjust all the weights in every iteration.

RNNs share the parameters across different time steps. This results in fewer parameters to train and decreases the computational cost. Deep RNNs also suffer from the vanishing and exploding gradient problem.

The various characteristics of all the above-mentioned neural networks are summarized in Table 4.1. Although all three have a common disadvantage of vanishing and exploding gradient, RNN is the optimal choice for time-series data with the recurrent connections and less computational burden from parameter sharing.

Of the numerous types of RNNs, Long Short-term Memory (LSTM) has been chosen for this application and the logistics and equations are detailed in the following section.

Table 4.1: Attributes of ANN vs. CNN vs. RNN

Attribute	ANN	RNN	CNN
Data compatibility	Tabular	Sequence	Image
Recurrent connections	-	Yes	-
Parameter sharing	-	Yes	Yes
Spatial relationship	-	-	Yes
Vanishing and Exploding gradient	Yes	Yes	Yes

4.2.3.1 Long Short-term Memory (LSTM)

Long Short-term Memory RNN is specifically designed to avoid the long-term dependency problem [96] and there are many slight variations [97]. We will use the definition from [98] in this context. As seen in Fig. 4.2 (from [95]), a cell of LSTM RNN has three gates, which control the involvement of the past context information: input gate, output gate, and forget gate. The latter is used to scale the influence of the previous cell on the current cell state [95].

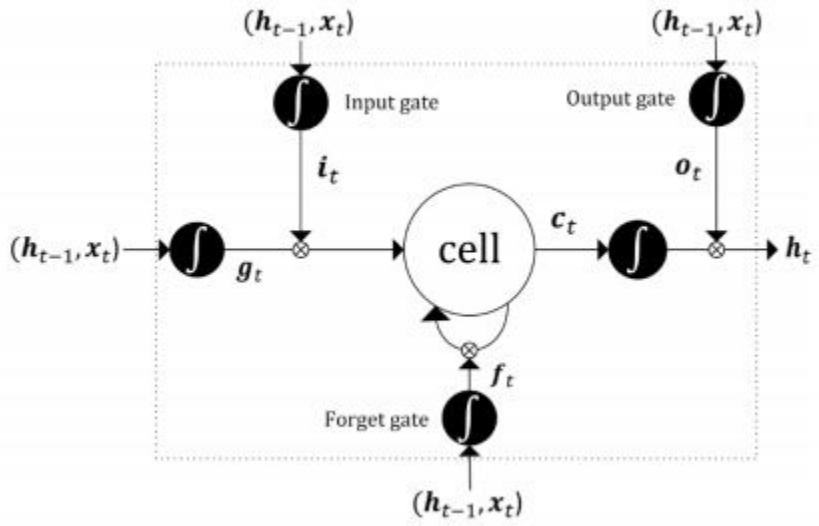

Figure 4.2: LSTM cell structure

The equations for computing the gate outputs are defined below [95]:

$$
\begin{aligned}
\boldsymbol{i}_t &= \sigma\left(\theta_{xi}\boldsymbol{x}_t + \theta_{hi}\boldsymbol{h}_{t-1} + b_{\mathrm{i}}\right) \\
\boldsymbol{f}_t &= \sigma\left(\theta_{xf}\boldsymbol{x}_t + \theta_{hf}\boldsymbol{h}_{t-1} + b_{\mathrm{f}}\right) \\
\boldsymbol{o}_t &= \sigma\left(\theta_{xo}\boldsymbol{x}_t + \theta_{ho}\boldsymbol{h}_{t-1} + b_{0}\right) \\
\boldsymbol{g}_t &= \tanh\left(\theta_{xg}\boldsymbol{x}_t + \theta_{hg}\boldsymbol{h}_{t-1} + b_{\mathrm{g}}\right) \\
\boldsymbol{c}_t &= \boldsymbol{f}_t \cdot \boldsymbol{c}_{t-1} + \boldsymbol{i}_t \cdot \boldsymbol{g}_t \\
\boldsymbol{h}_t &= \boldsymbol{o}_t \cdot \tanh\left(\boldsymbol{c}_t\right)
\end{aligned}
\tag{4.3}
$$

where $\boldsymbol{h}_{t-1}$ is the output of the last time step, $\boldsymbol{x}_t$ is the cell input at the current step, and $\boldsymbol{h}_t$ is the cell output. The t in the subscripts represents the current step number. The $\boldsymbol{i}, \boldsymbol{f}, \boldsymbol{o}$, and $\boldsymbol{g}$ respectively denote the output vectors of input gate, the forget gate, output gate and the cell itself. θ are the weights, for example, θ_{xi} is the weight between the input vector $\boldsymbol{x}_t$ and the input gate vector $\boldsymbol{i}_t$, θ_{hi} is the weight between the output vector $\boldsymbol{h}_{t-1}$ and the gate vector $\boldsymbol{i}_t$. b represents biases, $\boldsymbol{c}_t$ and $\boldsymbol{c}_{t-1}$ are the cell outputs in the current step and the previous step, respectively, and σ represents a sigmoid function (output 0 to 1). LSTM usually limits the activation function to tanh (output -1 to 1) for $\boldsymbol{g}_t$ and $\boldsymbol{h}_t$, and sigmoid for $\boldsymbol{i}_t$, $\boldsymbol{f}_t$, and $\boldsymbol{o}_t$. Other activation functions, like rectified linear unit (ReLU), make LSTM diverge [99], hence, the sigmoid and tanh are suitable choices.

Generally, the RNN cannot retrieve data deep into its memory and LSTM RNN brought forth a solution [100]. LSTM RNN has become a popular choice for modeling inherently dynamic processes [95] and is expected to result in a high accuracy.

4.3 Hidden Markov Model (HMM)

A Markov chain satisfies the Markov property (Eq. 4.4) where the next state depends only on the current state and not on the sequence of states that preceded it [101]. The model consists of a finite number of states $\{s_1, s_2, \ldots, s_n\}$ and some

known probabilities $\boldsymbol{P} = \{p_{ij}\}$ where p_{ij} is the probability of moving from state s_i to the state s_j [83].

$$P\left(s_{t+1} \mid s_0, s_1, \ldots, s_t\right) = P\left(s_{t+1} \mid s_t\right) \tag{4.4}$$

Hidden Markov model (HMM) is a Markov chain in which the observations, dependent on the state, are visible instead of states. Each state has a probability distribution over the possible output observations. The sequence of observations is linked to its corresponding sequence of states. In a HMM, the observer does not know which state the system is in, but only a probabilistic insight on where it should be. It is defined by equation 4.5 as formulated in [83].

$$\boldsymbol{\mu} = (\boldsymbol{S}, \boldsymbol{O}, \boldsymbol{A}, \boldsymbol{B}, \boldsymbol{\pi}) \tag{4.5}$$

where $\boldsymbol{S} = \{s_1, s_2, \ldots, s_n\}$ is the set of hidden states, $\boldsymbol{O} = \{o_1, o_2, \ldots, o_m\}$ is the set of observations, $\boldsymbol{A}$ is the transition matrix, $\boldsymbol{B}$ is the emission matrix, and $\boldsymbol{\pi}$ is the initial state matrix, where π_i is the probability that state s_i is a start state. The matrices have been defined in the following equations.

$$\boldsymbol{A} = \{a_{ij}\}, \quad a_{ij} = P\left(s_j \mid s_i\right) \quad for \quad i, j = 1, 2, \ldots, n \tag{4.6}$$

$$\boldsymbol{B} = \{b_{ij}\}, \quad b_{ij} = P\left(o_j \mid s_i\right) \quad for \quad i = 1, 2, \ldots, n, \quad j = 1, 2, \ldots, m \tag{4.7}$$

$$\pi_i = \frac{1}{\sum S_i} \quad i = 1, 2, \ldots, n \tag{4.8}$$

All states have equal probabilities to be the initial state as depicted in the equation for π_i. The HMM structure is illustrated in Figure 4.3 (from [83]).

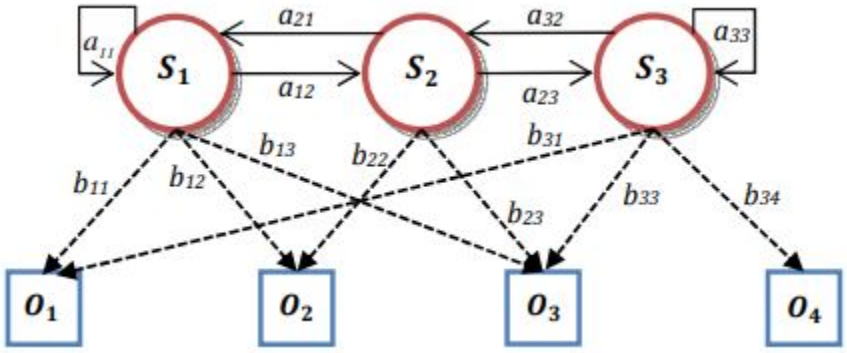

Figure 4.3: Hidden Markov Model

Hidden Markov Models are used to model temporal and sequence data. They are commonly used in temporal pattern recognition such as time series classification [102] and speech recognition [101].

In order to improve the accuracy of the time series classifier, the HMM is trained to evaluate, confirm and correct the classification results performed by the LSTM (initial classifier). The general framework of the approach is sketched in Fig. 4.4 (from [83]) which shows the two phases of this approach. During training phase, the confusion matrix and the classified data outputted by the first classifier will be used. In the classification phase, the trained HMM will be used to reclassify the sequence of classified samples. The correct samples will be confirmed and the misclassified samples will be corrected. Classifying any time series data will require two stages.

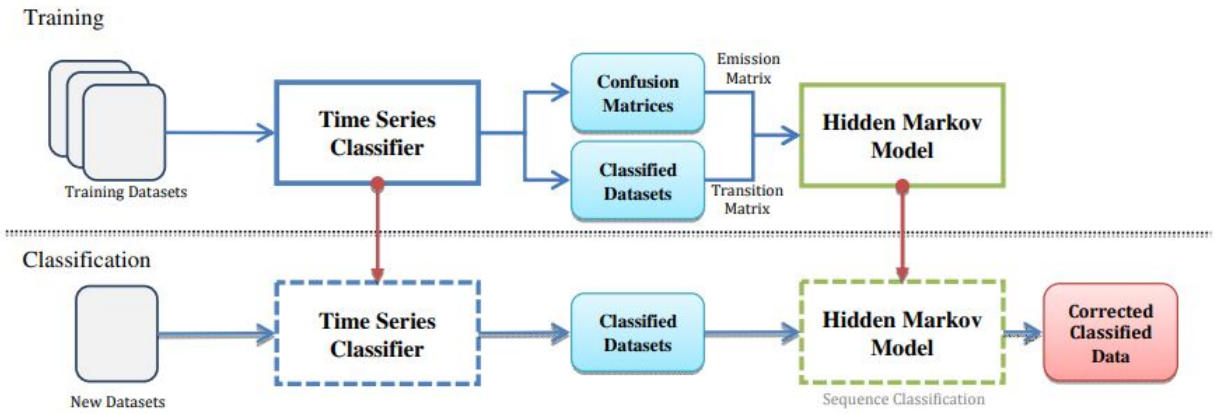

Figure 4.4: General Framework with two phases: Training and Classification

A confusion matrix $\boldsymbol{C} = c_{ij}$ for $i, j = 1, 2, \ldots, n$ is denoted such that c_{ij} represents the number of samples that belong to state s_i but they have been misclassified as s_j. Confusion matrix is also used in computing the emission matrix, $\boldsymbol{B}$.

Unlike traditional classifiers (i.e. SVM, NN), HMM classifies the data on the basis of their temporal relations [83]. To classify a given sequence of observations, we need to find the most likely sequence of states (path) that produces these observations. Viterbi algorithm [103] can be used to find the most likely path as elaborated below.

Algorithm 8 Viterbi algorithm

1: **procedure** CLASSIFICATION($\boldsymbol{\mu}, \boldsymbol{O}$)
2: Input: The trained HMM $\boldsymbol{\mu} = (\boldsymbol{A}, \boldsymbol{B}, \boldsymbol{\pi})$, and a sequence of observations $\boldsymbol{O} = \{o^1, \ldots, o^T\}$
3: Create a path probability matrix $\boldsymbol{V}$
4: **for** $t \leftarrow 0, T$ **do**
5: **for** $s \leftarrow 0, N$ **do**
6: for each transition $i \rightarrow s$
7: $score = v[s,t] \times a[s,i] \times b\,(i, o^t)$
8: **if** $score > v[s,t]$ **then**
9: $v[i, t+1] = score$
10: $backpointer[i, t+1] = s$
11: **end if**
12: **end for**
13: **end for**
14: Choose the highest probability state in final column of $\boldsymbol{V}$ and backtrack to find $\boldsymbol{S}$
15: **return** $\boldsymbol{S}$, a best path of states
16: **end procedure**

4.4 Classification approach

There are different traits by which classification can be performed [7]. Using the taxonomy and classification scheme for artificial space objects [104] as a reference, we have selected attitude and shape as classifiers. We will primarily use light curves of artificial space objects in LEO as the training and testing sets. The first classification determination is made from the control states. For each model in the bank, additional models are created that are copies of that shape model but have different control profiles. The control profiles include (three-axis) spin stabilized, and tumbling/irregular. The control states are not limited to ones used in this work and other states are possible (i.e. regularly spinning/rotating), but for this study, these are sufficient. The next classification is determined using the shape model, either separating it as regular or irregular. Under regular, for example we have objects in the bank such as ellipsoid,

cylinder, cone, cubesat, torus, probe, box-wing satellite, probe, disk and rocket body. Examples of these models have been included in the previous two chapters. If the object cannot be identified as one from the aforementioned list, it will be categorized as an irregular object, which includes fragments.

4.4.1 Sub-classification of Tumbling objects

Light curves of tumbling objects have a wide variety of features than stable objects. Stable satellites tend to have a single main peak around low solar phase angles caused by a solar panel glint [81]. Additionally, observed brightness values tend to have relatively low variance about their trend. On the other hand, tumbling object light curves tend to take one of three forms: sinusoidal, aliased, or multiple. A sinusoidal signature will have several peaks and troughs. An aliased light curve is caused by the sensor sampling at a slow rate (below the Nyquist frequency) to properly capture the periodic behavior. These light curves do not have a distinguishable trend and look like scattered data points. A type of aliasing where it appears as though two distinct trends have been plotted on top of one another is known as multiple form. Residuals about the mean trend have a bi-modal distribution. The sampling rate is too slow, once again, to capture the sinusoidal nature. Additionally, it has been suggested that fine-scale specular glints are causing the bi-modal behavior [81]. Tests to identify these forms respectively are periodicity test, and aliasing test. These have been discussed in further detail below.

4.4.1.1 Periodicity Test

Assuming the data is not aliased, we can test for periodicity to detect the presence of sinusoidal periodic waveforms, which differentiates tumbling from stable objects. One test that can be used to confirm the significance of a signal's periodic

component is Fisher's Exact Test for Periodicity [105]. The test statistic is found by extracting the most significant frequencies. As we noted from the analysis in the chapter for estimation of period, the Lomb-Scargle periodogram will be utilized to find dominant frequencies as it does not require observations to be uniformly spaced, which is rare in real photometric data. If the light curve has a significant periodic component, we will assume that it came from a tumbling object. Since stable objects can have a single peak in its periodogram, a threshold must be set on the period length that would be tested such that the test does not indicate that stable objects are periodic (with a long period). This eliminates false positives.

Outliers are inevitable in photometry and should be removed because they can distract from periodic components that are truly present in a light curve. They also cause some undesired results in the periodogram and in turn, the test for periodicity itself. There are 3 different types of outlier detection methods [106]. Type 1 is applied when there is no prior information for the data (labels). They assume that "normal" points lie in the same region of feature space and that outliers are far from this area. Type 2 is applied when labels for normal and abnormal data are available. They are usually classifiers which are trained with these data and can consequently flag the outliers that belong to the already known outlier classes. Type 3 is applied when only labels for normal data are available. They aim to define the normality boundaries, and anything that does not lie within the normal boundary is flagged as an outlier.

Additionally, there are some frequencies that we do not expect in the light curve from a tumbling object. For instance, if the fundamental frequency of a light curve is too low, that frequency may correspond to one or fewer periods occurring within the observation window. Then this frequency is likely not representative of the tumble rate. Generally, there is a clear peak close to zero for the unstable object's period while the stable objects' periods tend to be much longer [81].

4.4.1.2 Test for aliasing

Since aliasing causes particularly noisy light curves, as a way to identify aliased, tumbling objects from stable objects, we can use a test. An assumption of stationarity is sufficient to give us the ability to detect aliasing in a temporally sampled signal process [107]. We can ensure stationarity using the Augmented Dicky Fuller (ADF) test.

The Augmented Dickey-Fuller test is a unit root test, a type of statistical test. A unit root test determines how strongly a time series is defined by a trend. ADF test is utilized as a measure of confidence to which a null hypothesis can be rejected or fail to be rejected. It uses an autoregressive model and optimizes an information criterion across multiple different lag values. The model is defined as

$$\Delta y_t = \alpha + \beta t + \gamma y_{t-1} + \delta_1 \Delta y_{t-1} + \cdots + \delta_{p-1} \Delta y_{t-v+1} + \varepsilon_t \tag{4.9}$$

where α is a constant, β the coefficient on a time trend and p the lag order of the autoregressive process. By including lags of the order p the ADF formulation allows for higher-order autoregressive processes. The unit root test is then carried out under the null hypothesis $\gamma = 0$ against the alternative hypothesis of $\gamma < 0$.

- Null Hypothesis: If failed to be rejected, it suggests the time series has a unit root, meaning it is non-stationary. It has some time dependent structure.
- Alternate Hypothesis: The null hypothesis is rejected; it suggests the time series does not have a unit root, meaning it is stationary. It does not have time-dependent structure.

  We interpret this result using the p-value from the test.

$$\begin{cases} \text{Non-stationary time series,} & \text{if } p - value > 0.05 \\ \text{Stationary time series,} & \text{otherwise} \end{cases}$$

The test outputs a statistic value and if it leans more negative, there is a higher probability to reject the null hypothesis. Comparing it to the lookup critical values $(1\%, 5\%, 10\%)$ determines significance of accuracy and can eliminate the possibility of statistical flukes. An example of the Augmented Dicky-Fuller test results are portrayed in Fig. 4.5 where the p-value satisfies the alternate hypothesis. The ADF-statistic's absolute value is greater than the critical value at 1% implying a higher confidence level in the data being stationary.

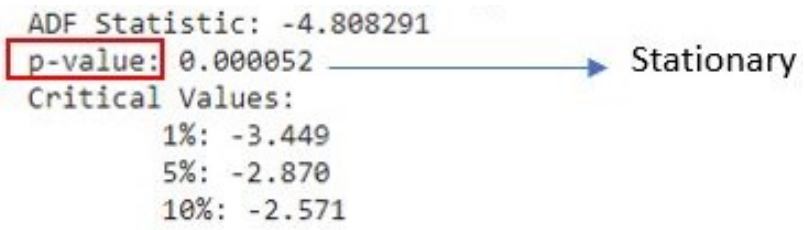

Figure 4.5: Results of the ADF test on a stationary time-series

Once this is confirmed, we can use bispectral analysis to identify aliased signals. The domain of the bispectrum of a discrete-time signal is a periodic function in two dimensional frequency plane $\{\omega_1, \omega_2\}$. The bispectrum, defined to be the triple Fourier transform of the third-order autocorrelation, reduces to a function of two frequencies since stationarity confines the spectrum to the plane through the origin of the frequency domain perpendicular to the vector $(1, 1, 1)$ [108].

Assuming a real-valued discrete time series, all non-redundant information is confined to the square $0 \leq \omega_1, \omega_2 \leq \pi$. Due to symmetries, the non-redundant information in the bispectrum is confined to a particular triangle inside this square.

The triangle consists of two pieces (isosceles and irregular). The region inside the triangle could include frequencies higher than the Nyquist frequency and can lend itself to possible aliasing. If the sampling rate is sufficiently rapid to avoid aliasing, then the discrete bispectrum is non-zero only in the isosceles triangular subset of the fundamental domain and therefore no aliasing is present [108]. On the contrary, if the bispectrum is non-zero in the outer triangle, then the sampling rate was too slow to avoid aliasing. The bispectrum of a sampled signal is visible in Fig. 4.6, where we see that it is non-zero within the isosceles triangle only. Upon closer inspection, we notice specks of a different color indicating magnitudes larger than the vicinity in the z-axis. We can assert that the outer-triangle does not show a non-zero bispectrum, hence the underlying signal must not have been aliased.

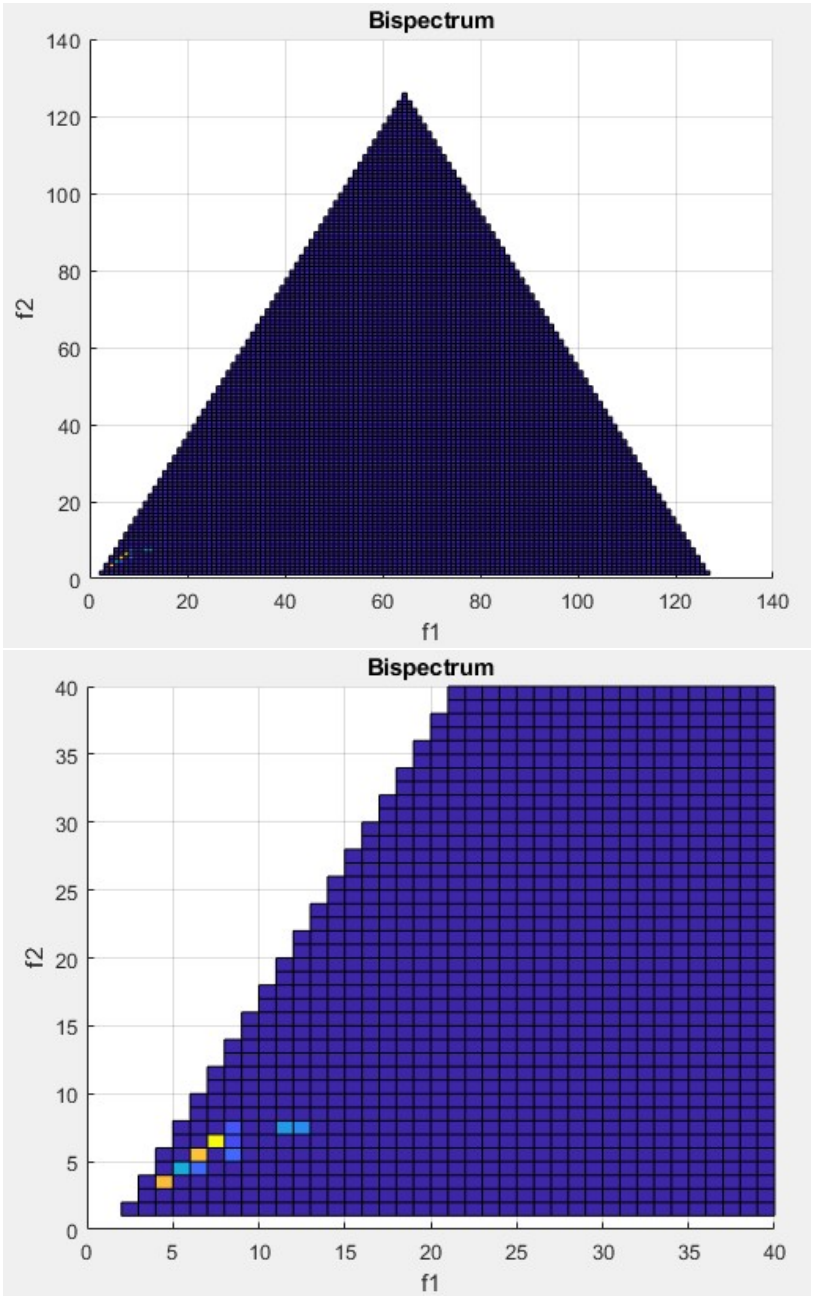

Figure 4.6: Bispectrum of a nonaliased signal (Top) and zoomed-in results (Bottom)

4.4.2 Feature extraction

Certain features in a light curve can be correlated to physical structures on objects. The primary light curve features are narrow and broad brightness peaks

correlating to structures such as the main payload enclosure, solar panels, and communications antennas. Large antennas are often located on the eastern and/or western sides of the nadir-facing main body as seen in a box-wing satellite. This asymmetry is observed in the reflected light of the photometric curves. Narrow features are narrow peaks whereas broad features include either a broad peak or a shoulder [81]. Feature extraction prior to classification is essential as it can remove irrelevant and redundant features to improve classification accuracy [109]. Many transformation methods reduce the dimension of the data. There is a need for non-model-based methods [5]. Traditional frequency-domain methods (i.e. FFT) do not capture time-varying behavior while wavelet decomposition is well-suited for real-time applications. We can extract the feature information via wavelet decomposition, which is elaborated in the next section.

4.4.2.1 Wavelet Analysis

Fourier Transform produces a frequency spectrum of the signal, while losing time resolution since we are unaware of when that frequency occurs. To obtain both frequency and time resolution, we can split the original signal into several parts and apply a Fourier Transform to each one. This approach of obtaining the frequency content of a signal locally in time was a windowing technique applied to the signal, called the Short Time Fourier Transform (STFT) that maps a signal into a two-dimensional function of time and frequency [110]. STFT raises new concerns when applying it to the partial signal, since the frequency range that it can detect is $n/2$, where n is the length of the partial signal. The time/frequency window of the STFT is fixed and hence unsuitable for detecting signals with both high and/or low frequencies. Wavelet analysis is an extension of the STFT in such a way that the window is no longer fixed, but can be varied. The Wavelet Transform approach automatically

adjusts the window width to give good time resolution and poor frequency resolution at high frequencies, and good frequency resolution and poor time resolution at low frequencies [111].

A wavelet is a sum of elementary functions with two requirements that it should integrate to zero, waving above and below the x-axis, and that the function has to be well-localized. They have limited duration and tend to be irregular and asymmetric [110]. The use of long time intervals for precise low frequency information, and shorter intervals for high frequency information is accomplished through the use of a location parameter and a scale parameter, whereas the Fourier method only has the latter. One of the two parameters is the translation or location parameter. The other parameter is a dilation or scale parameter, the latter corresponding to the frequency in the Fourier case.

The basic formula of wavelets is

$$X_{a,b} = \int_{-\infty}^{\infty} x(t)\psi_{a,b}(t)dt \tag{4.10}$$

where x is the real signal, ψ is an arbitrary mother wavelet, a is the scale and b is the translation.

There are many types of mother wavelets and the objective is to seek for the non-zero magnitudes of the mother wavelet. The scale is inversely proportional to the frequency of the mother wavelet and the same as the size of the window. The translation parameter is analogous to how far we "slide" the window from the starting point.

Wavelet Transform is divided into two classes: Continuous Wavelet Transform (CWT) and Discrete Wavelet Transform (DWT). CWT allows us to set the scale and translation to an arbitrary value. Some commonly used mother wavelets that

belong to CWT are Morlet, Meyer, Mexican Hat. DWT restricts the value of the scale and translation. Mother wavelets commonly used in DWT are Haar, Daubechies. Daubechies wavelet has a unique scaling restriction; it has a scaling function called a Father Wavelet to determine the right scale. An example of mother wavelets for CWT and DWT are represented visually in Figure 4.7.

By applying the Discrete Wavelet Transform (DWT) on a signal, we can deconstruct its frequency sub-bands, also known as wavelet decomposition. Out of each sub-band we can generate features which can be used as inputs for a classifier [112]. DWT is utilized to extract the wavelet coefficients: approximation and detail. The approximation coefficients represent the output of the low pass filter (averaging filter) of the DWT. The detail coefficients represent the output of the high pass filter (difference filter) of the DWT. By applying the DWT again on the approximation coefficients of the previous DWT, we get the wavelet transform of the next level. At each next level, the original signal is also sampled down by a factor of 2 (de-noising). These respective properties are depicted in Fig. 4.8.

The Wavelet Transform automatically adjusts the window width to give good time resolution and poor frequency resolution at high frequencies, and good frequency resolution and poor time resolution at low frequencies [111]. The limit of the time and frequency resolutions is given by $\Delta t \Delta f \geq \frac{1}{4\pi}$. If a coefficient scores a high statistic value, data (in terms of this coefficient) can be easily separated by the classifier.

To preface the results in Fig. 4.9, the rocket nose cone's light curve has produced a spectrogram with pixels representing frequency-time coordinates, after the DWT. Dominant modes are referred to by the legend and correlate to the change in magnitude of the signal (i.e. peaks, saddle points). The signal when decomposed using a combination of low-pass and high-pass filters results in the approximation and detail (horizontal, vertical, and diagonal) coefficients is seen in Fig. 4.10. One

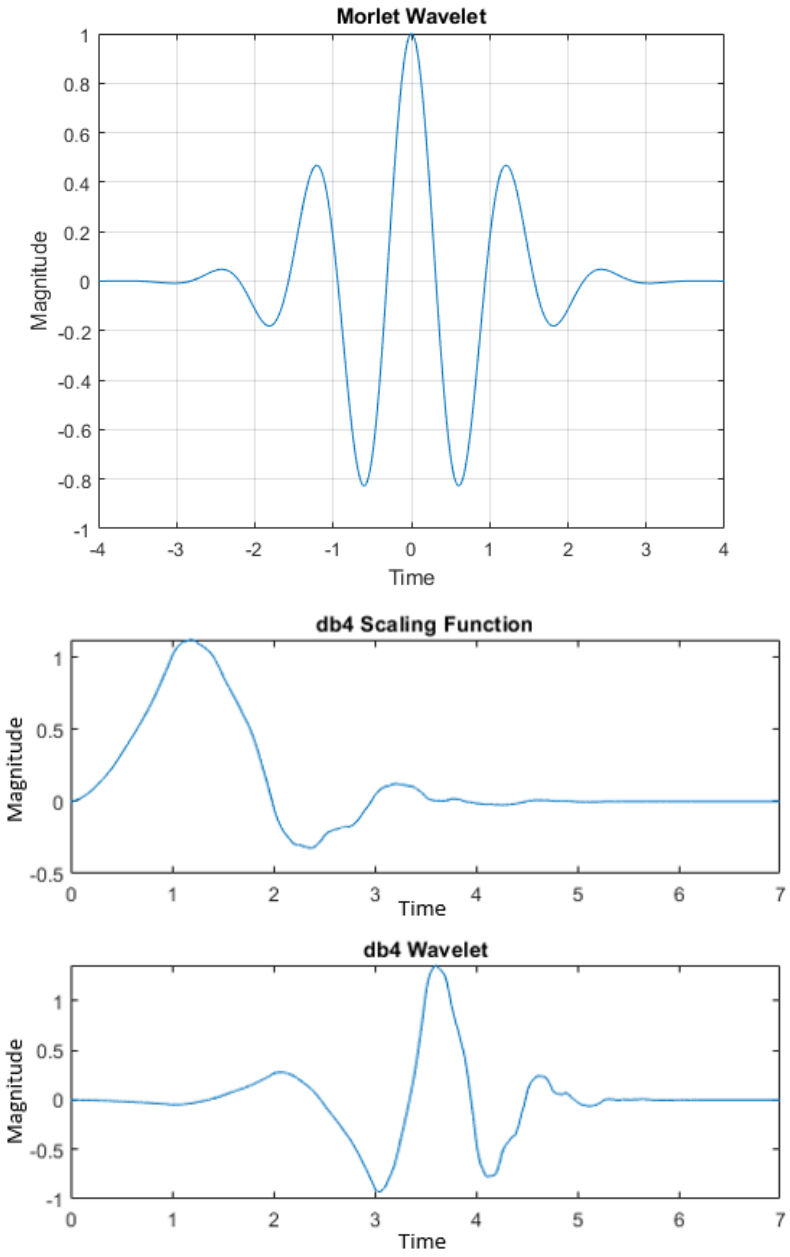

Figure 4.7: Types of Mother wavelets: Morlet (Top) and Daubechies with 4 vanishing moments (Bottom)

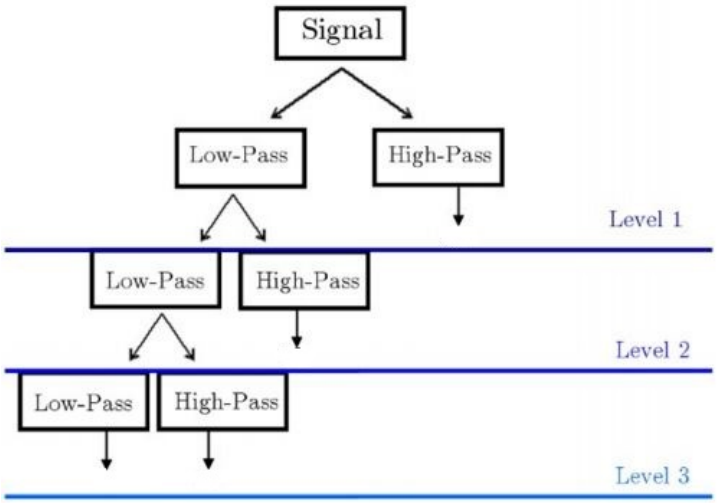

Figure 4.8: Discrete Wavelet Transform of a signal [5]

can observe that this particular signal stores all of its pertinent information using the detail coefficients.

In literature, it has been stated that a major advantage of analyzing a signal with wavelets is that it allows for the study of signal features locally with a detail matched to their scale. This property is especially useful for signals that are non-stationary, have short-lived transient components, have features at different scales or have singularities, discontinuities in higher derivatives and self-similarity [113].

In fact, DWT is used in extracting the characteristic absorption signatures of materials from terahertz reflection spectra [114]. Different mother wavelets were compared based on their phase and gain functions. Phase functions of the wavelet and scaling filters result in spectral shifts to the absorption lines in the wavelet domain. As a result, DWT analysis with accompanying phase corrections can be utilized as a robust technique for material identification in nondestructive evaluation using terahertz spectroscopy [115]. Another application of wavelets is in the implementation

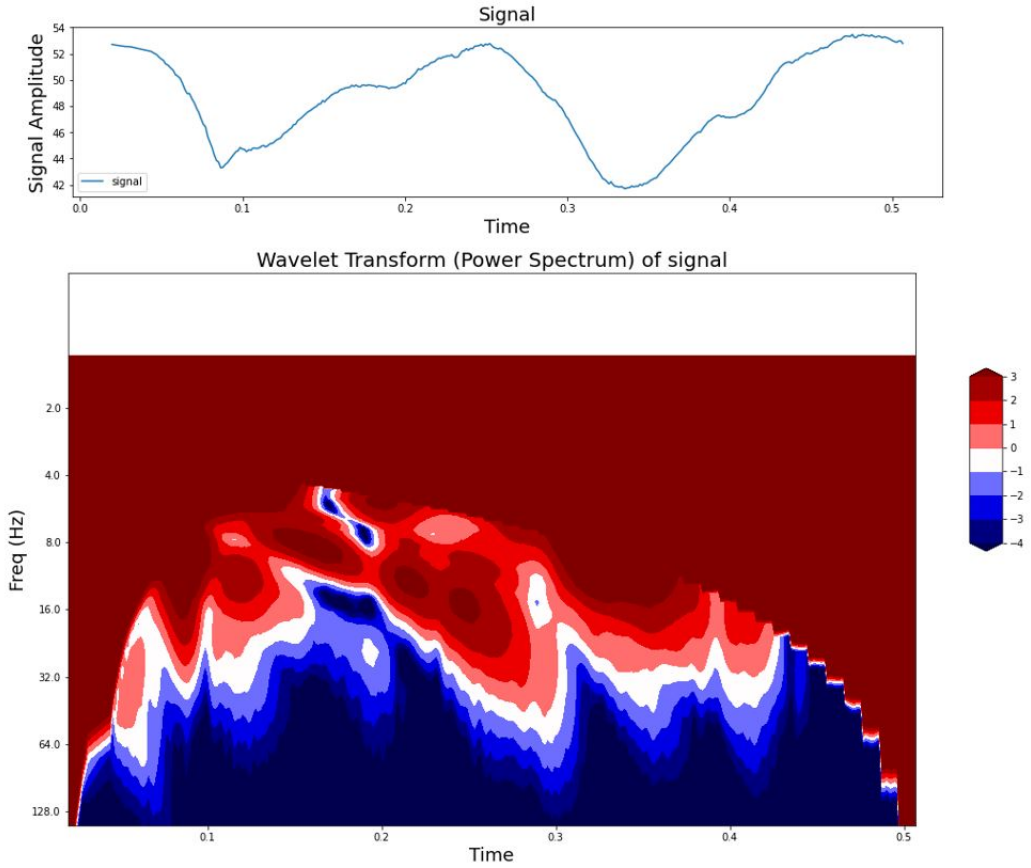

Figure 4.9: Light curve of Rocket nose cone (Top) and its spectrogram (Bottom)

of P300 Speller. P300 Speller is a P300-based Brain-Computer Interface (BCI), which helps users write the desired characters to the computer screen by detecting the P300 event-related potentials in users' electroencephalographic (EEG) [116]. It combines the use of DWT with the Fisher criterion, which is analogous to the F-statistic and is discussed below.

The F-statistic is employed in order to select between the spectral coefficients from the DWT.

$$F = \frac{variance\ of\ the\ group\ means}{mean\ of\ the\ variances\ within\ group} \tag{4.11}$$

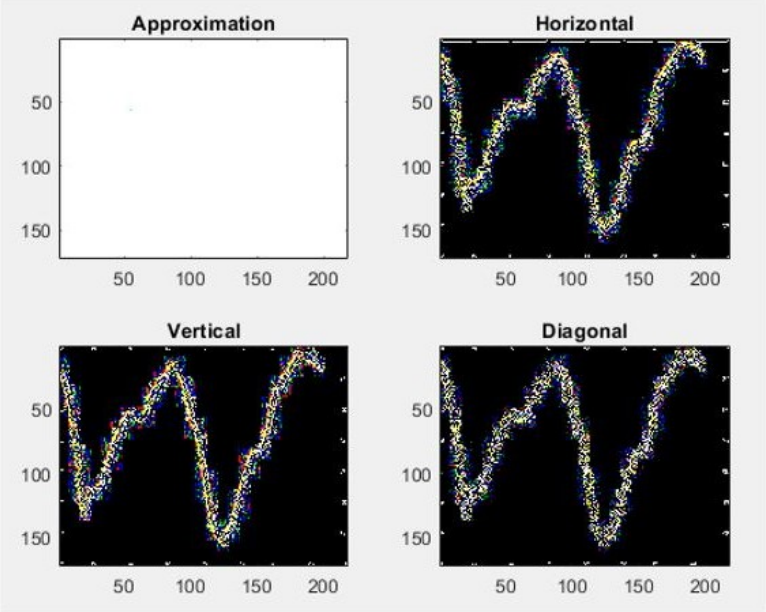

Figure 4.10: Approximation and Detail coefficients of Rocket nose cone signal

ANOVA (ANalysis Of VAriance) is a statistical technique for comparing means of multiple groups under the null hypothesis that all means are equal. If a coefficient scores a high F value, data from the different time-series classes in terms of this coefficient can be easily separated by the classifier. All spectral coefficients are ranked according to their F values and a small set of them are selected to be the classification features.

4.5 Light curve simulation environment

There are several variables that can affect the motion of an object tumbling in space and subsequently alters the amount of brightness detected by the observer. They have been discussed in detail below with considerations for inclusion in the simulation environment based on their significance.

4.5.1 Atmospheric Scintillation

Another variable to consider is the exposure times between frame captures for objects that are farther away and tumbling at a slower rate. Exposure leads to a good signal-to-noise ratio. Atmospheric scintillation is caused by optical turbulence in the Earth's atmosphere [117]. Scintillation provides a limit to the noise performance which can be reached in ground-based photometry. Conventional results for the scintillation level have typically assumed that one object is observed at a time, and we might expect that some of the scintillation would be cancelled out in CCD photometry due to the availability of simultaneous observations of comparison objects [118]. The typical expression used for approximation from [119] is

$$\frac{\sigma_{\text{scint}}}{F} \approx 0.09 \frac{X^{3/2}}{D^{2/3}\sqrt{2T}} \exp\left(-\frac{h}{h_0}\right) \tag{4.12}$$

where σ_{scint} is the rms scintillation (in flux units), F is the object flux, X is the airmass, D is the telescope aperture in cm, T is the exposure time in sec, h is the telescope altitude, and h_0 is a turbulence weighted atmospheric altitude ($h_0 = 8$ km).

Scintillation is negligible compared to the dominant noise sources in the data and the processing of images commences after all images are captured (with corresponding time stamps) and stored.

4.5.2 Orbital evolution

For a spherical body with uniform reflection properties, its attitude motion does not have any effect on the orbital evolution [120]. In contrast, a non-spherical body consisting of flat surfaces does have an effect. Direct solar radiation pressure is by far the largest perturbation and it depends on the current area and its orientation exposed to the radiation source [121]. The observer's capture times for these artificial

objects are generally short bursts in the simulation so any orbital evolution will be minimally visible.

4.5.3 Atmospheric drag

Atmospheric drag is strongly reduced at higher altitudes [122] however, LEO is within the range that experiences the perturbation. Atmospheric drag in LEO is not sufficient to prevent a runaway growth of debris objects [4]. To simulate the influence of atmospheric drag, the aerodynamic force and torque coefficients are calculated for the stream facing side of the spacecraft using the spacecraft surface geometry model and including shadowing effects resulting from the objects actual attitude [123]. This might need prior information on the shape of the object as we use the projected area, therefore taking the dot product of every facet's normal vector and velocity vector. An alternative is to consider the bounds of projected area to compute drag for the unresolved object.

4.5.4 Motion blur

In order to imitate real light curves, the object must continue to rotate during the exposure as it does in the real world. However, for objects that are rapidly rotating or for simulations involving long exposures, the change in orientation of the normal vectors during exposure affects the intensity of the light reflected towards the observer [14]. The apparent streaks, if any, are usually visible on images captured of the object and can cause differences in the peak magnitudes. Since we are dealing with the post-processed brightness intensity values, this is not applicable.

4.5.5 Earth eclipse shadowing

There are instances when the Earth creates a shadow, assuming a perfectly cylindrical shadow cone. It is assumed that Earth shadow is entered, if the angle β between the geocentric unit vector to the sun and the orbital plane of the eclipse is smaller than

$$\beta < \arcsin\left(\frac{a\oplus}{a}\right) \tag{4.13}$$

where $a\oplus$ is the mean Earth radius (6378 km) and a the semi-major axis of a circular satellite orbit [120]. This shadow cylinder is derived under multiple assumptions: 1. a spherical Earth, 2. Earth's atmosphere is neglected. This simple model has been proven useful in many applications with low area-to-mass ratio objects [120].

4.5.6 Self-shadowing and Self-obscuration

Self-shadowing will allow for the simulation of more realistic light curves for convex objects and objects with large extrusions (i.e. solar panels) [14]. Significant portions of the satellite may be shadowed by the solar panel or the body of the satellite may prevent reflections from the solar panel from reaching the observer. This can be emulated using a simple ray-tracing algorithm to determine shadows, where the forward and backward paths of the photons are traced when rendering the image of an object. It's important to note that this does not include secondary reflections. Self-obscuration occurs when other surfaces of the same object cause obscuring. Knowledge of the surface models is the most valuable information needed to solve obscuration problems [124], which is not always the case for unresolved objects.

Otherwise, existence of other objects in near proximity must be evident which is also difficult.

4.6 Model and Results

The overall decision-making flow chart is shown in Figure 4.11 encompassing all the tests, given an object's light curve as the input.

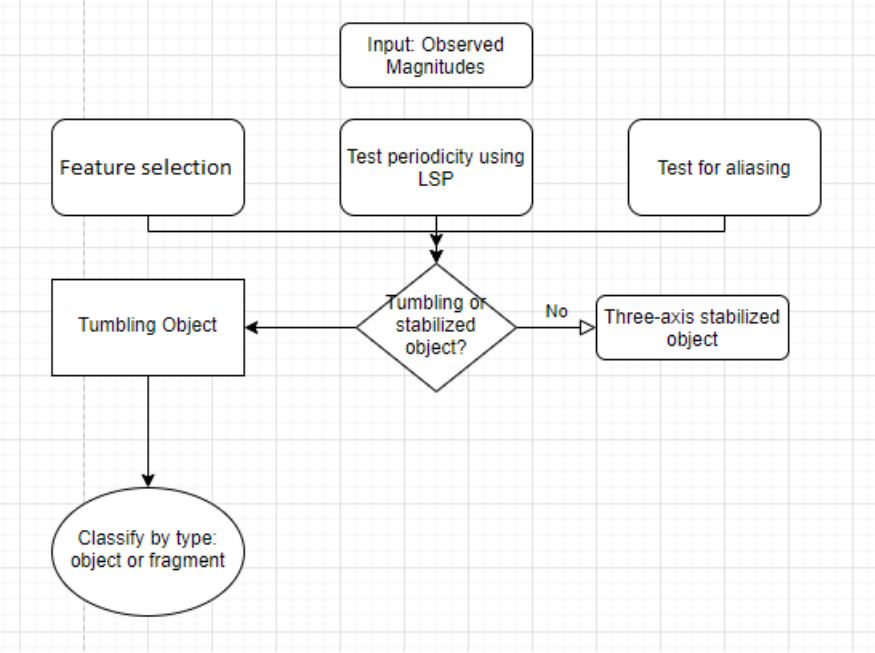

Figure 4.11: Classification flow-diagram

One additional measure to simplify the classification process is the use of a pre-selection tool. For this study, light curve pre-selection tool (lcps) like [125] is chosen. Its main purpose is to restrict large sets of light curves to a number of files that show interesting behavior, such as drops in flux. It uses a sliding window technique to compare a section of flux time series with its surroundings. A dip is detected if the flux within the window is lower than a threshold fraction of the surrounding fluxes.

The training dataset consists of light curve vectors as inputs and class vectors as outputs. The model is trained to assign each measurement vector to a class using a set of training examples. The classification approach is tested using simulated data as well. Synthesizing light curves for each of the models in the bank using Lebedev quadrature at differing angular rotation speeds (from $\omega = 1$ to $\omega = 20\,\mathrm{deg}/s$) for revolutions about its own spin axis makes up a portion of the volume of the training dataset. Variations in viewing geometries, altering size dimensions and interpolated surface reflectance properties across the facets also populate the training dataset. Python and Matlab are used to create the simulation for classification and pre-classification testing (aliasing, periodicity) respectively. In conjunction with the software tools, we used Keras, a deep learning API written in Python, as a library for building the neural network. Python modules for machine learning were utilized to implement the HMM. Populating the datasets was achieved through Matlab as well.

The simulation parameters used to generate the light curve measurements have been detailed in the previous chapters. The position of the object with respect to the observer's location on earth has coordinates to approximate an altitude of 1000 km. The spin-axis orientation is user-defined. A few examples of the simulated light curves are included in Fig. 4.12.

The various layers in the first classification stage using LSTM RNN is visualized in Figure 4.13. The LSTM hidden layers uses a softmax activation function and the dense layer was given a rectified linear activation function. When compiling the network, a categorical cross-entropy loss was used for classification.

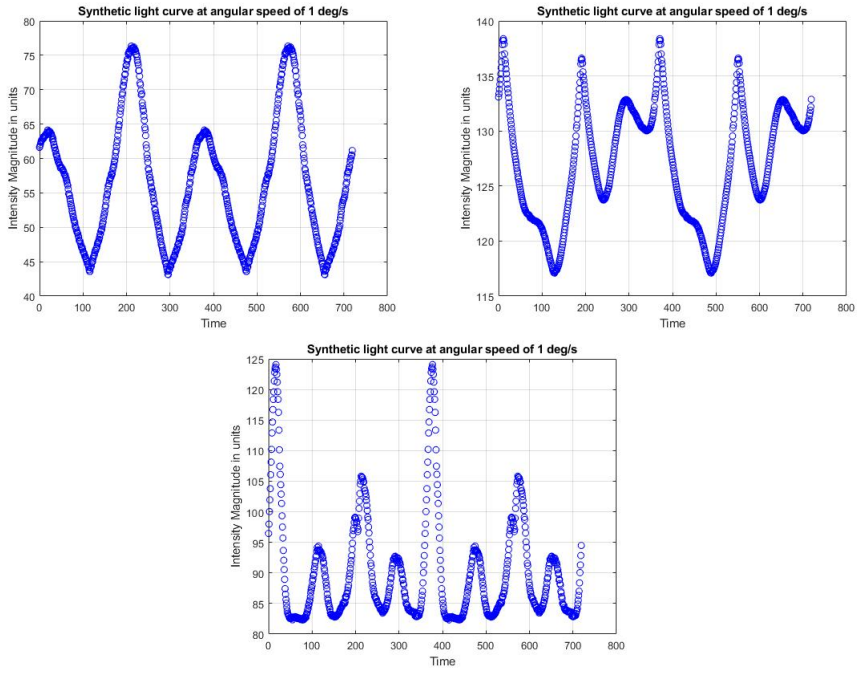

Figure 4.12: Synthetic light curves of Disk, RASSOR drum and Pioneer probe for training data set (Top to Bottom)

Figure 4.13: LSTM layers

Subsequently, the confusion matrix resulting from this is seen in Fig. 4.14. The matrix is usually split into four quadrants where the top-left indicates true positives (TP), the top-right is false positives (FP), bottom-left is false negatives (FN), and the bottom-right is true negatives (TN). One can observe that the range of normalized values is below 18%.

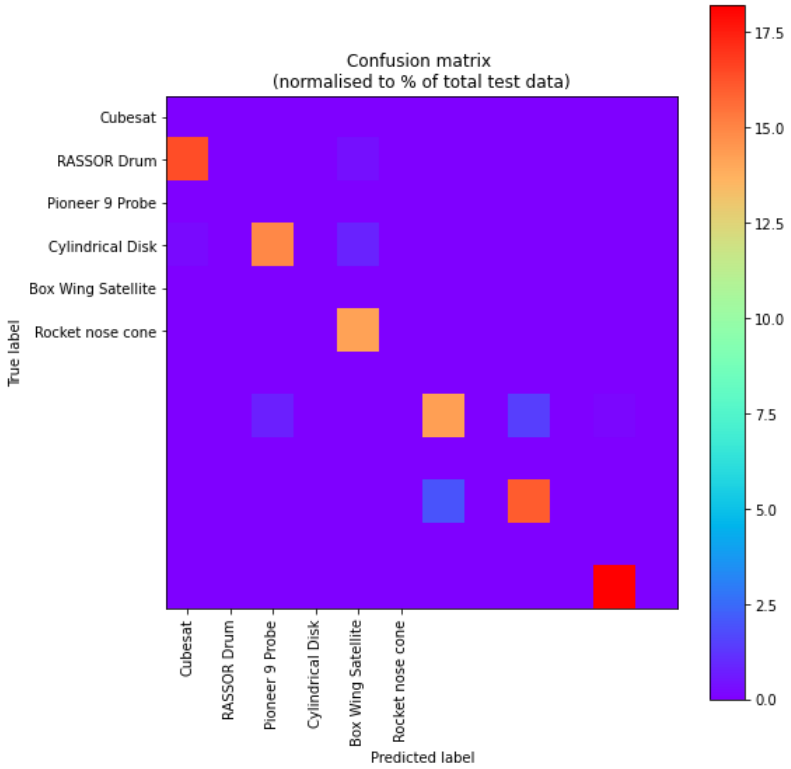

Figure 4.14: Confusion matrix

The state space for the Markov chain is $\boldsymbol{S} = \{S, T\}$ where S represents stable and T represents tumbling RSOs. For the HMM, we assumed the initial probabilities are equal for both states giving $P(X_1 = S) = P(X_1 = T) = 0.5$, which forms our initial state matrix, $\boldsymbol{\pi}$. This means it is equally likely that the first time series came from a stable or a tumbling object. The transition matrix contains the probabilities

that the underlying Markov sequence transitions from one state to another. We will assume the object is likely to stay in its stable state, unless it begins tumbling, in which case, it will very likely stay tumbling. This gives us the transition matrix, $\boldsymbol{A}$:

$$\boldsymbol{P} = \begin{bmatrix} P(S \mid S) & P(T \mid S) \\ P(S \mid T) & P(T \mid T) \end{bmatrix} = \begin{bmatrix} 0.9 & 0.1 \\ 0.01 & 0.99 \end{bmatrix} \tag{4.14}$$

where the notation $P(S \mid T)$ means the probability that the current state is S, given that the previous state was T. Finally, the emission matrix contains the probabilities of each possible observable, for each state. The results from testing the integrated classification model are shown below.

After running 100 epochs, the resulting accuracy is 94%, which is an acceptable value as it is within a 10% error. The higher the number of epochs, the accuracy in turn increases. A comprehensive visual depicting the accuracy in training and validation is observed in Fig. 4.15.

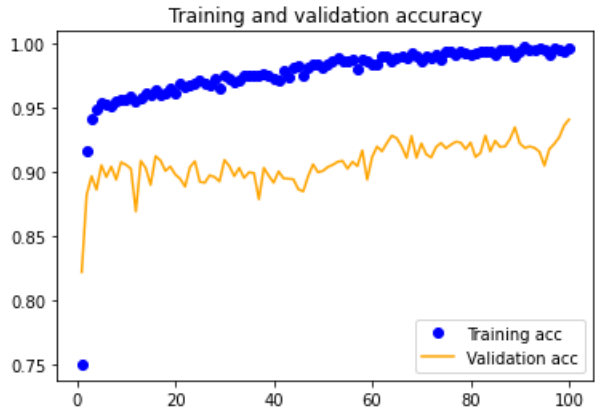

Figure 4.15: Training and Validation accuracy plots

Using a selective, smaller set of synthesized light curves of the artificial objects from the bank of models for the testing dataset, we can observe the results of the predictions using six classifiers of the tumbling state in Fig. 4.16. The blue line indicates the true labels while the red line refers to the predicted labels.

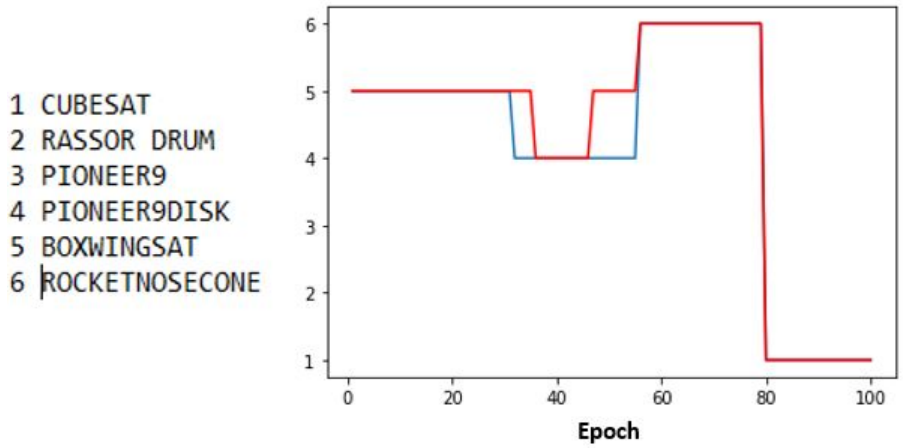

Figure 4.16: Prediction results using test data

It is reassuring to note that the true and predicted values overlap for most of the test data with some inaccuracy between the Pioneer 9 disk and the box wing satellite. There are some instances where the model was able to identify the two, however the error can be a result of the similarities in the light curves of the two objects. The model can also distinguish the cubesat from the rocket nose cone as the complexity of the latter is greater. These results are from an ideal model and to ensure that it is robust and can operate at any threshold, we performed some uncertainty analysis.

4.6.1 Uncertainty in the model

Modeling uncertainty in a neural network utilize various methods such as Monte Carlo simulation [126], Bayesian neural network [127], dropouts between layers [128].

Table 4.2: Accuracy of the model from varying levels of dropout

Dropout Level (%)	Accuracy (%)
0	92.16
25	93.32
50	91.28

Since dropout layers are included in the LSTM RNN, it has been chosen for this purpose. Dropout is a technique used to avoid overfitting and the % rate of dropout is used to remove hidden neurons in the layers. We can also add stochastic noise on model weights of the neurons. This is performed using Gaussian noise with a mean value and fixed standard deviation/percentage on weights. The results from finding the optimal tuning parameters for this hybrid model with input noise is tabulated below in Table 4.2.

It is inadequate to dropout more than 50% as it may become a scenario of underfitting. Therefore, the testing was bounded to that value. The optimal dropout level is at 25% resulting in the highest accuracy of predictions, although by a minimal amount. Another aspect that was considered is noise regularization and this was done by injecting Gaussian noise ($\mu = 0, \sigma = 0.1$) between hidden layers, specifically before the ReLU activation function. This resulted in an accuracy of 92.4% conjoining it with the optimal dropout level. It was evident that adding noise after the activation function creates a noisy activation function. However, the disadvantage to it is that results may be out of range from what the activation function may normally provide [129].

Now that the model had noise, we also introduced noise in the test data to investigate the behavior of the model in handling increased uncertainty. Adding a percentage of peak-to-peak amplitude to the signal as noise will alter the input test data. The results from combinations of model and test data uncertainty are tabulated

in Table 4.6.1, where revised model indicates optimal tuning for dropout layer and noise regularization. The three scenarios that were executed are listed below:

1. Revised model and test data without noise
2. Original model and test data with noise
3. Revised model and test data with noise

Table 4.3: Table of predictions and accuracy of model based on varying conditions of uncertainty in the model and test data

Scenario	Accuracy (%)	Plot of predictions
1	90.74	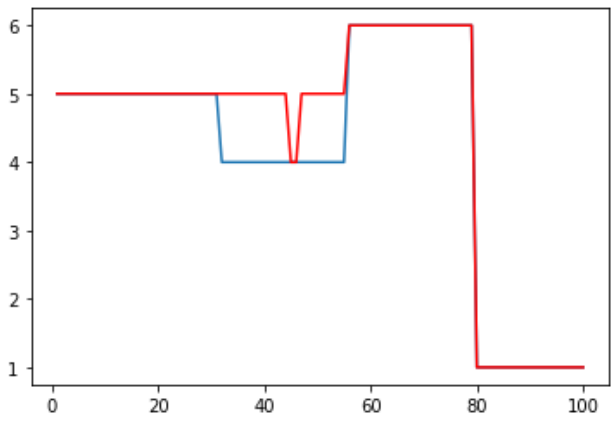
2	91.31	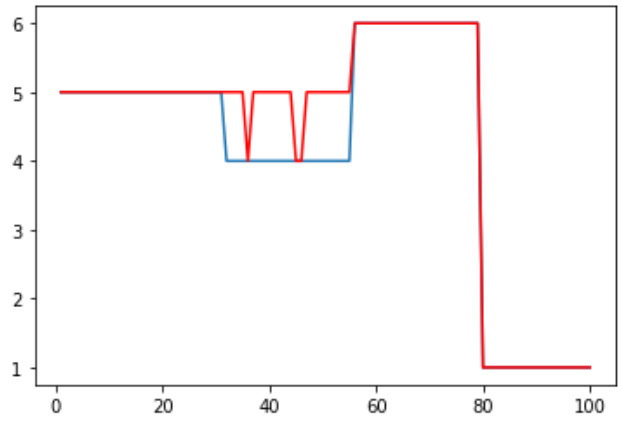

3	91.82	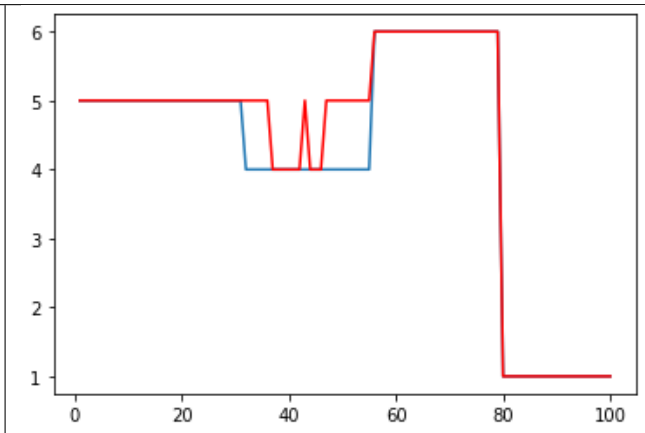

As mentioned earlier, the plots show the predictions for the classifiers in the test data. Surprisingly, scenario 3 (revised model and test data with noise) resulted in the highest accuracy and the least variation between expected and predicted classification. However, the other two test conditions don't fall behind and still lie in the 10% error bound. As expected, after introducing uncertainty in the model and injecting noise to the input test data, the accuracy has decreased from the original model by about 3%. However the small drop verifies and validates the robustness of this model in handling uncertainty.

4.7 Future work

Incorporating real light curves in our test dataset observed from Mini-MegaTORTORA (MMT-9) multi-channel high temporal resolution telescope was not feasible. Real light curves are typically short bursts of duration and do not match the length of simulated data. Within a single object's light curves, there are large variations in the trends and the periodicity. This is because several users from different locations are collecting data and there is a bit of discrepancy in the archive as some deem

an object periodic, while others aperiodic. Another thing to note with real data is that photometric observations with a gap in collection time can possess changes like slowing of tumbling rate. Here, it is important to use key identifiers in the light curve to match for resemblance. However, if the period is similar, we can correlate them to be the same object regardless of the gap in collection. If a component breaks off, resulting in lost mass, we can classify this as a new object. The predicted classes will provide us with confidence levels of multiple models and this is a way to approach this problem.

Sample selection bias is also a parameter to remember. It can cause catastrophic errors in predictions on the testing data because standard assumptions for machine-learned model selection procedures break down, and dense regions of testing space might be completely devoid of training data [130]. Some remedies include importance weighting, co-training, and active learning (AL). AL is where the data, whose inclusion in the training set would most improve predictions on the testing set, are queried for manual follow-up [130]. This is an effective approach and is appropriate for many astronomical applications (i.e. stars), although quite tedious and requires additional user interference. This technique needs to be verified for artificial RSOs, else another process to rectify sample selection bias is required.

Chapter 5

Modeling Triton's atmosphere

Triton, Neptune's largest moon and the only moon in the Solar System to be retrograde (orbit in an opposite direction to its planet), is thought to originally be a Kuiper Belt Object (KBO) [131]. The Kuiper belt extends outward from the orbit of Neptune, and is several manifolds wider and massive than the asteroid belt. Due to the nature of Triton's retrograde orbit, it is possible that Triton was a separate body originating from outside of our Solar System that was captured by Neptune's sphere of influence. Triton's surface and atmosphere still remain an enigma due to its history of hydrocarbons and tidal dissipation [131]. The possibility of a subsurface ocean indicates dynamic geologic activity and a better understanding of Triton can uncover the secrets behind the evolution of icy objects in the Solar System, including large moons, small KBOs and dwarf planets such as Pluto that might share a similar history.

Triton's surface is a mixture of smooth plains adjacent to craters that may have been caused by collisions with inner satellites post-capture by Neptune. Since Voyager 2 in August 1989 showing data of a dynamic atmosphere, only ground telescopes were able to capture data on Triton. Voyager observations of dust streaks imply the presence of strong surface winds in Triton's lower atmosphere [132]. However, cloud motions at different altitudes show velocities in different directions. The driving-energy behind the winds stems from maintaining vapour-pressure equilibrium of nitrogen (predominant constituent) with surface frosts and varied solar heating of the surface [132].

In addition to Voyager 2, the more recent New Horizons spacecraft (whose goal was to explore Pluto and other Kuiper Belt objects) performed a distant flyby of Neptune in 2014. During this flyby, New Horizons took a few snapshots of Neptune and Triton. Following analysis led to scientists suggesting that Triton could share similarities to Pluto: an icy surface, bright poles, nitrogen atmosphere, and the presence of 'ice volcanoes'. Another recognizable feature is Triton's size (only slightly larger than Pluto in terms of diameter).

Given the current state of knowledge of Triton's atmosphere, we need to probe Triton's atmosphere in the microbar region where previous observations do not exist and compare with model predictions. The seasonal change also needs to be investigated, which was predicted [133] based on vapor-pressure equilibrium of Triton's atmosphere with surface ices. High-resolution information about the atmospheric structure is required and this is acquired currently using ground-based observations of a series of stellar occulations (occurs when light from a star is blocked by another body from reaching the observer). An example of such was performed in 1993 at the Kuiper Airborne Observatory of the star Tr60 [133] by Triton.

Ground-based observations are confirmed since the rotation period and pole that it rotates about are known for Triton. Past literature has attempted to model the atmospheric figure by probing Triton's atmosphere with a stellar occultation. The observations of the occultation has occurred from a group of sites that span the full atmosphere (at 100 km altitude) or from one or more sites (at 20 km altitude) that passes near the center of Triton's shadow and model the structure of the 'central flash', similar to the approach for Titan [132]. To observe the changes in atmosphere with time, light curves can be gathered within the central region in order to understand the structure.

To quantify the distortion required to reproduce the measured light curve, an elliptical model of the atmosphere of varying ellipticity (circular, prolate and oblate) can be constructed and fit using the least-squares method. The orientation of the ellipse is variable. Instead of using a single probe approach as in the past, we can use the operations concept of a space probe releasing hundreds of small satellites into orbit [134] around Triton in succession (with a time delay) to improve data collection capability and provide redundancy due to power constraints. This allows for an in-situ, simultaneous measurements in the light curves, impossible to achieve using one operating probe. The data collected through a simulation (with additional astrometric data of Triton) can be 3D mapped to generate the atmospheric model and validate predictions of expansions of Triton's atmosphere due to thermal properties of the surface and increase in pressure [132].

This chapter will include a background on Triton, stellar occultation process, mission planning to arrive at Triton, and use of a constellation of satellites.

5.1 Triton

Triton has an unusual, circular, and close to Neptune orbit, but highly inclined to the planet's equator (by 157°) [135]. It has a sparse nitrogen-rich atmosphere with trace amounts of carbon monoxide and small amounts of methane near the surface [136]. Triton has a thin atmosphere and the absence of oceans. However, Earth and Triton share some contributing factors to global warming, such as the amount of methane and carbon monoxide in the atmosphere. Triton is a unique example of a vapor pressure atmosphere; this leads to a uniform global surface temperature and uniform near surface atmospheric pressure [136].

Triton is a relatively large moon (1352 km in radius) and it's distance from the Sun (30 AU), makes it's surface a very cold place (38 K). Yet, despite these frigid

surface conditions, Voyager 2 discovered it has a thin atmospheric surface pressure (14 μbar), where 1 bar is the approximate surface pressure of Earth's atmosphere [135]. Earth and Triton are similar in their atmospheric composition, with a majority of Nitrogen gas. The troposphere has shown winds as high as 8 km. [136] We know that the acceleration due to gravity on Triton's surface is 0.779 m/s^2 so using the same gravity model as before, we can compute the gravitational constant to be $\mu_0 = 1426.89\ km^3/s^2$. Since we know the surface temperature and atmospheric pressure on Triton, we can use the ideal gas law (as an approximation) $\rho = \frac{P}{R_g T}$ where R_g is the gas constant equal to 287.05 $J/(kg\ K)$ to calculate the surface air density ($\rho_0 = 1.2784 \times 10^{-4}\ kg/m^3$). The density model is not an exponential function like Earth. Instead, we use the electron density concentrations of the atmospheric composition from Voyager measurements [137] to produce a lookup table of densities for varying altitudes. In order to develop the atmospheric density model, it is crucial to comprehend the composition, structural layers and geologic features of Triton.

Nitrogen is the main gas in Triton's atmosphere [138]. The two other known components are methane and carbon monoxide, whose abundances are a few hundredths of a percent of that of the nitrogen. Carbon monoxide, which was discovered only in 2010 by the ground-based observations, is slightly more abundant than methane. Since 1986, the abundance of methane relative to nitrogen increased by four to five times due to the seasonal warming [139].

There is a possible existence of argon and neon lower than a few percent, although they were not detected in the ultraviolet part of the spectrum of Triton obtained by Voyager 2 in 1989 [137]. In addition to the gases mentioned above, the upper atmosphere contains significant amounts of both molecular and atomic hydrogen, which is produced by the photolysis of methane. This hydrogen quickly escapes into space serving as a source of plasma in the magnetosphere of Neptune [137].

Convection near Triton's surface heated by the Sun creates a troposphere rising to an altitude of about 8 km. Temperature decreases with height reaching a minimum of about 36 K at the tropopause [140]. There is no stratosphere, unlike Earth [135]. Higher altitudes include the thermosphere (8 to 850 km) and exosphere (above 850 km) [141]. In the thermosphere, the temperature rises to a constant 95 K upwards of 300 km [137]. The upper atmosphere continuously leaks nitrogen into outer space due to the weak gravity of Triton at a loss rate of about 0.3 kg/s. However, evidence shows that it is being replenished due to several geyser-like volcanic vents that were apparently spewing nitrogen gas laced with extremely fine, dark particles that settle onto the surface.

Taking into consideration the various factors that comprise Triton's atmosphere, a comprehensive density model has been developed (Figure 5.1) using data obtained from Voyager [137] as well as conversion factors from molecular to mass weights. A portion of the atmospheric measurements ($altitude \geq 400\ km$) indicated isothermal activity and the exponential relationship in adherence to it was utilized for the density model.

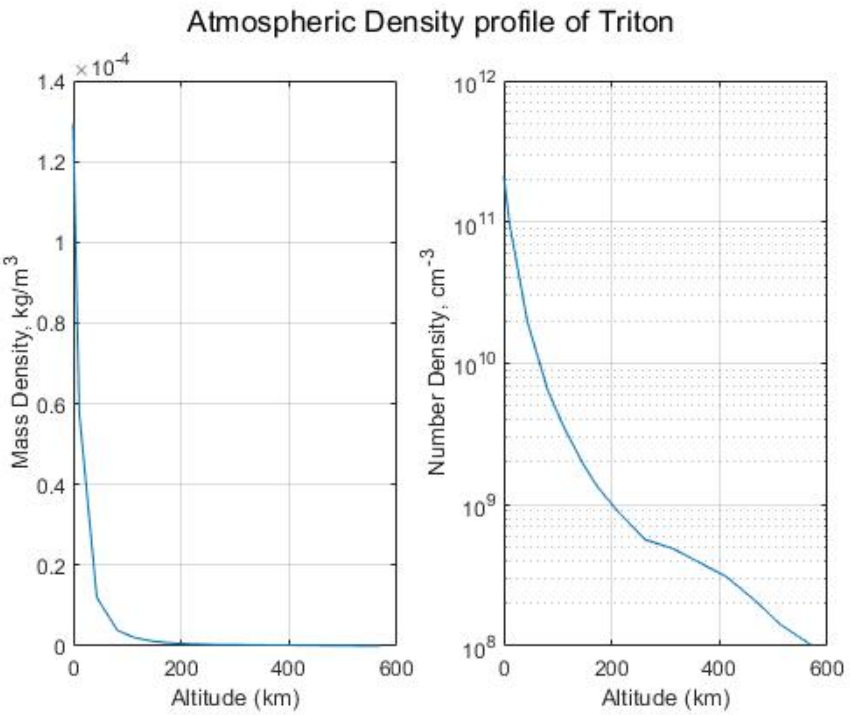

Figure 5.1: Atmospheric density profile for Triton as a function of altitude, Left: Mass density, Right: Electron number density

5.2 Stellar occultation process

There are two optical ways to study the atmosphere of a planet without landing and taking measurements. The first method is to look directly and the planetary disk and observe reflected sunlight. The alternative is to observe light from a distant star or the Sun which has passed at grazing incidence through the atmosphere. The latter process is known as the stellar occultation process. This method is valuable in giving information directly about the vertical structure of the atmosphere, its pressure, its temperature and perhaps its cloud or dust content.

The process as formulated by [142, 143] is as follows. Given the configuration of source (star), planetary body (Triton), and observer (on Earth), and an assumed set of parameters for the structure of the planetary atmosphere, the light curve can

be computed as follows. First, considering that the atmosphere acts only through its refractivity, we need to find the path through the atmosphere of the ray from source to observer and compute the extinction due to differential refraction. Next, we compute the reduced path length and multiply it by the sum of coefficients of absorption due to Rayleigh scattering, molecular absorption and absorption by clouds, dust and haze to get the optical thickness, τ. Multiplying the intensity reduction due to differential refraction by the factor of $(e^{-\tau})$ can result in overall extinction. A visual representation of the star path (Fig. 5.2 from [144]) and stellar occultation process by a planetary atmosphere (Fig. 5.3 from [144]) is included for reader's convenience.

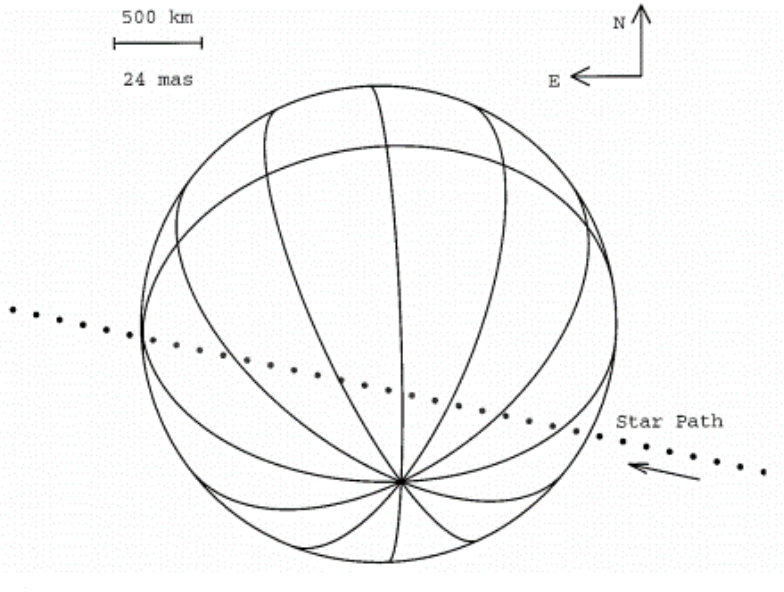

Figure 5.2: Star path at time intervals as it is occulted by Triton. The unit scale is at 24 milliarcsec.

A few approximations are made when computing light curves: geometric, atmospheric, and about the process.

1. The Sun is sufficiently distant that its light may be considered a plane wave.
2. Triton is a sphere of radius r.

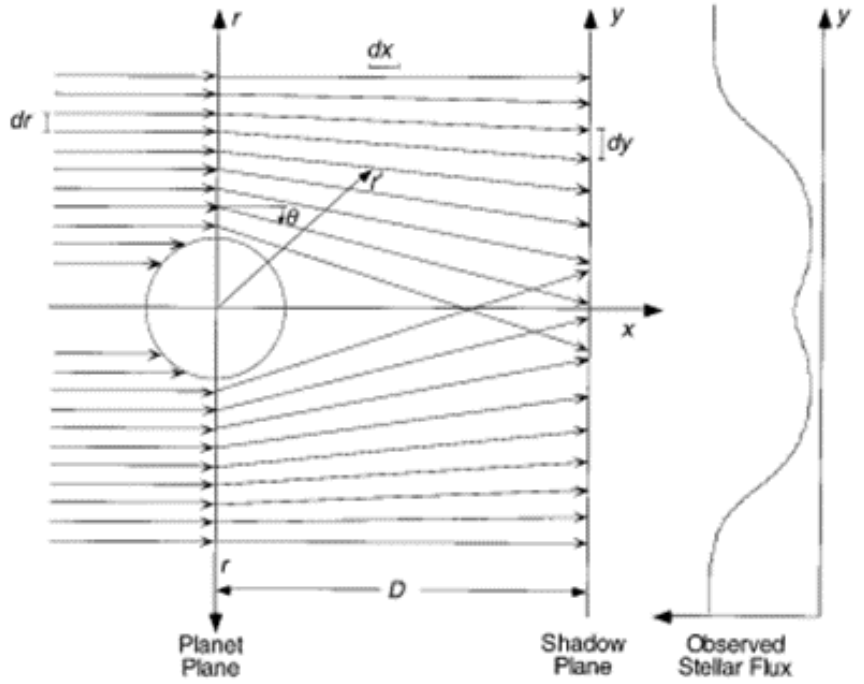

Figure 5.3: Stellar occultation by a planetary atmosphere: Light from a star is refracted by a planetary atmosphere and is dispersed. The dimmed magnitude is observed in the shadow plane. The sum of all flux at the observer's location is mapped as the occultation light curve seen on the right.

3. The radius of Triton is much greater than any characteristic height in the atmosphere.
4. Triton's atmosphere might not be spherically symmetric, and all quantities depend only on the radius, r.
5. The atmosphere is transparent (no haze present).
6. It is not purely molecular nitrogen N_2 atmosphere; includes other minor species like methane.
7. $T(r)$, temperature, is time-independent.
8. The refractivity of the atmosphere at any point is small.
9. The change in temperature is small over an altitude difference of one scale height.

10. Multiple scattering is negligible

Effects of refraction [142, 145] such as variation of refractivity with height, path of the ray, differential refraction, and the effects of absorption and scattering [142] such as reduced path length, Rayleigh scattering, molecular absorption and absorption by haze, clouds and dust can significantly influence the data collection and analysis. Thin atmospheres act as poor lenses and the Fresnel and Fraunhofer regimes need to be taken into consideration in the stellar occultation process [146]. Assuming that the Sun is finite, limb darkening [142] is significant during eclipses and must be accounted for.

Results from the 1993, and 1995 occultations have given us astrometric solutions and one such measured light curve is visible in Fig. 5.4 (from [144]).

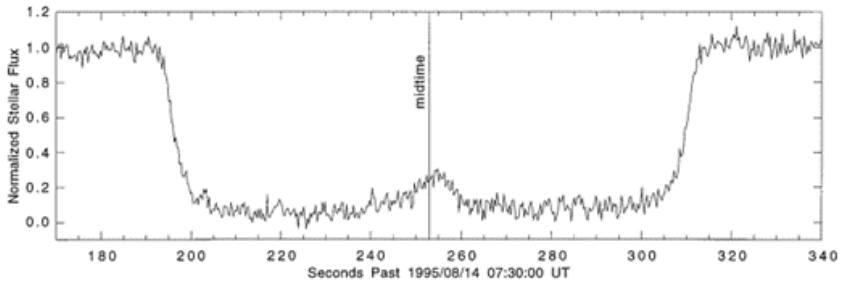

Figure 5.4: Stellar occultation light curve showing brightness measurements as a function of time. The peak of the central flash is seen slight to the right of midtime line.

5.3 Atmospheric information from occultation data

To understand the atmosphere from stellar occultation light curves requires a geometric reconstruction of the path of the observer through the shadow plane. For this, we will model an elliptical planetary figure from several chords of known relative positions [147], but this task can also be carried out from accurate astrometric

measurements of the star and Triton [148]. Once the shadow-plane path has been established, the first information that we can extract is the scale height, regardless of knowledge of Triton's atmospheric composition. In this case, since the composition is known, the temperature, pressure, and number-density profiles can be derived. Local variations in number density due to atmospheric waves and/or turbulence, which cause spikes in the occultation light curves, can also be characterized [143]. From stellar-occultation probes at multiple latitudes, the ellipticity of an atmosphere can be determined. For certain cases, information about the composition of an atmosphere can also be revealed through the time delay of spikes in dual-wavelength observations [143].

Our aim is to determine a unique global model (with atmospheric profiles for scale height, density, temperature and pressure) that satisfactorily explains all the observations, and to accomplish this, we can use chi-squared per degree of freedom term [149] to check for quality. The light curves from a best-fitting atmospheric model must resemble Fig. 5.4. The iterative procedure, combining both direct ray-tracing and inversion approaches [150] to find the model is to:

1. Invert best signal-to-noise ratio (S/N) light curve to retrieve atmospheric density, pressure, and temperature profiles.
2. Through direct ray-tracing, synthetic occultation light curves that are simultaneously fitted to all of the observed light curves obtained at a given date.
3. Find location of Triton's shadow center relative to the occultation chords.
4. Inversion of the best light curve is performed again and the procedure is resumed.

5.4 Mission concept of Operations

The spacecraft is propelled into a trajectory towards Saturn, and ultimately, to Triton. The orbiter will carry the small satellites, which will then be deployed in succession to map and study Triton's atmosphere. This will be accomplished using the

various instruments onboard. The orbiter will continuously transmit back to the Deep Space Network on Earth until its end of life. The orbiter will then dispose of itself into a graveyard orbit around Triton and fully abide by the established Planetary Protection Protocol [151].

Launching from Earth (Cape Canaveral, Florida) and getting a boost from the upper stage engine will propel the spacecraft in the direction towards Saturn. Approximately 3 years later, the orbiter will conduct a flyby of Saturn, with a small ΔV burn for course correction towards Neptune. It takes another 10 years to arrive at Neptune and performing a retrograde ΔV burn will place itself in an elliptical orbit around Neptune. When Triton and Neptune align properly, it will perform a Hohmann transfer, to enter a polar parking, circular, polar orbit. Figure 5.5 (from [152]) shows the Neptune capture and Triton transfer orbits in sequential order.

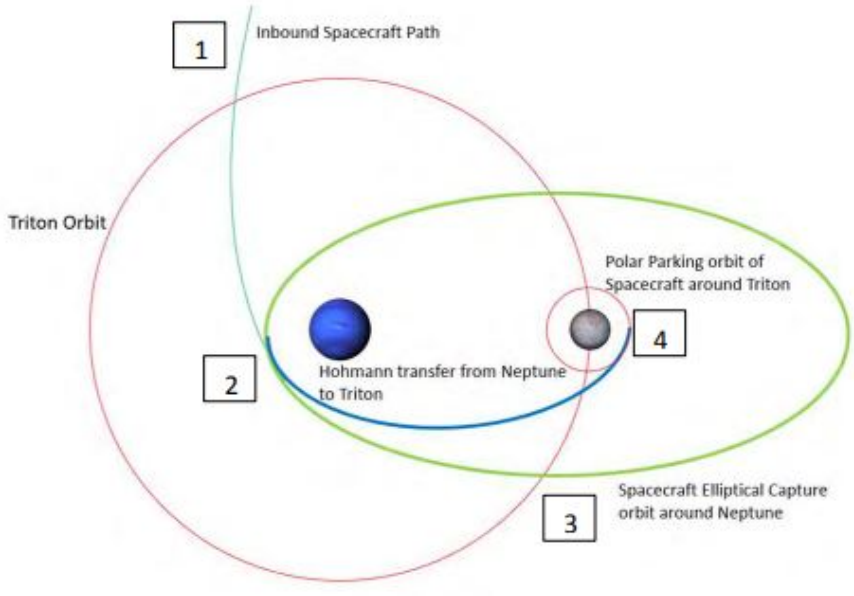

Figure 5.5: Orbits showing Neptune capture and transfer to Triton

The payload instruments include visible (VIS) and ultraviolet (UVS) mapping spectrometers (for the atmosphere and geysers), particle and dust analyzers (trace of the atmosphere), and optionally radio science and magnetometer, and gyroscope. The orbiter has a mass of approximately 25 kg with peak power of 38.5 W [152], whereas the probes should weight less than 1 kg and significantly lower peak power than the orbiter. VIS and UVS operate together in order to analyze the composition, density, and pressure of the atmosphere, and also study the geyser plume material.

The probes can continuously take and transmit all necessary data back to the orbiter when in view for about 1.5 hours per orbit, or until battery power ceases. Another fact to remember is that Triton will be in eclipse for 1 hour, so it will be vital to time the transmission and collection to maximize power.

5.5 Constellation of satellites

The role of the small satellites is to use them as probes. Ideally, we can measure speed and position of a probe in the axis of its descent as it falls through Triton's atmosphere. Apart from gravity, atmospheric drag is an external force acting on the probe and we can compute the acceleration due to drag using equation 5.1

$$\boldsymbol{a}_D = -\frac{1}{2}\left(C_D \frac{A_v(t)}{m_s}\right)\rho v_r^2 \boldsymbol{e}_v \tag{5.1}$$

where C_D is a drag coefficient, $A_v(t)$ is the cross-sectional area of the satellite in direction of travel, m_s is the total spacecraft mass, ρ is atmospheric density, v_r is the velocity magnitude relative to the ambient atmosphere, and $\boldsymbol{e}_v$ is a unit vector in the relative velocity direction.

The inverse ballistic coefficient is the term within parentheses in the equation. We can determine the ballistic coefficient that results in the closest estimation of position

Table 5.1: Diode accuracy at varying levels of temperature

Temperature (K)	Accuracy (mK)
1.4	± 12
10	± 12
77	± 22
300	± 32
500	± 50

and velocity to the truth values. Atmospheric density can then be inferred from this. One such approach for atmospheric density estimation using a satellite constellation [153] is a new spline-based atmospheric density parameterization. Parameterization fits into estimation and does not reduce the resolution of the density approximation. However, it was found that some *a priori* knowledge about density is necessary to reduce uncertainty in estimates. The knowledge about the satellite's inverse ballistic coefficients is of limited use, because the difference in time constants tends to decouple the inverse ballistic coefficients and the density parameters [153]. To solve this problem, a suggested solution is including gyroscopes on the probes, but further analysis and testing is required to verify if this is viable. Since Triton's maximum gravitational acceleration is approximately 0.08 g_0, where g_0 is the gravitational constant on Earth, the sensor's peak acceleration value will be well within the limit.

In order to measure temperature, we can utilize a sensor, Omega CY670 cryogenic temperature diode, as it is accurate within temperature ranges of 1.4 K to 500 K [152]. Triton's ambient temperature is said to be 38 K. The diode's accuracy is listed for the range of operating temperatures in Table 5.1.

Additionally, a pressure transducer can determine the pressure gradient of Triton's atmosphere. As the atmospheric pressure is quite low (14 μbar), the sensor must be capable of reading small measurements. The LP1400 has a range of 10.3 to 68.9 μbar [152]. The structure of the probes must be forward heavy in order to

have projectile motion during descent. Reduced mass materials like Titanium are suitable for this purpose. Since Triton has a surface pressure of 1.4 Pa, multi-layer insulation (MLI) doesn't serve the purpose at $P > 1.33\ Pa$. Instead, aerogel for foam insulation works well with the added benefit of lower density. Choices for the various components of the satellites can optimize the overall performance.

The life cycle for the data collection is limited, hence a constellation of small satellites was chosen to serve this purpose. Releasing multiple probes ensures redundancy and accounts for good measurements if any are lost to malfunction or transmission errors. This technique allows us to deploy several satellites within the same constellation during a single launch, making it cost-effective [154]. It's essential to have correct positioning of the satellites within the constellation.

The results of the atmospheric model after simulating the constellation of satellites is an extensive application that can be explored for future work and improvements.

Chapter 6

Summary and Closing Remarks

Additional artificial space objects orbiting Earth is becoming an issue for space situational awareness (SSA). A piece of space debris too small to be tracked can damage other large structures such as the International Space Station, which is a main hub for operations in space and on Earth. It reminds us that the low-Earth orbit's space junk problem is a time-sensitive issue. Accurate tracking and identification of RSOs through ground-based photometric light curve measurements can aid in characterizing collision-prone objects to our orbital assets, planning for commercial use of space, and possibly understand the intent of foreign objects. Optical measurements for space object tracking are sensitive to shape, attitude, angular velocity, and surface parameters. Current state-of-the-art in RSO characterization relies heavily on nonlinear state estimation theory, multiple models, and full light curve inversion which is computationally expensive. A data-driven approach improves accuracy for a large volume of objects using deep neural networks. Given an unresolved object's light curve, in low earth orbit (LEO), we can now characterize it by shape and spin rate using Recurrent neural networks and a hidden Markov model. This hybrid approach improves the accuracy of time series classification by executing a secondary screening accounting for the temporal relations in the data. Redundancy in the classifiers from multiple layers of training and prediction are eliminated. This integrated model has been developed to identify tumbling and stabilized objects by testing for aliasing, periodicity, and feature extraction. The performance of this approach for RSO classification is demonstrated via simulations. The model is designed to train and

validate using synthetic light curve measurements of objects spanning ellipsoid, rocket upper-stage, CubeSat, disk, probe, and box-wing satellite, among others. Variations from different viewing geometries, altering shape/size dimensions and surface properties have populated the dataset. The simulated measurements are evaluated using Lebedev quadrature at varying angular rotational speeds and interpolated surface reflectance properties across the facets. The fidelity of these simulations ensures it is both realistic and accurate to within 10% error and robust to handle uncertainty. The computational efficiency is increased as function integration has shown better performance compared to tessellation for artificial RSOs. After investigating a wide range of signal processing techniques, the Lomb-Scargle periodogram most accurately estimates the Sidereal rotation period of the object with the least user interface. The dependency on *a priori* knowledge of the object is reduced as we no longer need to follow the established Light curve inversion procedure. There is flexibility to deal with a larger amount of data and populate more datasets for improved artificial RSO classification.

Extensive understanding of photometric light curves reveals the effects of the atmosphere as it can reduce the quality of data collection. This lends to availing ourselves to atmospheric models for future missions that may choose to use light curves. The lack of information about Triton in recent years makes it a plausible site for exploration. This can be fixed using ground-based photometry and some in-situ measurements. A better understanding can open the doors to further exploration of icy objects in the Solar system, including large moons, small Kuiper Belt Objects (KBOs) and dwarf planets that might share a similar history. Continuing this investigation of Triton's atmosphere using stellar occultation will result in a global model. The generated atmospheric model can validate predictions of Triton's expanding atmosphere due to thermal properties of the surface and increase in pressure.

Bibliography

[1] E. O. Ofek, "MATLAB package for astronomy and astrophysics," Astrophysics Source Code Library, 2014.

[2] S. Seth and J. C. Principe, "On speeding up computation in information theoretic learning," in Proceedings of the 2009 International Joint Conference on Neural Networks, IJCNN'09, (Piscataway, NJ, USA), pp. 2471–2475, IEEE Press, 2009.

[3] X. Lu, H. Zhao, and Z. You, "Cellinoid shape model for asteroids," Earth Moon and Planets, vol. 112, pp. 73–87, 08 2014.

[4] E. Schafer, "Stereoscopic light curve analysis of space debris objects," Master's thesis, DLR Institute for Technical Physics, 12 2017.

[5] A. D. Dianetti and J. L. Crassidis, "Light curve analysis using wavelets," in 2018 AIAA Guidance, Navigation, and Control Conference, p. 1605, 2018.

[6] I. W. McQuaid, "Autonomous association of geo RSO observations using deep neural networks," tech. rep., Air Force Institute of Technology, Wright-Patterson Air Force Base, Ohio, 2018.

[7] R. Linares, J. L. Crassidis, and M. K. Jah, "Space object classification and characterization via multiple model adaptive estimation," in 17th International Conference on Information Fusion (FUSION), pp. 1–7, IEEE, 2014.

[8] R. Furfaro, R. Linares, and V. Reddy, "Space objects classification via light-curve measurements: deep convolutional neural networks and model-based transfer learning," in AMOS Technologies Conference, Maui Economic Development Board, 2018.

[9] M. Kaasalainen and J. Torppa, "Optimization methods for asteroid lightcurve

inversion: I. shape determination," Icarus, vol. 153, no. 1, pp. 24 – 36, 2001.

[10] M. Kaasalainen, J. Torppa, and K. Muinonen, "Optimization methods for asteroid lightcurve inversion: II. the complete inverse problem," Icarus, vol. 153, no. 1, pp. 37 – 51, 2001.

[11] E. Antonello, P. Broglia, P. Conconi, and L. Mantegazza, "Fourier decomposition of the light curves of high amplitudes delta scuti and sx phe stars.," Astronomy and Astrophysics, vol. 169, pp. 122–132, nov 1986.

[12] E. Poretti, E. Antonello, and J. F. Le Borgne, "Fourier decomposition of the light curves of pulsating variables : the delta scuti stars BD -7 1108, KU centauri and v567 ophiuchi.," Astronomy and Astrophysics, vol. 228, pp. 350–360, feb 1990.

[13] J. C. Hinks and J. L. Crassidis, "Angular velocity bounds via light curve glint duration," in AIAA Guidance, Navigation, and Control Conference, p. 0627, AIAA, 01 2016.

[14] J. Allworth, L. Windrim, J. Wardman, D. Kucharski, J. Bennett, and M. Bryson, "Development of a high fidelity simulator for generalised photometric based space object classification using machine learning," arXiv preprint arXiv:2004.12270, 2020.

[15] Y. Huo, Z. Li, Y. Fang, and F. Zhang, "Classification for geosynchronous satellites with deep learning and multiple kernel learning," Applied optics, vol. 58, no. 21, pp. 5830–5838, 2019.

[16] W. Song, L. Zhang, Y. Tian, S. Fong, J. Liu, and A. Gozho, "Cnn-based 3d object classification using hough space of lidar point clouds," Human-centric Computing and Information Sciences, vol. 10, no. 1, pp. 1–14, 2020.

[17] R. Linares and J. L. Crassidis, "Space object classification using model driven and data driven methods," in Spaceflight Mechanics 2016 Meeting, 2016.

[18] B. Jia, E. Blasch, K. Pham, D. Shen, Z. Wang, and G. Chen, "Space object classification using fused features of time series data," Advanced Maui Optical and Space Surveillance Technologies (AMOS), 2017.

[19] D. S. Lauretta, "Application of machine-learning algorithms for on-board asteroid shape model determination," NASA Facts, 2018.

[20] S. Segal, P. Gurfil, and K. Shahid, "In-orbit tracking of resident space objects: A comparison of monocular and stereoscopic vision," IEEE Transactions on Aerospace and Electronic Systems, vol. 50, no. 1, pp. 676–688, 2014.

[21] D. J. Kessler and B. G. Cour-Palais, "Collision frequency of artificial satellites: The creation of a debris belt," Journal of Geophysical Research: Space Physics, vol. 83, no. A6, pp. 2637–2646, 1978.

[22] D. J. Kessler, "Orbital debris environment for spacecraft in low earth orbit," AIAA Journal of Spacecraft and Rockets, vol. 28, no. 3, pp. 347–351, 1991.

[23] P. Huijse, P. A. Estevez, P. Protopapas, P. Zegers, and J. C. Principe, "An information theoretic algorithm for finding periodicities in stellar light curves," IEEE Transactions on Signal Processing, vol. 60, no. 10, pp. 5135–5145, 2012.

[24] W. Wild, "Estimating asteroid pole orientation from photometric light curves," International Amateur-Professional Photoelectric Photometry Communications, vol. 68, p. 14, 1997.

[25] F. Santoni, E. Cordelli, and F. Piergentili, "Determination of disposed-upper-stage attitude motion by ground-based optical observations," Journal of Spacecraft and Rockets, vol. 50, no. 3, pp. 701–708, 2013.

[26] K. Balachandran and K. Subbarao, "Estimating sidereal rotation period of resident space objects using non-uniformly sampled light curves," in The Advanced Maui Optical and Space Surveillance Technologies Conference, p. 32, sep 2018.

[27] N. R. Lomb, "Least-squares frequency analysis of unequally spaced data,"

Astrophysics and space science, vol. 39, no. 2, pp. 447–462, 1976.

[28] J. T. VanderPlas, "Understanding the lomb–scargle periodogram," The Astrophysical Journal Supplement Series, vol. 236, no. 1, p. 16, 2018.

[29] T. J. Deeming, "Fourier analysis with unequally-spaced data," Astrophysics and Space Science, vol. 36, pp. 137–158, aug 1975.

[30] A. Heck, J. Manfroid, and G. Mersch, "On period determination methods," Astrophysics and Space Science, vol. 59, pp. 63–72, jan 1985.

[31] A. Schwarzenberg-Czerny, "Optimum period search: Quantitative analysis," The Astrophysical Journal, vol. 516, pp. 315–323, may 1999.

[32] D. N. Swingler, "A comparison of the fourier, jurkevich, and stellingwerf methods of period estimation," Astronomical Journal, vol. 97, pp. 280–287, jan 1989.

[33] E. Distefano, A. C. Lanzafame, A. F. Lanza, S. Messina, A. J. Korn, K. Eriksson, and J. Cuypers, "Determination of rotation periods in solar-like stars with irregular sampling: the gaia case," Monthly Notices of the Royal Astronomical Society, vol. 421, pp. 2774–2785, 04 2012.

[34] P. Dubath, L. Rimoldini, M. Süveges, J. Blomme, M. López, L. M. Sarro, J. De Ridder, J. Cuypers, L. Guy, I. Lecoeur, and et al., "Random forest automated supervised classification of hipparcos periodic variable stars," Monthly Notices of the Royal Astronomical Society, vol. 414, p. 2602–2617, May 2011.

[35] M. J. Graham, A. J. Drake, S. G. Djorgovski, A. A. Mahabal, C. Donalek, V. Duan, and A. Maker, "A comparison of period finding algorithms," Monthly Notices of the Royal Astronomical Society, vol. 434, pp. 3423–3444, 08 2013.

[36] J. T. VanderPlas and Ž. Ivezic´, "PERIODOGRAMS FOR MULTIBAND ASTRONOMICAL TIME SERIES," The Astrophysical Journal, vol. 812, p. 18, oct 2015.

[37] P. Huijse, P. Estévez, P. Zegers, J. Príncipe, and P. Protopapas, "Period

estimation in astronomical time series using slotted correntropy," IEEE Signal Processing Letters, vol. 18, pp. 371–374, 2011.

[38] M. J. Graham, A. J. Drake, S. G. Djorgovski, A. A. Mahabal, and C. Donalek, "Using conditional entropy to identify periodicity," Monthly Notices of the Royal Astronomical Society, vol. 434, p. 2629–2635, Jul 2013.

[39] Y. Wang, R. Khardon, and P. Protopapas, "Nonparametric bayesian estimation of periodic light curves," The Astrophysical Journal, vol. 756, p. 67, sep 2012.

[40] K. Levenberg, "A method for the solution of certain non-linear problems in least squares," Quarterly of applied mathematics, vol. 2, no. 2, pp. 164–168, 1944.

[41] T. Yanagisawa and H. Kurosaki, "Shape and motion estimate of LEO debris using light curves," Advances in Space Research, vol. 50, no. 1, pp. 136–145, 2012.

[42] J. C. Armstrong, B. Nellermore, and L. Reitzler, "Measuring rotation periods of asteroids using differential CCD photometry," International Amateur-Professional Photoelectric Photometry Communications, vol. 63, p. 59, 1996.

[43] P. Laguna, G. B. Moody, and R. G. Mark, "Power spectral density of unevenly sampled data by least-square analysis: performance and application to heart rate signals," IEEE Transactions on Biomedical Engineering, vol. 45, no. 6, pp. 698–715, 1998.

[44] E. Sejdić, I. Djurović, and L. Stanković, "Fractional fourier transform as a signal processing tool: An overview of recent developments," Signal Processing, vol. 91, no. 6, pp. 1351–1369, 2011.

[45] H. M. Ozaktas, O. Arikan, M. A. Kutay, and G. Bozdagt, "Digital computation of the fractional fourier transform," IEEE Transactions on signal processing, vol. 44, no. 9, pp. 2141–2150, 1996.

[46] J. D. Scargle, "Studies in astronomical time series analysis. II-statistical aspects of spectral analysis of unevenly spaced data," The Astrophysical Journal, vol. 263, pp. 835–853, 1982.

[47] J. H. Horne and S. L. Baliunas, "A prescription for period analysis of unevenly sampled time series," The Astrophysical Journal, vol. 302, pp. 757–763, 1986.

[48] J. Burke, Edward W., W. W. Rolland, and W. R. Boy, "A photoelectric study of magnetic variable stars," Journal of the Royal Astronomical Society of Canada, vol. 64, no. 6, pp. 353–369, 1970.

[49] R. F. Stellingwerf, "Period determination using phase dispersion minimization," The Astrophysical Journal, vol. 224, pp. 953–960, 1978.

[50] M. M. Dworetsky, "A period-finding method for sparse randomly spaced observations or "how long is a piece of string?"," Monthly Notices of the Royal Astronomical Society, vol. 203, no. 4, pp. 917–924, 1983.

[51] J. D. Scargle, "Studies in astronomical time series analysis. III-fourier transforms, autocorrelation functions, and cross-correlation functions of unevenly spaced data," The Astrophysical Journal, vol. 343, pp. 874–887, 1989.

[52] B. Scholkopf, A. J. Smola, F. Bach, et al., Learning with kernels: support vector machines, regularization, optimization, and beyond. MIT press, 2002.

[53] A. Gunduz and J. C. Principe, "Correntropy as a novel measure for nonlinearity tests," Signal Processing, vol. 89, no. 1, pp. 14–23, 2009.

[54] D. Bédard and M. Lévesque, "Analysis of the canx-1 engineering model spectral reflectance measurements," Journal of Spacecraft and Rockets, vol. 51, no. 5, pp. 1492–1504, 2014.

[55] M. A. Earl and G. A. Wade, "Observations of the spin-period variations of inactive box-wing geosynchronous satellites," Journal of Spacecraft and Rockets, vol. 52, no. 3, pp. 968–977, 2015.

[56] J. C. van der Ha and V. J. Lappas, "Long-term attitude drift of spinning spacecraft under solar radiation torques," Journal of Guidance, Control, and Dynamics, vol. 30, no. 5, pp. 1470–1479, 2007.

[57] J. Pepper, K. G. Stassun, and B. S. Gaudi, "Kelt: The kilodegree extremely little telescope, a survey for exoplanets transiting bright, hot stars," Handbook of Exoplanets, p. 969–980, 2018.

[58] C. Obermeier, T. Henning, J. E. Schlieder, I. J. Crossfield, E. A. Petigura, A. W. Howard, E. Sinukoff, H. Isaacson, D. R. Ciardi, T. J. David, et al., "K2 discovers a busy bee: an unusual transiting neptune found in the beehive cluster," The Astronomical Journal, vol. 152, no. 6, p. 223, 2016.

[59] J. N. Pelton, "The space debris threat and the kessler syndrome," in Space Debris and Other Threats from Outer Space, pp. 17–23, Springer, 2013.

[60] D. J. Kessler, "Orbital debris environment for spacecraft in low earth orbit," Journal of spacecraft and rockets, vol. 28, no. 3, pp. 347–351, 1991.

[61] B. Bradley and P. Axelrad, "Lightcurve inversion for shape estimation of geo objects from space-based sensors," in Univ. of Colorado. International Space Symposium for Flight Dynamics, 2014.

[62] M. Kaasalainen, J. Torppa, and J. Piironen, "Models of twenty asteroids from photometric data," Icarus, vol. 159, no. 2, pp. 369 – 395, 2002.

[63] Kaasalainen, M., Lu, X., and Vänttinen, A.-V., "Optimal computation of brightness integrals parametrized on the unit sphere," Astronomy & Astrophysics, vol. 539, p. A96, 2012.

[64] H. Seo, H. Jin, Y. Song, Y. Lee, and Y. Oh, "The photometric brightness variation of geostationary orbit satellite," Journal of Astronomy and Space Sciences, vol. 30, no. 3, pp. 179–185, 2013.

[65] M. Hejduk, "Phase functions of deep-space orbital debris," in Proceedings of the

Advanced Maui Optical and Space Surveillance Technologies Conference, 2007.

[66] M. Hejduk, "Specular and diffuse components in spherical satellite photometric modeling," in Proceedings of the Advanced Maui Optical and Space Surveillance Technologies Conference, p. E15, 2011.

[67] M. Mulrooney, "Optical phase functions and albedos of orbiting debris objects," Master's thesis, Rice University, 1993.

[68] J. A. Reeger and B. Fornberg, "Numerical quadrature over the surface of a sphere," Studies in Applied Mathematics, vol. 137, no. 2, pp. 174–188, 2016.

[69] B. Fornberg and C. Piret, "A stable algorithm for flat radial basis functions on a sphere," SIAM Journal on Scientific Computing, vol. 30, no. 1, pp. 60–80, 2008.

[70] J. Li, X. Wang, and L. Qu, "Calculation of physical optics integrals over nurbs surface using a delaminating quadrature method," IEEE Transactions on Antennas and Propagation, vol. 60, no. 5, pp. 2388–2397, 2012.

[71] X.-P. Lu and D. Jewitt, "Dependence of light curves on phase angle and asteroid shape," The Astronomical Journal, vol. 158, no. 6, p. 220, 2019.

[72] Durech, J., Sidorin, V., and Kaasalainen, M., "Damit: a database of asteroid models," Astronomy & Astrophysics, vol. 513, p. A46, 2010.

[73] C. H. Beentjes, "Quadrature on a spherical surface," Working note available on the website http://people. maths. ox. ac. uk/beentjes/Essays, 2015.

[74] V. Lebedev, "Quadratures on a sphere," USSR Computational Mathematics and Mathematical Physics, vol. 16, no. 2, pp. 10 – 24, 1976.

[75] W. H. Press, S. A. Teukolsky, W. T. Vetterling, and B. P. Flannery, Numerical recipes 3rd edition: The art of scientific computing. Cambridge university press, 2007.

[76] K. Balachandran and K. Subbarao, "Computing surface brightness integrals of artificial space objects with axisymmetric bodies using photometric light curves,"

in International Astronautical Congress, oct 2019.

[77] N. C. Combe, "Geometric classification of real ternary octahedral quartics," Discrete & Computational Geometry, vol. 60, no. 2, pp. 255–282, 2018.

[78] F. Santoni, E. Cordelli, and F. Piergentili, "Determination of disposed-upper-stage attitude motion by ground-based optical observations," Journal of Spacecraft and Rockets, vol. 50, no. 3, pp. 701–708, 2013.

[79] N. Li and Z. Cheng, "Mixed brightness-integrals of convex bodies," Journal of the Korean Mathematical Society, vol. 47, 09 2010.

[80] B. Fornberg and J. M. Martel, "On spherical harmonics based numerical quadrature over the surface of a sphere," Advances in Computational Mathematics, vol. 40, no. 5-6, pp. 1169–1184, 2014.

[81] P. Dao, K. Haynes, S. Gregory, J. Hollon, T. Payne, and K. Kinateder, "Machine classification and sub-classification pipeline for geo light curves," Proceedings of the Advanced Maui Optical and Space Surveillance Technologies Conference, p. 53, 2019.

[82] D.-W. Kim and C. A. Bailer-Jones, "A package for the automated classification of periodic variable stars," Astronomy & Astrophysics, vol. 587, p. A18, 2016.

[83] B. Esmael, A. Arnaout, R. K. Fruhwirth, and G. Thonhauser, "Improving time series classification using hidden markov models," in 2012 12th International Conference on Hybrid Intelligent Systems (HIS), pp. 502–507, IEEE, 2012.

[84] L. Batal, L. Sacchi, R. Bellazzi, and M. Hauskrecht, "Multivariate time series classification with temporal abstractions," in Proceedings of the 22nd International Florida Artificial Intelligence Research Society Conference, FLAIRS-22, pp. 344–349, University of Pittsburgh, 2009.

[85] J. Lin, E. Keogh, S. Lonardi, and B. Chiu, "A symbolic representation of time series, with implications for streaming algorithms," in Proceedings of the 8th

ACM SIGMOD workshop on Research issues in data mining and knowledge discovery, pp. 2–11, 2003.

[86] B. Esmael, A. Arnaout, R. K. Fruhwirth, and G. Thonhauser, "Multivariate time series classification by combining trend-based and value-based approximations," in International Conference on Computational Science and Its Applications, pp. 392–403, Springer, 2012.

[87] E. Keogh, K. Chakrabarti, M. Pazzani, and S. Mehrotra, "Locally adaptive dimensionality reduction for indexing large time series databases," in Proceedings of the 2001 ACM SIGMOD international conference on Management of data, pp. 151–162, 2001.

[88] R. Polikar, "Ensemble based systems in decision making," IEEE Circuits and systems magazine, vol. 6, no. 3, pp. 21–45, 2006.

[89] L. Xu, A. Krzyzak, and C. Y. Suen, "Methods of combining multiple classifiers and their applications to handwriting recognition," IEEE transactions on systems, man, and cybernetics, vol. 22, no. 3, pp. 418–435, 1992.

[90] T. A. Hinners, K. Tat, and R. Thorp, "Machine learning techniques for stellar light curve classification," The Astronomical Journal, vol. 156, no. 1, p. 7, 2018.

[91] I. Nun, P. Protopapas, B. Sim, M. Zhu, R. Dave, N. Castro, and K. Pichara, "Fats: Feature analysis for time series," arXiv preprint arXiv:1506.00010, 2015.

[92] F. Bre, J. M. Gimenez, and V. D. Fachinotti, "Prediction of wind pressure coefficients on building surfaces using artificial neural networks," Energy and Buildings, vol. 158, pp. 1429–1441, 2018.

[93] I. Goodfellow, Y. Bengio, and A. Courville, Deep Learning. The MIT Press, 2016.

[94] D. P. Kingma and J. Ba, "Adam: A method for stochastic optimization," CoRR, vol. abs/1412.6980, 2015.

[95] Z. Sun, L. Di, and H. Fang, "Using long short-term memory recurrent neural network in land cover classification on landsat and cropland data layer time series," International journal of remote sensing, vol. 40, no. 2, pp. 593–614, 2019.

[96] F. A. Gers and J. Schmidhuber, "Recurrent nets that time and count," in Proceedings of the IEEE-INNS-ENNS International Joint Conference on Neural Networks. IJCNN 2000. Neural Computing: New Challenges and Perspectives for the New Millennium, vol. 3, pp. 189–194, IEEE, 2000.

[97] R. Jozefowicz, W. Zaremba, and I. Sutskever, "An empirical exploration of recurrent network architectures," in International conference on machine learning, pp. 2342–2350, 2015.

[98] A. Graves, A.-r. Mohamed, and G. Hinton, "Speech recognition with deep recurrent neural networks," in 2013 IEEE international conference on acoustics, speech and signal processing, pp. 6645–6649, IEEE, 2013.

[99] G. E. Dahl, T. N. Sainath, and G. E. Hinton, "Improving deep neural networks for lvcsr using rectified linear units and dropout," in 2013 IEEE international conference on acoustics, speech and signal processing, pp. 8609–8613, IEEE, 2013.

[100] S. Hochreiter and J. Schmidhuber, "Long short-term memory," Neural computation, vol. 9, no. 8, pp. 1735–1780, 1997.

[101] L. R. Rabiner, "A tutorial on hidden markov models and selected applications in speech recognition," Proceedings of the IEEE, vol. 77, no. 2, pp. 257–286, 1989.

[102] P. Wang, H. Wang, and W. Wang, "Finding semantics in time series," in Proceedings of the 2011 ACM SIGMOD International Conference on Management of data, pp. 385–396, 2011.

[103] J. Hagenauer and P. Hoeher, "A viterbi algorithm with soft-decision outputs

and its applications," in 1989 IEEE Global Telecommunications Conference and Exhibition,'Communications Technology for the 1990s and Beyond', pp. 1680–1686, IEEE, 1989.

[104] C. Früh, M. Jah, E. Valdez, P. Kervin, and T. Kelecy, "Taxonomy and classification scheme for artificial space objects," tech. rep., Air Force Research Lab, Kirtland AFB NM, Space Vehicles Directorate, 2013.

[105] A. W.-C. Liew, N.-F. Law, X.-Q. Cao, and H. Yan, "Statistical power of fisher test for the detection of short periodic gene expression profiles," Pattern Recognition, vol. 42, no. 4, pp. 549–556, 2009.

[106] I. Nun, P. Protopapas, B. Sim, and W. Chen, "Ensemble learning method for outlier detection and its application to astronomical light curves," The Astronomical Journal, vol. 152, no. 3, p. 71, 2016.

[107] K. Vixie, "Detection of aliasing in signals," in Portland State University and Los Alamos National Laboratory, 2007.

[108] K. R. Vixie, M. Wolinsky, and D. E. Sigeti, "The bispectral aliasing test: a clarification and some key examples," in ISSPA'99. Proceedings of the Fifth International Symposium on Signal Processing and its Applications (IEEE Cat. No. 99EX359), vol. 1, pp. 255–258, IEEE, 1999.

[109] J. Bennet, C. Arul Ganaprakasam, and K. Arputharaj, "A discrete wavelet based feature extraction and hybrid classification technique for microarray data analysis," The Scientific world journal, vol. 2014, 2014.

[110] I. M. Tibuleac and E. Herrin, "An automatic method for determination of lg arrival times using wavelet transforms," Seismological Research Letters, vol. 70, no. 5, pp. 577–595, 1999.

[111] S. Deokar and L. Waghmare, "Integrated dwt–fft approach for detection and classification of power quality disturbances," International Journal of Electrical

Power & Energy Systems, vol. 61, pp. 594–605, 2014.

[112] T. N. Ukwatta and P. R. Wozniak, "Integrating temporal and spectral features of astronomical data using wavelet analysis for source classification," in 2015 IEEE Applied Imagery Pattern Recognition Workshop (AIPR), pp. 1–10, IEEE, 2015.

[113] P. Kumar and E. Foufoula-Georgiou, "Wavelet analysis for geophysical applications," Reviews of geophysics, vol. 35, no. 4, pp. 385–412, 1997.

[114] M. Ebrahimkhani and M. Arbab, "Extraction of thz absorption signatures obscured by rough surface scattering using discrete wavelet transform," in 2018 43rd International Conference on Infrared, Millimeter, and Terahertz Waves (IRMMW-THz), pp. 1–2, IEEE, 2018.

[115] M. E. Khani, D. P. Winebrenner, and M. H. Arbab, "Phase function effects on identification of terahertz spectral signatures using the discrete wavelet transform," IEEE Transactions on Terahertz Science and Technology, vol. 10, no. 6, pp. 656–666, 2020.

[116] S. Guo, S. Lin, and Z. Huang, "Feature extraction of p300s in eeg signal with discrete wavelet transform and fisher criterion," in 2015 8th International Conference on Biomedical Engineering and Informatics (BMEI), pp. 200–204, IEEE, 2015.

[117] D. Föhring, R. Wilson, J. Osborn, and V. Dhillon, "Atmospheric scintillation noise in ground-based exoplanet photometry," Monthly Notices of the Royal Astronomical Society, vol. 489, no. 4, pp. 5098–5108, 2019.

[118] J. Irwin, M. Irwin, S. Aigrain, S. Hodgkin, L. Hebb, and E. Moraux, "The monitor project: data processing and light curve production," Monthly Notices of the Royal Astronomical Society, vol. 375, no. 4, pp. 1449–1462, 2007.

[119] P. Ryan and D. Sandler, "Scintillation reduction method for photometric mea-

surements," Publications of the Astronomical Society of the Pacific, vol. 110, no. 752, p. 1235, 1998.

[120] C. Früh, T. M. Kelecy, and M. K. Jah, "Coupled orbit-attitude dynamics of high area-to-mass ratio (hamr) objects: influence of solar radiation pressure, earth's shadow and the visibility in light curves," Celestial Mechanics and Dynamical Astronomy, vol. 117, no. 4, pp. 385–404, 2013.

[121] C. Früh and T. Schildknecht, "Attitude motion of space debris objects under influence of solar radiation pressure and gravitiy," in 63rd international Astronautical congress, 2012.

[122] J. Šilha, J.-N. Pittet, M. Hamara, and T. Schildknecht, "Apparent rotation properties of space debris extracted from photometric measurements," Advances in space research, vol. 61, no. 3, pp. 844–861, 2018.

[123] R. Kanzler, J. Silha, T. Schildknecht, B. Fritsche, T. Lips, and H. Krag, "Space debris attitude simulation-ιota (in-orbit tumbling analysis)," in Proceedings of the Advanced Maui Optical and Space Surveillance Technologies Conference, held in Wailea, Maui, Hawaii, 2014.

[124] R. B. Fisher, Using surfaces and object models to recognize partially obscured objects. Department of Artificial Intelligence, University of Edinburgh, 1983.

[125] M. Schlecker, "Irregular variability in kepler photometry," Master's thesis, Technical University of Munich, 12 2016.

[126] C. Z. Mooney, Monte carlo simulation. No. 116, Sage, 1997.

[127] W. Wright, "Bayesian approach to neural-network modeling with input uncertainty," IEEE Transactions on Neural Networks, vol. 10, no. 6, pp. 1261–1270, 1999.

[128] S. Goel and R. Bajpai, "Impact of uncertainty in the input variables and model parameters on predictions of a long short term memory (lstm) based sales

forecasting model," Machine Learning and Knowledge Extraction, vol. 2, no. 3, pp. 256–270, 2020.

[129] K.-C. Jim, C. L. Giles, and B. G. Horne, "An analysis of noise in recurrent neural networks: convergence and generalization," IEEE Transactions on neural networks, vol. 7, no. 6, pp. 1424–1438, 1996.

[130] J. W. Richards, D. L. Starr, H. Brink, A. A. Miller, J. S. Bloom, N. R. Butler, J. B. James, J. P. Long, and J. Rice, "Active learning to overcome sample selection bias: Application to photometric variable star classification," The Astrophysical Journal, vol. 744, no. 2, p. 192, 2011.

[131] C. Agnor, A. Barr, B. Bierhaus, D. Brain, B. Bills, W. Bottke, B. Buratti, S. Charnoz, J. Cho, A. Christou, et al., "The exploration of neptune and triton," 2009.

[132] J. Elliot, M. Person, S. McDonald, M. Buie, E. Dunham, R. Millis, R. Nye, C. Olkin, L. Wasserman, L. Young, et al., "The prediction and observation of the 1997 july 18 stellar occultation by triton: More evidence for distortion and increasing pressure in triton's atmosphere," Icarus, vol. 148, no. 2, pp. 347–369, 2000.

[133] J. Elliot, J. Stansberry, C. Olkin, M. Agner, and M. Davies, "Triton's distorted atmosphere," Science, vol. 278, no. 5337, pp. 436–439, 1997.

[134] T. R. C. Perez, A framework for employing femtosatellites in planetary science missions, including a proposed mission concept for Titan. PhD thesis, University of Texas at Arlington, 2017.

[135] W. B. McKinnon and R. L. Kirk, "Chapter 40 - triton," in Encyclopedia of the Solar System (Third Edition) (T. Spohn, D. Breuer, and T. V. Johnson, eds.), pp. 861 – 881, Boston: Elsevier, third edition ed., 2014.

[136] V. Inglezakis, "Chapter 7 - extraterrestrial environment," in Environment and

Development (S. G. Poulopoulos and V. J. Inglezakis, eds.), pp. 453 – 498, Amsterdam: Elsevier, 2016.

[137] A. L. Broadfoot, S. K. Atreya, J. L. Bertaux, J. E. Blamont, A. J. Dessler, T. M. Donahue, W. T. Forrester, D. T. Hall, F. Herbert, J. B. Holberg, D. M. Hunter, V. A. Krasnopolsky, S. Linick, J. I. Lunine, J. C. McConnell, H. W. Moos, B. R. Sandel, N. M. Schneider, D. E. Shemansky, G. R. Smith, D. F. Strobel, and R. V. Yelle, "Ultraviolet spectrometer observations of neptune and triton," Science, vol. 246, no. 4936, pp. 1459–1466, 1989.

[138] W. K. Hartmann and R. Miller, The grand tour: a traveler's guide to the Solar System. Workman Publishing, 3 ed., May 2005.

[139] E. Lellouch, C. De Bergh, B. Sicardy, S. Ferron, and H.-U. Käufl, "Detection of co in triton's atmosphere and the nature of surface-atmosphere interactions," Astronomy & Astrophysics, vol. 512, p. L8, 2010.

[140] B. A. Smith, L. A. Soderblom, D. Banfield, c. Barnet, A. T. Basilevsky, R. F. Beebe, K. Bollinger, J. M. Boyce, A. Brahic, G. A. Briggs, R. H. Brown, c. Chyba, s. A. Collins, T. Colvin, A. F. Cook, D. Crisp, S. K. Croft, D. Cruikshank, J. N. Cuzzi, G. E. Danielson, M. E. Davies, E. De Jong, L. Dones, D. Godfrey, J. Goguen, I. Grenier, V. R. Haemmerle, H. Hammel, c. J. Hansen, c. P. Helfenstein, C. Howell, G. E. Hunt, A. P. Ingersoll, T. V. Johnson, J. Kargel, R. Kirk, D. I. Kuehn, S. Limaye, H. Masursky, A. McEwen, D. Morrison, T. Owen, W. Owen, J. B. Pollack, c. c. Porco, K. Rages, P. Rogers, D. Rudy, C. Sagan, J. Schwartz, E. M. Shoemaker, M. Showalter, B. Sicardy, D. Simonelli, J. Spencer, L. A. Sromovsky, C. Stoker, R. G. Strom, V. E. Suomi, S. P. Synott, R. J. Terrile, P. Thomas, W. R. Thompson, A. Verbiscer, and J. Veverka, "Voyager 2 at neptune: Imaging science results," Science, vol. 246, no. 4936, pp. 1422–1449, 1989.

[141] E. Lellouch, M. Blanc, J. Oukbir, and P.-Y. Longaretti, "A model of triton's atmosphere and ionosphere," Advances in Space Research, vol. 12, no. 11, pp. 113 – 121, 1992.

[142] H. L. Weisberg, The Study of Planetary Atmospheres by Stellar Occultation. Santa Monica, CA: RAND Corporation, 1962.

[143] J. Elliot and C. Olkin, "Probing planetary atmospheres with stellar occultations," Annual Review of Earth and Planetary Sciences, vol. 24, no. 1, pp. 89–123, 1996.

[144] C. Olkin, J. Elliot, H. Hammel, A. Cooray, S. McDonald, J. Foust, A. Bosh, M. Buie, R. Millis, L. Wasserman, et al., "The thermal structure of triton's atmosphere: Results from the 1993 and 1995 occultations," Icarus, vol. 129, no. 1, pp. 178–201, 1997.

[145] D. Alp and B.-O. Demory, "Refraction in exoplanet atmospheres-photometric signatures, implications for transmission spectroscopy, and search in kepler data," Astronomy & Astrophysics, vol. 609, p. A90, 2018.

[146] E. Young, "A fourier optics method for calculating stellar occultation light curves by objects with thin atmospheres," The Astronomical Journal, vol. 144, no. 2, p. 32, 2012.

[147] R. Millis, L. Wasserman, O. Franz, R. Nye, J. Elliot, E. Dunham, A. Bosh, L. Young, S. Slivan, A. Gilmore, P. Kilmartin, W. Allen, R. Watson, S. Dieters, K. Hill, A. Giles, G. Blow, J. Priestley, W. Kissling, W. Walker, B. Marino, D. Dix, A. Page, J. Ross, H. Avey, D. Hickey, H. Kennedy, K. Mottram, G. Moyland, T. Murphy, C. Dahn, and A. Klemola, "Pluto's radius and atmosphere: Results from the entire 9 june 1988 occultation data set," Icarus, vol. 105, no. 2, pp. 282 – 297, 1993.

[148] C. B. Olkin, J. L. Elliot, S. J. Bus, S. W. McDonald, and C. C. Dahn, "Astrometry of single-chord occultations: Application to the 1993 triton event," Publications

of the Astronomical Society of the Pacific, vol. 108, p. 202, feb 1996.

[149] A. Dias-Oliveira, B. Sicardy, E. Lellouch, R. Vieira-Martins, M. Assafin, J. I. B. Camargo, F. Braga-Ribas, A. Gomes-Júnior, G. Benedetti-Rossi, F. Colas, et al., "Pluto's atmosphere from stellar occultations in 2012 and 2013," The Astrophysical Journal, vol. 811, no. 1, p. 53, 2015.

[150] R. French, J. Elliot, and P. Gierasch, "Analysis of stellar occultation data: Effects of photon noise and initial conditions," Icarus, vol. 33, no. 1, pp. 186–202, 1978.

[151] J. D. Rummel and D. B. Pugel, "Planetary protection technologies for planetary science instruments, spacecraft, and missions: Report of the nasa planetary protection technology definition team (pptdt)," Life Sciences in Space Research, vol. 23, pp. 60–68, 2019.

[152] P. Enterprises, K. Braggs, C. Janda, C. Brannon, D. Lee, P. Cowart, L. Mousessian, G. Gordon, and D. Edberg, "Project tes: Triton exploration system," California State Polytechnic University, Pomona.

[153] J. Hinks and M. Psiaki, "Simultaneous orbit and atmospheric density estimation for a satellite constellation," in AIAA/AAS Astrodynamics Specialist Conference, p. 8258, 2010.

[154] T. C. Sorensen, E. J. Pilger, M. S. Wood, M. A. Nunes, and L. K. Yoneshige, "Mission design and operations of a constellation of small satellites for remote sensing," in Sensors and Systems for Space Applications VI, vol. 8739, p. 873906, International Society for Optics and Photonics, 2013.

VITA

Katiyayni Balachandran received her B.Eng in Space Engineering from York University in 2017 and her Ph.D. in Aerospace Engineering from the University of Texas at Arlington in 2021. She was awarded the Amelia Earhart Fellowship and the Natural Sciences and Engineering Research Council of Canada (NSERC) Alexander Graham Bell Graduate Scholarship. She conducted research at the Centre for Research in Earth & Space Science (CRESS) in optical space instrumentation and worked on the Canada Mars Sample Return Analog Deployment as a rover planner during her undergraduate program. In 2019, she worked on space surveillance & tracking of debris at the European Space Agency (ESA-ESOC) to perform attitude estimation and observe tumbling motion of perturbed objects. During her doctoral studies, she was a graduate teaching assistant for several courses in the Mechanical and Aerospace Engineering (MAE) department. Katiyayni primarily works in areas of space object characterization, orbital mechanics and astrodynamics, signal processing, neural network design, and optical instrumentation. She has also worked on guidance and control of aerospace vehicles as well as analysis of nonlinear dynamical systems. Her training in space communications has allowed her to delve into planetary surface exploration using rovers and a network of small landers.